Elaboration of chiral material by electrochemistry

Laura Adam

université de BORDEAUX

THÈSE PRÉSENTÉE

POUR OBTENIR LE GRADE DE

DOCTEUR DE

L'UNIVERSITÉ DE BORDEAUX

ÉCOLE DOCTORALE DES SCIENCES CHIMIQUES

SPÉCIALITÉ CHIMIE - PHYSIQUE

Par Laura, Marie ADAM

Elaboration de matériaux chiraux par électrochimie

Sous la direction d'Alexander KUHN

Soutenue le 16 décembre 2021

Membres du jury :

M. Nicolas MANO	Directeur de recherche, Université de Bordeaux	Président
M. Nicolas STEIN	Maître de conférences, Université de Lorraine	Rapporteur
Mme Chularat WATTANAKIT	Assistant professor, Vidyasirimedhi institute of science and technology	Rapporteur
M. Alexander KUHN	Professeur, Bordeaux INP	Directeur de thèse

« Si tu veux construire un bateau, ne rassemble pas tes hommes et femmes pour leur donner des ordres, pour expliquer chaque détail, pour leur dire où trouver chaque chose … Si tu veux construire un bateau, fais naître dans le cœur de tes hommes et femmes le désir de la mer. »

- *Antoine de Saint-Exupéry*

Cette thèse, mon étoile.

Remerciements

Nous y voilà enfin, quatre années se sont écoulées entre mon arrivée à Bordeaux et la fin de cette thèse. Quatre années qui ont été riches d'enseignements, de rencontres, d'aventures et d'expériences. Quatre années qui ont réservées leurs lots de difficultés et de réjouissances. Quatre années qui m'ont terriblement appris sur moi-même mais aussi sur les autres et qui ont remis en question tout un projet professionnel. Quatre années intenses.

Ce travail a été réalisé sous la direction d'Alexander Kuhn, qui a posé le cadre de ce travail, évitant ainsi une trop grande exploration du sujet qui aurait pu être difficile à exploiter.

Cette thèse n'aurait pas abouti sans le soutien précieux d'un certain nombre de personne.

Tout d'abord, Stéphane Reculusa, de mon arrivée au sein du laboratoire à la soutenance, tu auras été présent et un repère qui, à plusieurs reprises, m'a permis de ne pas me noyer (pas totalement en tout cas). C'est toujours un plaisir de pouvoir discuter science avec toi, que ce soit sur ce sujet de thèse ou bien sur d'autres projets. Même au cours de cette dernière année que j'ai passée à distance du laboratoire, tu continuais de m'accorder du temps, et je t'en suis infiniment reconnaissante,

Merci Stéphane Arbault, toi aussi, en plus des discussions scientifiques, tu as été un soutien fort appréciable. Merci infiniment pour ta bienveillance et ta sagesse,

Je tiens à remercier également Laurent Bouffier pour m'avoir consacré du temps en cette fin de thèse. Les circonstances font que nous n'avons eu que peu d'échanges *in fine*, et je le regrette, mais je retiendrai tes connaissances impressionnantes, ton enthousiasme ainsi que ta rigueur,

Merci à Alice Dauphin d'avoir été très présente tout au long de cette aventure. Parce que je n'oublierais pas tes « Aller ! Demain rdv 7h, j'apporte le petit déj' et ça va marcher ! » et toutes les petites victoires célébrées à coup d'Apibul,

Cristina Carucci and Eliana Farias, it was such a pleasure to share the office for few months with both of you, maybe the best atmosphere I could feel during this tough PhD process. You are among the most beautiful persons I had the joy to meet during these four years. And, as I always mix up the words, "grazias"!

Je remercie aussi Pauline Lefrançois, ta présence pendant cette dernière année aurait été d'un grand secours. Merci pour ton écoute et ta compréhension,

Merci à Emmanuel Suraniti, pour nos discussions scientifiques et celles qui l'étaient moins, pour avoir essayé à plusieurs reprises de me redonner confiance à des moments où je ne croyais plus en grand-chose. Merci pour tes mots réconfortants et ta clairvoyance,

Thomas Delahaye : ton soutien à distance tout au long de cette thèse a été très appréciable, merci pour ça … Mais je n'oublie pas que tu as commencé par infecté le labo d'une odeur de vinaigre !

Cécile Allilaire, ça a été une joie de partager ces quelques moments avec toi. Merci pour nos discussions … Et tes orangettes (ça manque !),

Bertrand Goudeau, pour ton expertise en microscopie optique et ton envie de comprendre et de toujours apprendre plus. Voilà une précieuse personne pour un laboratoire ! … et merci aussi pour ton imagination débordante pour l'élaboration de plans machiavéliques dont notre cher Camille a souvent fait les frais !

Camille Colin (justement !), les circonstances ont fait qu'on s'est un peu perdus de vue en étant au même endroit physiquement, mais je garderai en mémoire les quelques premiers mois passés à faire preuve d'inventivité pour se taquiner mutuellement (et dire que tout est parti d'un schtroumph …),

Je remercie également les autres personnes que j'ai pu rencontrer au sein du laboratoire et qui ont comptées au cours de cette aventure. Je pense évidemment à Ariana Villarroel, Quentin Deville, Tatjana Safarik, Aleksandar Karajic, Ivana Trivunovic, Sharvina Shanmugathasan, Younness Boukarkour, Hélène Labie, Silvia Voci, Gerardo Salinas, Paul Chassagne, Iuliia Malytska, et Tommaso Nicolini.

Bien sûr, la thèse est prenante, mais la vie de doctorant ne se résume pas qu'au laboratoire. A l'*extérieur*, j'ai eu la chance de croiser la route de personnes formidables :

Je pense notamment aux orienteurs, les pommes de pin, mais gare à celui qui cumulerait des dettes !

Aux plongeurs, les nautiliens, même si le Covid a mis de la distance entre nous (de toutes façons, on voit rien à Cazaux !),

Une pensée pour Uriel également, rencontré au sommet de *Teotihuacan* (pour au final te retrouver à Bergerac, c'est nettement moins exotique !) qui m'a permis de faire mon premier concert au violoncelle et de reprendre une activité musicale stimulante entre instrument et voix !

Je remercie aussi les aprilisiens et aprilisiennes qui ont égayé quelques-uns de mes week-ends et en égayeront encore bien d'autres !

Je ne peux pas finir cette partie sans un petit retour en arrière. En 2016, alors en première année de master à l'université de Lorraine, j'avais en tête de m'arrêter à ce diplôme. Et le destin (ou appelez cela comme vous voulez) a voulu que je fasse mon stage dans un laboratoire de recherche : l'équipe 208 de l'Institut Jean Lamour. Quinze jours seulement passés auprès de mon maître de stage et j'avais déjà changé d'avis … Puis, entre ce stage et maintenant, il s'en est passées des choses et il a toujours été présent, m'a apportée une écoute attentive et a été d'une bienveillance à toute épreuve. Et encore aujourd'hui, il est présent en étant rapporteur de cette thèse. Merci pour tout, Nicolas.

J'en profite pour adresser un clin d'œil à mes anciens collègues qui tiennent toujours une place particulière dans mes pensées : Cristina C. A., Sophie L., Nathalie L, Clotilde B., Eric M., Sébastien D., Stéphanie M., Didier M., Philippe P., Abdel D., Laura M., Mariem M., Cédric F., Marie L. D., Keith T.

Un remerciement un peu particulier, à Adèle B. Combes pour son livre paru récemment qui fait la lumière sur certains dysfonctionnements du système académique (*Comment l'université broie les jeunes chercheurs, Précarité, harcèlement, loi du silence*, aux éditions Autrement). En espérant profondément qu'il s'agisse là d'un ouvrage initiateur d'une évolution bénéfique aux jeunes chercheurs, et au monde de la recherche de façon plus globale.

Enfin, cette thèse, au travers de multiples difficultés, m'a profondément affectée et poussée dans mes derniers retranchements. Merci aux personnes qui m'ont aidée et accompagnée dans cette quête d'énergie (notamment à celle qui m'aura fait découvrir Annie Ernaux, Jérémie Villet et redécouvrir Marcel Proust). A l'heure actuelle, je n'ai aucune certitude sur l'avenir, mais je sais que j'ai appris et grandi avec chacun d'entre vous. Merci à vous.

"Hope should be the last one to die"

- *24.10.2018, E.V.*

Résumé

Elaboration de matériaux chiraux par électrochimie

Cette thèse s'intéresse à la synthèse ainsi qu'à la modification de matériaux chiraux à différentes échelles par voie électrochimique.

La première partie est consacrée à la chiralité moléculaire et plus spécifiquement à l'électrodéposition de matrices métalliques poreuses via l'utilisation de cristaux liquides pour une réactivité enantiosélective. Le palladium a été choisi pour ses propriétés catalytiques concernant les réactions d'hydrogénation. Dans un premier temps, l'électrodéposition a été réalisée à l'échelle macroscopique et une étude de la morphologie des dépôts a été réalisée par microscopie électronique à balayage. Cette première étude a révélé une grande rugosité de surface et l'absence de nanostructuration du dépôt de palladium malgré la variation de nombreux paramètres. L'hypothèse principale est un transport des ions palladium limité par la diffusion en raison de la viscosité de l'électrolyte. La synthèse de palladium mésoporeux a donc été effectuée sur des substrats micrométriques, les ultramicroélectrodes. Une nette diminution de la rugosité de surface est observée et une grande surface électroactive est mesurée par voltampérométrie cyclique. La dihydroxy-3,4-phenylalanine a ensuite été utilisée pour induire une impression chirale lors de l'électrodéposition du palladium. La chiralité des matériaux ainsi obtenus a été testée par voltampérométrie impulsionnelle. Les résultats obtenus jusqu'à présent ne permettent pas d'affirmer que ces matériaux sont effectivement énantiosélectifs.

La seconde partie de cette thèse est consacrée à la modification de matériaux par électrochimie sans fil. Différents substrats de verre ou de silice ont été utilisés pour mettre au point un procédé de déposition autocatalytique suivi d'une modification par électrochimie bipolaire, permettant de briser la symétrie des objets obtenus. Si ces modifications sont obtenues à l'échelle macroscopiques, le procédé demande encore des modifications et des adaptations pour les objets micrométriques et, à plus longue échéance, nanométriques telles que des nanohélices de silice.

Mots clés : Electrochimie – Electrodéposition – Electrochimie bipolaire – Déposition electroless – Chiralité

Abstract

Elaboration of chiral material by electrochemistry

This thesis deals with the synthesis and the modification of chiral materials at different scales by electrochemistry.

The first part is devoted to molecular chirality, especially in the frame of the electrodeposition of porous metallic matrices by using lyotropic liquid crystal structures as a template to achieve enantioselective reactivity. Palladium has been chosen for its catalytic properties regarding hydrogenation reactions. First, electrodeposition at the macroscale and morphological study of the deposits by scanning electron microscope were performed. This study reveals a high roughness and the absence of nanostructuration of the palladium deposits despite a change of numerous parameters. The main hypothesis is a transport of palladium ions limited by diffusion in the viscous electrolyte. Afterwards, the synthesis of mesoporous palladium has been performed at ultramicroelectrodes. The surface appears much smoother than previously and a high electroactive surface area is measured by cyclic voltammetry. Dihydroxy-3,4-phenylalanine has been used for chiral imprinting during the electrodeposition process. The chirality of the obtained materials has been tested by differential pulse voltammetry. The results obtained so far do not allow concluding that these materials are actually enantioselective.

The second part of the thesis is devoted to the modification of materials by wireless electrochemistry. Different glass or silica substrates have been used to elaborate an electroless deposition process followed by bipolar electrochemical modification allowing breaking the symmetry of such objects. At the macroscale, modifications could be obtained, however at smaller scales, the process still requires some development in order to allow a modification of micro- and nanometric objects such as silica nanohelices.

Keywords: Electrochemistry – Electrodeposition – Bipolar electrochemistry – Electroless deposition – Chirality

Unité de recherche

Institut des Sciences Moléculaires (ISM), UMR CNRS 5255, Université de Bordeaux

Groupe NanoSystèmes Analytiques (NSysA)

16 Avenue Pey Berland

33607 Pessac France

Résumé

La chiralité est la propriété d'un objet selon laquelle il n'est pas superposable à son image au travers d'un miroir. Cette propriété est largement connue à l'échelle moléculaire. En effet, de nombreuses molécules chirales sont présentes autour de nous notamment dans les médicaments [1], les produits pour l'agriculture [2], les parfums [3], etc. Les deux images miroirs d'une même molécule sont appelées des énantiomères. Ils ont donc la même composition chimique mais diffèrent l'un de l'autre par leur arrangement spatial. Cette différence leur confère une spécificité d'action. Par exemple, concernant les parfums, deux énantiomères auront deux odeurs différentes. Dans le cas des médicaments, un énantiomère sera utile pour soigner une maladie alors que l'autre pourra être efficace pour une autre maladie, être inactif ou encore, être toxique.

Partant de ce constat, il est évident que la chiralité moléculaire représente un enjeu sociétal majeur. C'est ainsi que depuis les années 70, les chercheurs travaillent à l'élaboration d'outils et de procédés pour la synthèse asymétrique [4] qui permettent de favoriser la production d'un des deux énantiomères d'une même molécule, mais développent aussi des techniques pour la séparation chirale [5] et l'analyse énantiomérique [6,7].

Parmi les différents procédés développés, certains font appel à des surfaces chirales. Ainsi, le premier chapitre de cette thèse présente les différentes possibilités pour l'obtention de telles surfaces. Des molécules chirales peuvent être adsorbées à la surface de substrats achiraux comme cela a été réalisé par exemple avec l'adsorption des énantiomères de l'acide tartrique sur le substrat Cu(110) [8]. Il est également possible d'exposer des plans cristallins qui ont des hauts indices de Miller [9]. Une autre possibilité est d'avoir recours à l'impression moléculaire. Ce dernier point est notamment connu dans le monde des polymères (**MIP** : molecular imprinted polymer) [10]. Des impressions moléculaires ont également été réalisées avec des métaux [11]. Toutefois la faible surface active ne permet pas une grande sélectivité.

Le développement des métaux poreux par électrodéposition en utilisant des cristaux liquides comme matrice permet d'augmenter de manière significative la surface active [12].En effet, l'utilisation de surfactants formant une phase lyotrope permet d'effectuer une structuration par matrice dite « molle ». Cette phase lyotrope forme différents arrangements selon la composition du mélange ainsi que de la température qui sont résumés dans un diagramme de phase (Figure 1).

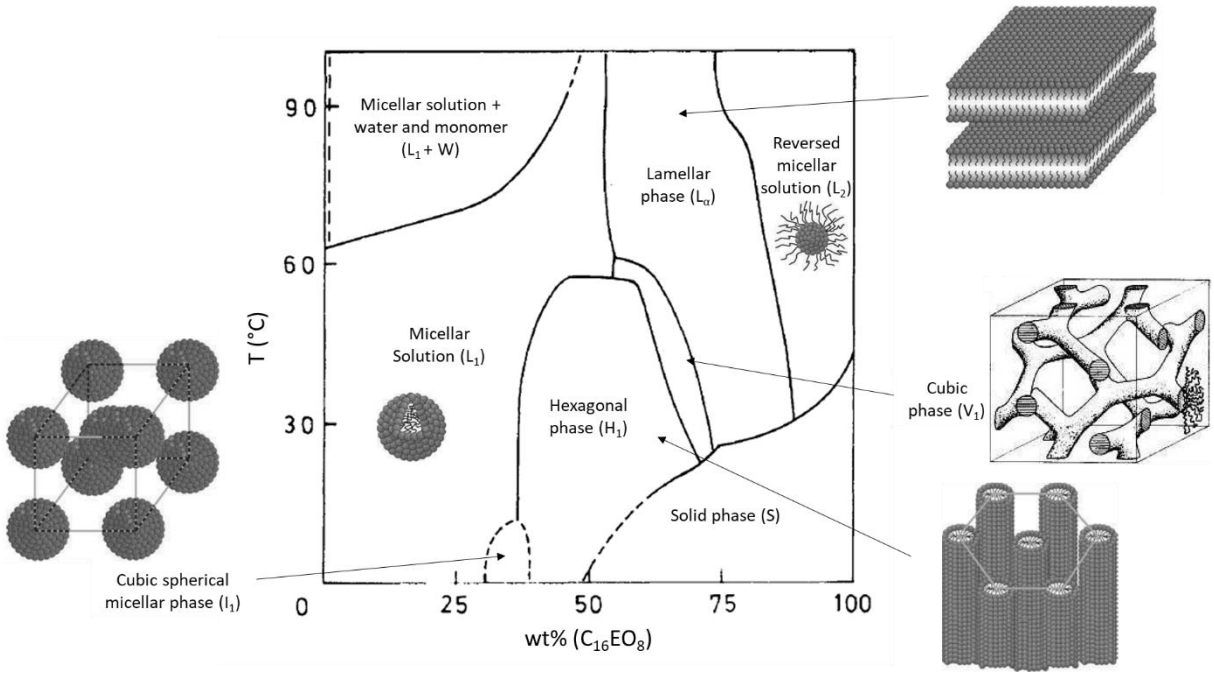

Figure 1: Diagramme de phase obtenu pour le mélange $C_{16}EO_8$/eau montrant les différents arrangements possibles en fonction des proportions surfactant/eau et de la température. Adaptée des références [13,14]

L'utilisation concomitante de cristaux liquides et de molécules chirales pour la synthèse de matériaux énantiosélectifs a été reportée dans la littérature pour trois matériaux différents, à savoir, le platine [15], un alliage de platine-iridium [16] et le nickel [17]. Les résultats obtenus, à la fois pour la reconnaissance chirale et la synthèse énantiosélective, sont particulièrement remarquables en terme de sélectivité.

La reconnaissance chirale est effectuée par voltampérométrie impulsionnelle (**DPV** : *Differential Pulse Voltammetry*). Des électrodes imprimées avec les énantiomères de la dihydroxy-3,4-phenylalanine (**DOPA**) ont été utilisées. Ainsi, les électrodes imprimées avec la L-DOPA présentent un signal d'oxydation plus important lorsqu'une solution de L-DOPA est utilisée, alors que le signal est plus faible avec une solution de D-DOPA ; l'inverse est observé avec des électrodes imprimées avec la D-DOPA (Figure 2 A).

La réduction sélective de l'acétophénone en phényléthanol (**PE**) a été réalisée soit à potentiel continu, soit à potentiel pulsé. Les excès énantiomériques (**% ee**) obtenus avec l'alliage platine-iridium sont plus importants que ceux obtenus avec le platine. L'alliage permet également la réutilisation des électrodes avec seulement une faible diminution de l'excès énantiomérique (Figure 2 B). Le cas du nickel montre que l'électrochimie pulsée permet une réelle augmentation de l'excès énantiomérique (Figure 2 C).

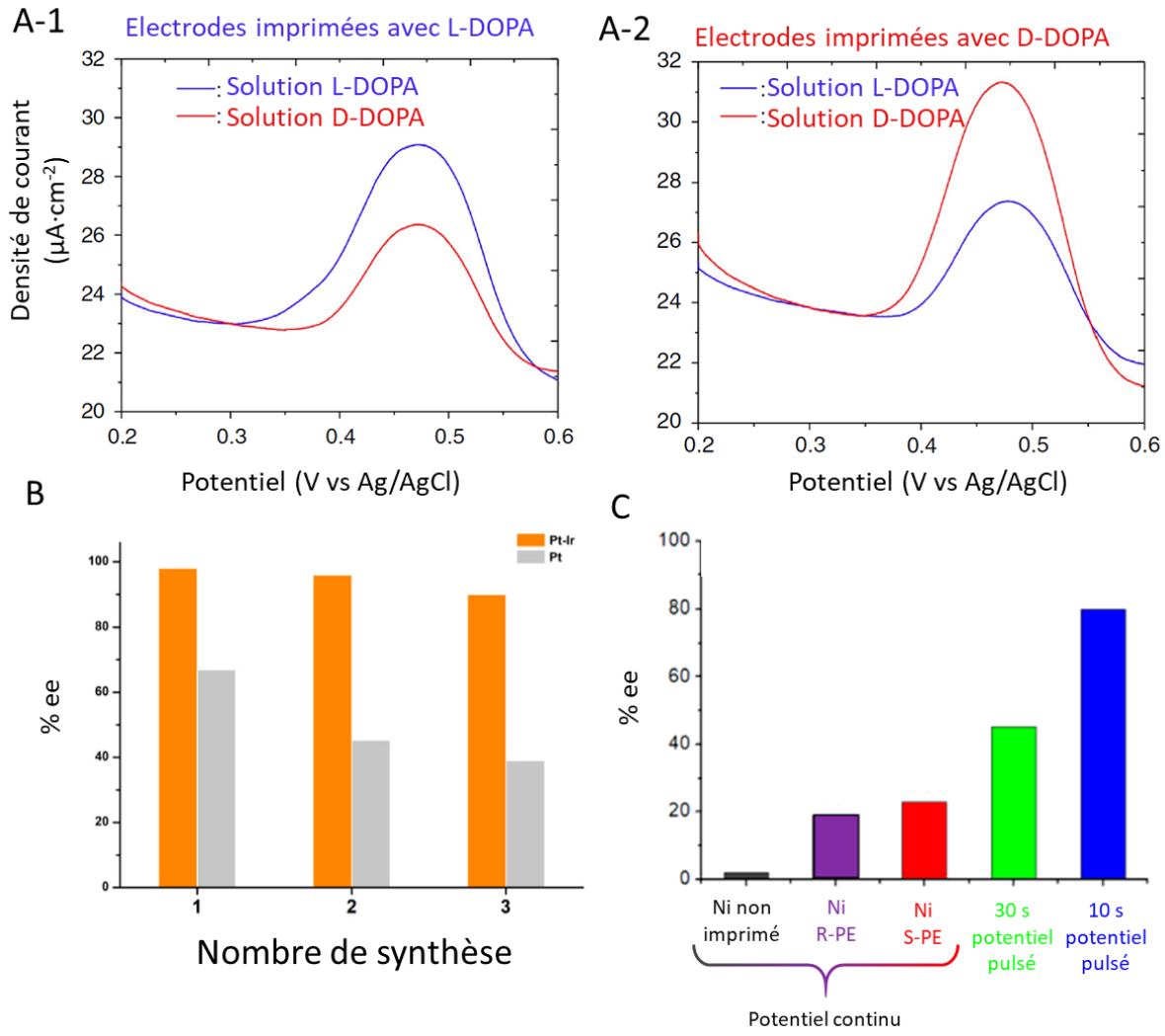

Figure 2: A) DPV réalisées avec des électrodes imprimées par la L-DOPA (A-1) et la D-DOPA (A-2), dans des solutions de 4mM L-DOPA (courbes bleues) et de 4 mM D-DOPA (courbes rouges) dans 50 mM HCl. Adaptée de [15]

B) Comparaison des excès énantiomériques obtenues en fin de synthèse (synthèse de phényléthanol à partir d'acétophénone) après 1, 2 puis 3 utilisations des électrodes en platine-iridium (orange) et en platine (gris). Adaptée de [16]

C) Comparaison des excès énantiomériques obtenues en fin de synthèse (synthèse de phényléthanol à partir d'acétophénone) avec un potentiel continu pour des électrodes en nickel non imprimée (noir), imprimée avec du R-PE (mauve), du S-PE (rouge), puis avec un potentiel pulsé avec des impulsions de 30 s (vert) et de 10 s (bleu). Adaptée de [17]

Dans le cadre de cette thèse, la possibilité de transposer ce concept au palladium a été étudiée. En effet, le palladium présente des propriétés catalytiques intéressantes pour l'hydrogénation de molécules.

Ainsi, le deuxième chapitre de cette thèse est dédié au palladium à l'échelle macroscopique. Tout d'abord, la réactivité des énantiomères de la molécule de DOPA à la

surface d'électrodes planes de palladium a été étudiée. Les voltampérogrammes montrent que l'oxydation du DOPA se produit au même potentiel que l'oxydation de la surface de palladium (Figure 3 A). Cette observation est un inconvénient, d'une part car les signaux d'oxydation se superposent et il sera donc difficile d'interpréter les données recueillies. D'autre part, l'oxydation de la surface de palladium modifie l'arrangement surfacique des atomes et devrait ainsi détruire l'empreinte moléculaire imprimée lors de l'électrodéposition. Finalement, il a été montré que le DOPA peut être adsorbé à la surface du palladium (Figure 3 B). L'adsorption permet de diminuer le potentiel d'oxydation et donc de distinguer l'oxydation du DOPA de celle du palladium. De plus, l'adsorption est réalisée avant toute modification de surface, ainsi les résultats obtenus sont directement corrélés avec la surface initiale de l'électrode.

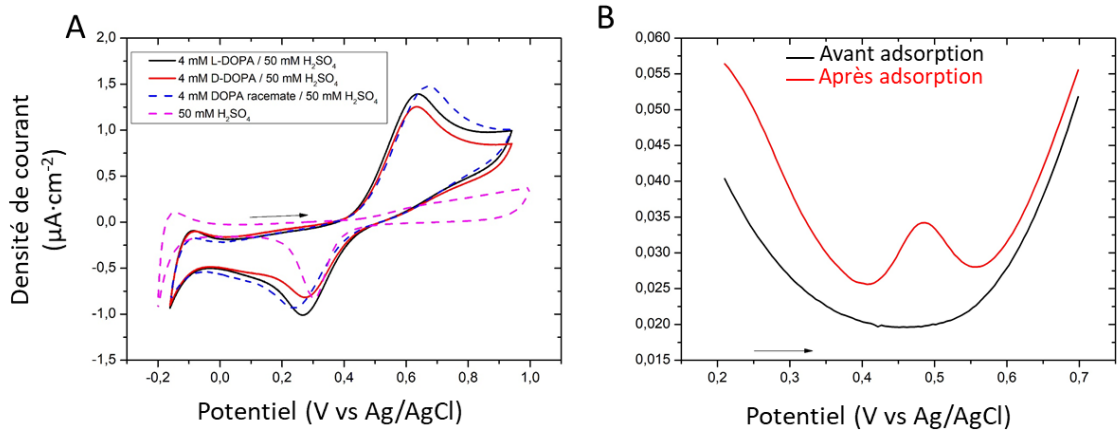

Figure 3: A) Voltampérométries cycliques réalisées avec une électrode commerciale de palladium avec des solutions de 4mM L-DOPA (noir), D-DOPA (rouge), mélange racémique de DOPA (pointillés bleus) et électrolyte support, 50 mM H_2SO_4 (pointillés magenta)

B) DPV réalisées avec une électrode commerciale de palladium dans l'électrolyte support (50 mM H_2SO_4) avant adsorption de molécules de DOPA (noir) et après adsorption (rouge)

Ensuite, il s'agit d'obtenir un dépôt de palladium présentant une nanostructuration qui induit une grande surface électroactive à l'échelle macroscopique. L'électrolyte est composé d'un surfactant non ionique en milieu aqueux et de sel de palladium à haute concentration pour former un cristal liquide. Les proportions utilisées sont telles que la phase lyotrope suit un arrangement hexagonal. Ainsi, l'électrodéposition des ions de palladium devrait donner accès à un film de palladium mésoporeux. L'impact de plusieurs paramètres sur la morphologie des dépôts a été étudié.

Différents potentiels d'électrodéposition ont été utilisés. Les dépôts obtenus avec les surpotentiels les plus élevés sont les dépôts les plus hétérogènes alors qu'avec des surpotentiels plus faibles, les dépôts sont plus homogènes mais présentent tout de même une forte rugosité de surface. L'augmentation de la température permet de diminuer la viscosité de l'électrolyte et d'ainsi améliorer la diffusion des ions palladium au travers de l'électrolyte. Il faut toutefois faire attention à ne pas trop chauffer l'électrolyte afin de conserver la phase hexagonale. Une température de 40 °C donne les meilleurs résultats bien que la surface reste très rugueuse. Le surfactant a également un impact sur la morphologie des dépôts. L'utilisation de surfactant « pur » (présence d'une seule longueur de molécule et non pas une distribution autour d'une longueur moyenne de chaîne carbonée) améliore nettement l'homogénéité des dépôts, bien que ceux-ci présentent toujours des irrégularités de surface. L'impact du traitement de surface du substrat ainsi que sa nature ont également été étudiés. Une légère diminution de la rugosité est observée en utilisant le platine comme matériau d'électrode de travail, et ce, quel que soit le traitement de surface effectué en amont. Finalement, la variation de la quantité de charge injectée au cours de l'électrodéposition nous a permis d'observer par microscopie électronique à balayage (**MEB**) la surface d'électrode à différentes étapes du procédé de déposition et semble confirmer que la diffusion des ions palladium est le paramètre déterminant du procédé d'électrodéposition (Figure 4). De plus, l'analyse par voltampérométrie cyclique indique que les dépôts obtenus ne sont pas mésoporeux (Figure 5).

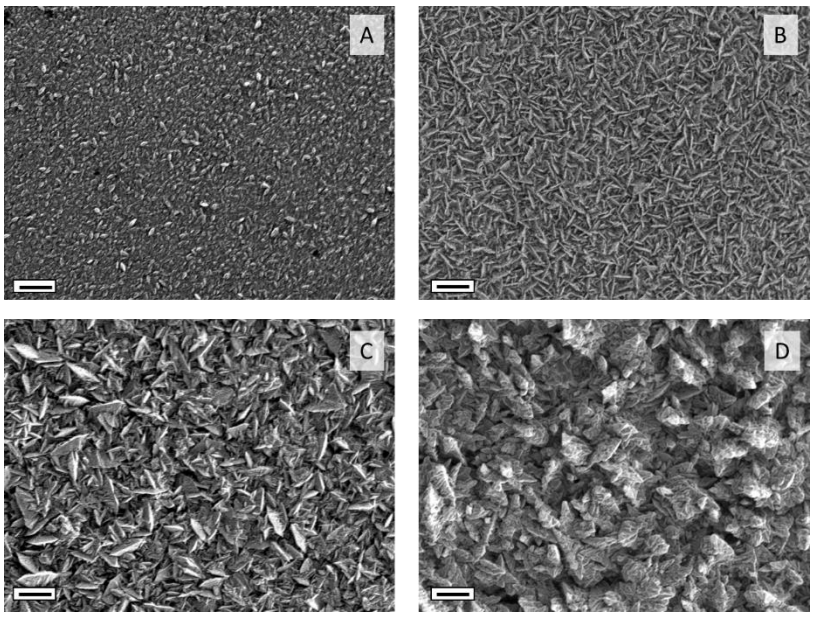

Figure 4: Images MEB des dépôts obtenus en fin de chronoampérométrie A) 0,5 C·cm^{-2}, B) 1 C·cm^{-2}, C) 2 C·cm^{-2}, D) 8 C·cm^{-2}. Barre d'échelle : 1 µm

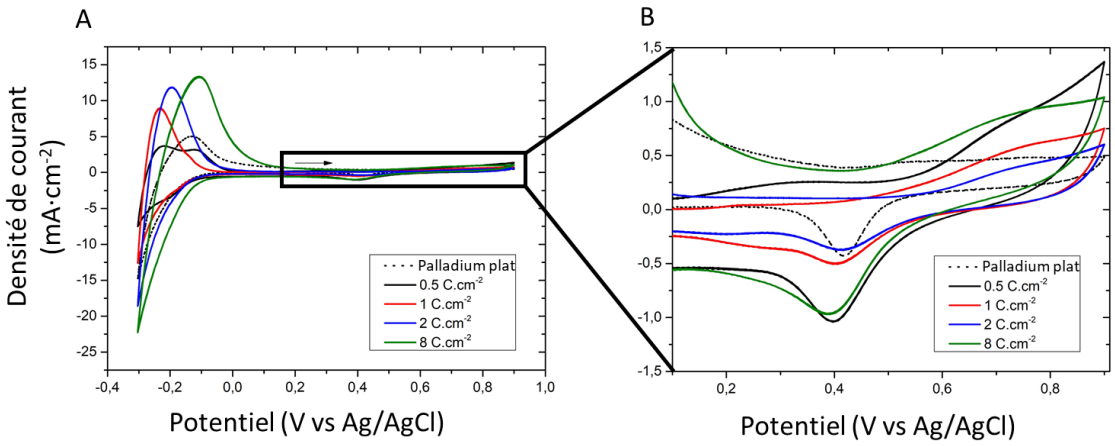

Figure 5: Voltampérométries cycliques effectuées dans 1 M H_2SO_4 avec les électrodes de palladium obtenues après chronoampérométrie pour 0,5 C·cm^{-2} (noir), 1 C·cm^{-2} (rouge), 2 C·cm^{-2} (bleu) et 8 C·cm^{-2} (vert) comparées à une électrode plane de palladium (pointillés noirs)

A partir de ces observations, l'utilisation d'ultramicroélectrodes (**UME**) semble être indiquée, puisque la diminution de la taille d'électrode permet l'établissement d'un régime de diffusion stationnaire et permet donc d'être moins limité par la diffusion des espèces (Chapitre 3). Des dépôts de palladium à partir du même électrolyte et dans les mêmes conditions ont été réalisés à la fois sur substrats macroscopiques et sur UME. Les images obtenues par MEB mettent en évidence l'apport très net des UME pour la diminution de la rugosité de surface des dépôts (Figure 6). De plus, la mesure de la surface électroactive par voltampérométrie cyclique fait état d'une grande surface disponible, 100 fois supérieure à la surface géométrique de l'électrode, ce qui est révélateur d'une nanostructuration.

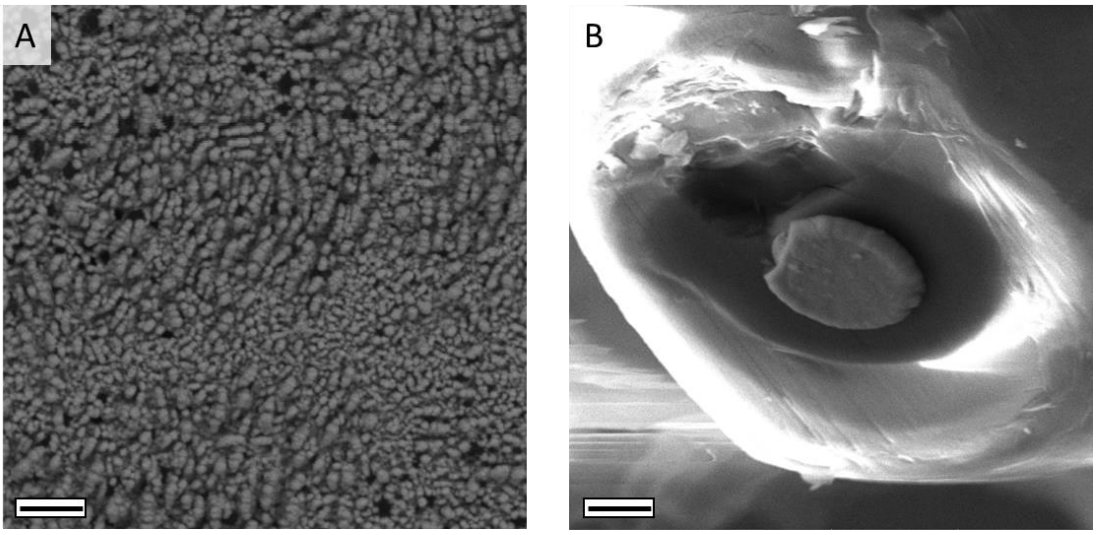

Figure 6: Images MEB des dépôts obtenus sur électrode macroscopique (A) et sur UME (b). Barre d'échelle : 5 µm

Ainsi, les dépôts suivants ont été réalisés en présence de molécules de DOPA afin d'induire une empreinte chirale. La chiralité de ces dépôts a ensuite été testée par DPV. Dans un premier temps, les voltampérogrammes ont été réalisés dans la solution de DOPA avec le palladium déposé comme électrode de travail. Les données enregistrées ne permettent pas de distinguer les énantiomères. En effet, la surface géométrique de l'électrode étant de l'ordre du micromètre, il est possible que la contribution de la surface externe (a priori, non imprimée) soit plus importante que celle de la surface interne (les mésopores qui contiennent l'empreinte chirale) en raison de l'élaboration d'un régime stationnaire quasi-immédiat. Ce qui expliquerait que la distinction des énantiomères par DPV en solution ne soit pas possible lorsque le film métallique chiral est supporté par une UME. Comme montré précédemment, le DOPA s'adsorbe spontanément à la surface du palladium. Les voltampérométries suivantes ont donc été réalisées par adsorption (Figure 7). La principale observation est le manque de reproductibilité des mesures qui se traduit par un grand écart type autour de la moyenne de la densité de charge liée à l'oxydation du DOPA adsorbé (Figure 8). L'hypothèse principale expliquant cette observation est une procédure de nettoyage de l'électrode inappropriée et qu'il faudra donc étudier par la suite.

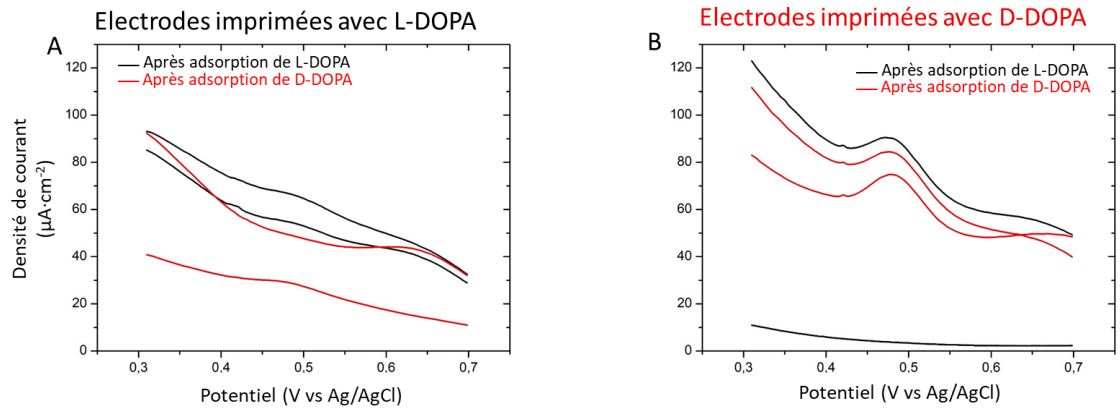

Figure 7: DPV réalisées avec des électrodes imprimées par la L-DOPA (A) et la D-DOPA (B) dans 50 mM H_2SO_4 après adsorption de L-DOPA (noir) et de D-DOPA (rouge)

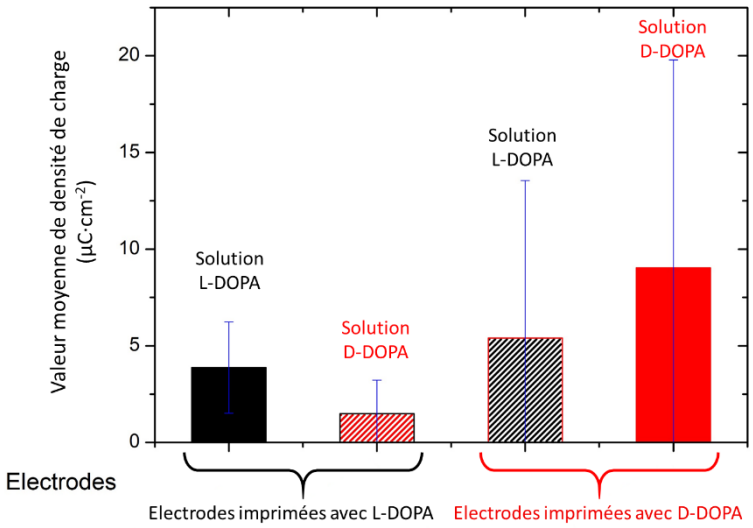

Figure 8: Analyse statistique des densités de charge mesurées par DPV liées à l'oxydation de la DOPA. Les statistiques ont été réalisés à partir de 80 mesures, 20 pour chaque catégorie

Alors que la première partie de cette thèse est dédiée à la chiralité à l'échelle moléculaire, la seconde partie est consacrée à la chiralité à plus large échelle. En effet, des matériaux chiraux, tels que des hélices en silice [18], ont été développés. L'objectif de ce chapitre a été de mettre au point un procédé permettant la modification de ces hélices de telle sorte à pouvoir induire un mouvement.

Pour cela, des dépôts autocatalytiques ainsi que la modification localisée par électrochimie bipolaire ont été réalisés sur des substrats de verre et de silice, de différentes géométries et à différentes échelles (Chapitre 4). Tout d'abord, des dépôts de nickel par procédé electroless ont été effectués pour créer une couche conductrice à la surface des différents substrats. Les plaques de verres ainsi modifiées ont été utilisées dans un montage classique à trois électrodes, en tant qu'électrode de travail pour enregistrer des voltampérogrammes linéaires, pour déterminer des valeurs de potentiels essentielles pour la mise en place des expériences en électrochimie bipolaire.

Trois électrolytes (contenant des ions de nickel, d'or ou de platine) ont été ainsi analysés pour déterminer celui qui sera le plus approprié pour la suite du projet. Les voltampérogrammes obtenus indiquent que l'électrolyte contenant les ions de platine est le plus adapté pour le but de ce projet, toutefois, des améliorations de formulations de ces électrolytes devraient être étudiés (Figure 9).

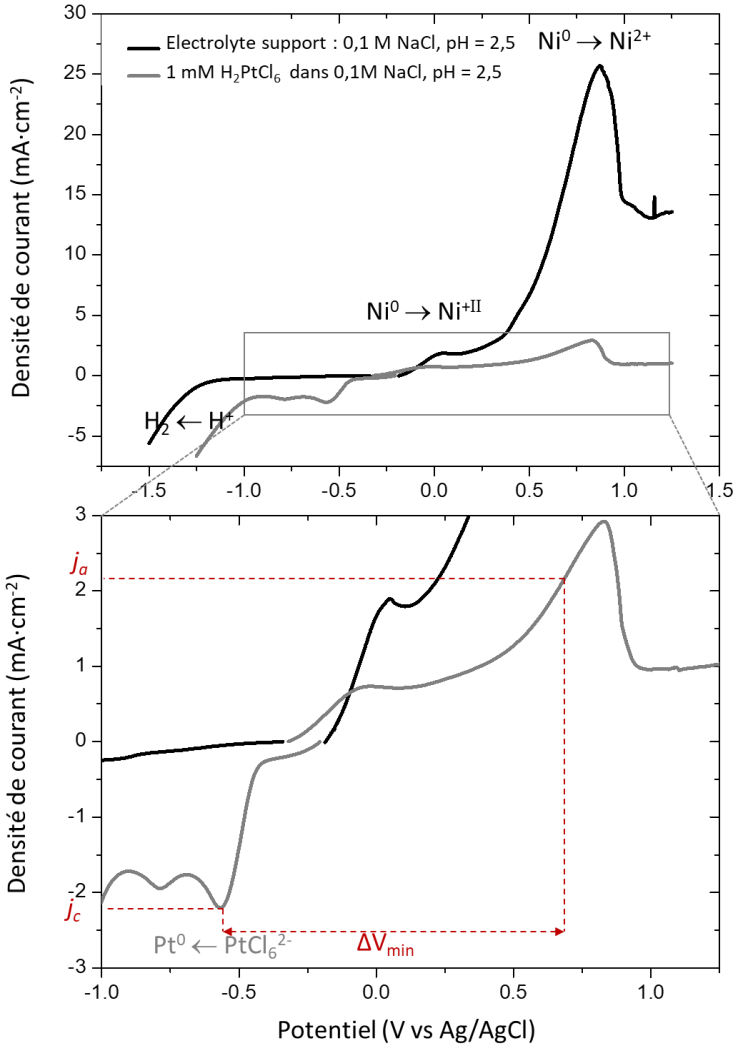

Figure 9: Voltampérogrammes obtenus à partir d'un électrolyte support (0,1 M NaCl, pH = 2,5, courbes noires) et à partir d'une solution contenant des ions de platine (1 mM H_2PtCl_6, 0,1 M NaCl, pH = 2,5) avec comme électrode de travail, des lames de verre recouvertes de nickel

Ensuite, l'électrochimie bipolaire a été utilisée pour modifier ces objets cœur-coquille. La variation du potentiel aux extrémités des électrodes bipolaires a montré qu'il était possible de déposer du platine au pôle cathodique. Curieusement, au-delà d'une certaine valeur, le platine a également été observé sur le pôle anodique alors qu'une expérience contrôle montre qu'il n'y a pas de dépôt spontané de platine. Une possible explication serait l'existence d'un mécanisme électrochimique-chimique. La première étape serait l'oxydation du nickel en nickel (II), sous la forme d'hydroxyde, d'oxyde ou de complexe. La seconde étape serait la réaction du nickel (II) avec le sel de platine présent en solution. Des billes de verre d'un millimètre de

diamètre ont également été utilisées comme substrats et il a été montré qu'il était possible de déposer du platine du coté cathodique tout en dissolvant le nickel du coté anodique (Figure 10).

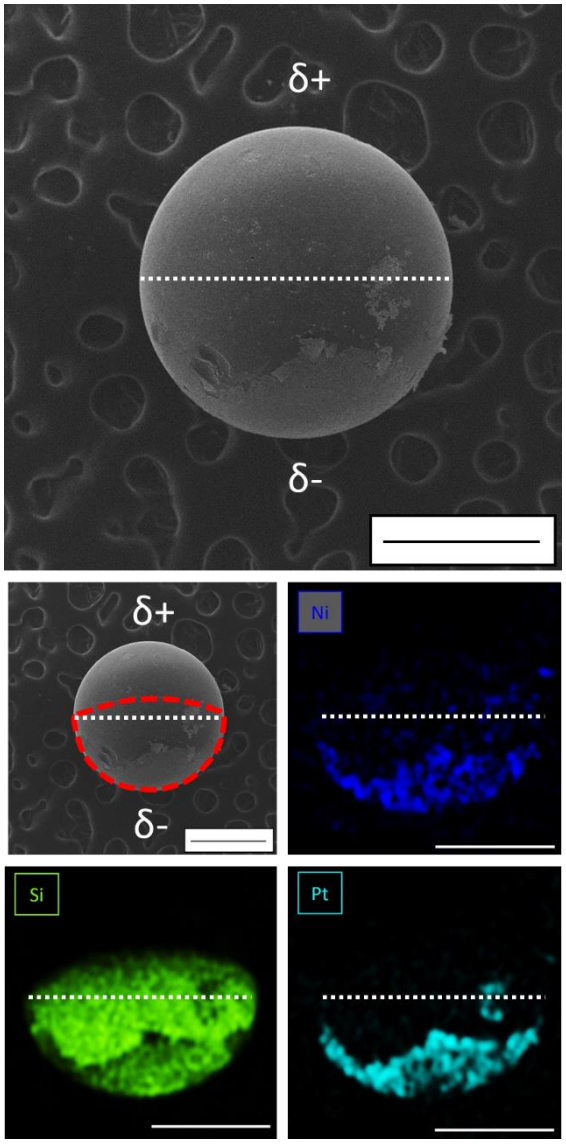

Figure 10: Images MEB et analyse élémentaire d'une bille de verre (1 mm de diamètre) recouverte de nickel après une expérience d'électrochimie bipolaire. Barre d'échelle : 500 µm

Par la suite, le dépôt electroless de nickel a été effectué sur des billes de verres d'environ 250 µm de diamètre. Les images par MEB ainsi que la spectroscopie de rayons X à dispersions d'énergie montrent que les billes sont partiellement recouvertes de nickel, probablement dû à des chocs mécaniques qui ont eu un effet abrasif localement (Figure 11 A). Finalement, la modification par voie electroless a été essayée avec des billes de silice de 1 µm de diamètre. Les différentes analyses ne révèlent pas la présence de nickel à la surface des billes (Figure 11 B). De nombreuses hypothèses doivent être étudiées pour comprendre cette observation,

comme une sensibilisation peu voire pas efficace de la surface des billes ou encore un nombre de billes insuffisant présent dans le bain électrolytique.

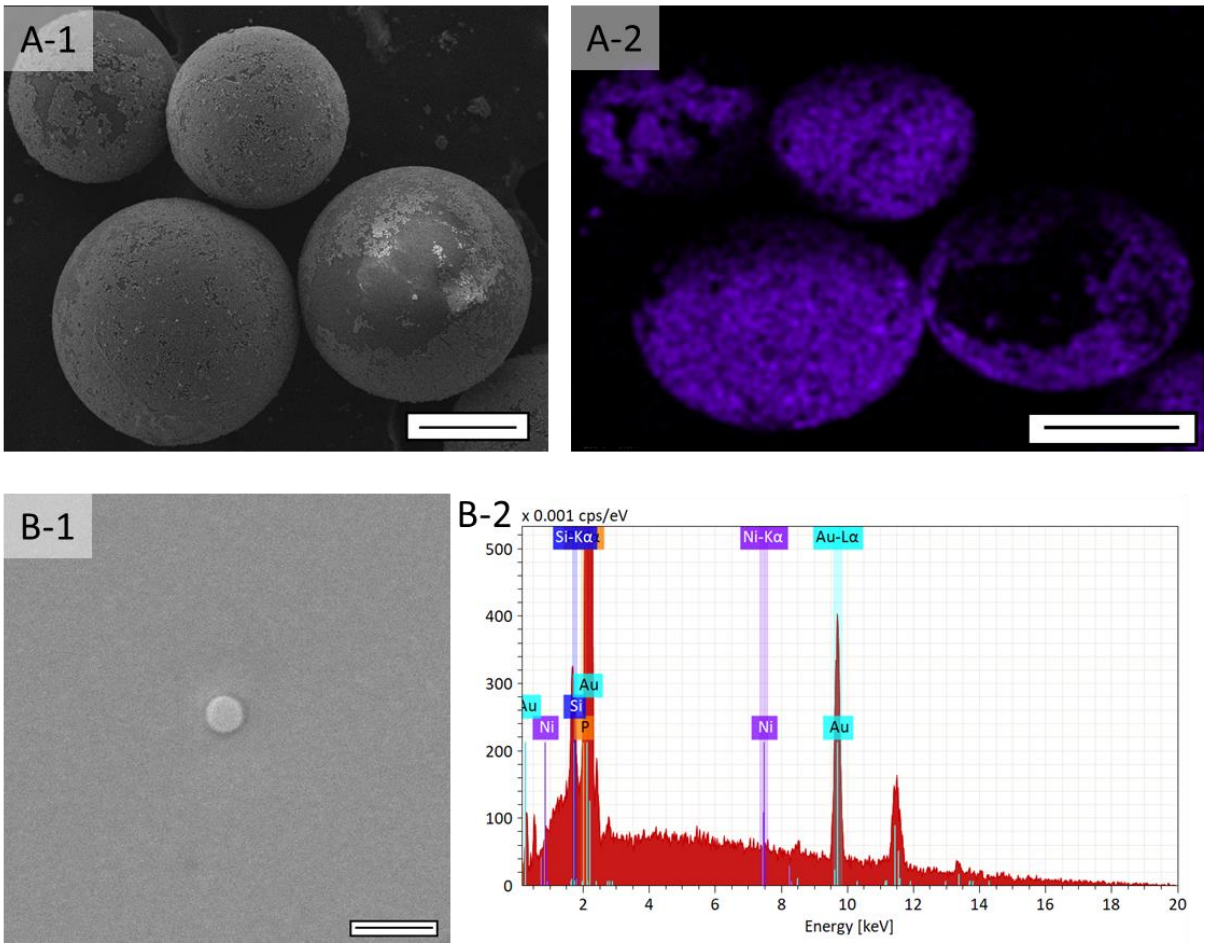

Figure 11: A) Images MEB et analyse élémentaire de billes de verre d'environ 250 µm de diamètre après déposition de nickel. Barre d'échelle : 100 µm

B) Image MEB (B-1) et spectre (B-2) d'une bille de silice de 1µm de diamètre déposée sur une lame d'or après déposition de nickel. Barre d'échelle : 2 µm

Finalement, cette thèse a été consacrée, d'une part, à l'induction d'une propriété chirale dans un film métallique afin d'en faire un matériau énantiosélectif, d'autre part, à la modification d'objets non conducteur par dépôt autocatalytique puis par électrochimie bipolaire en vue de modifier des hélices en silice.

Le palladium, montrant des propriétés catalytiques intéressantes pour les réactions d'hydrogénation a été choisi afin d'améliorer le rendement obtenu jusqu'alors avec le platine, platine-iridium et le nickel. Il a été montré que les dépôts synthétisés à l'échelle macroscopique présentaient de fortes irrégularités de surface. De plus, les voltampérométries cycliques ne mettent pas en évidence la présence de mésopores. Ainsi, les dépôts ont été conduits sur ultramicroélectrodes (qui permettent l'élaboration d'un régime stationnaire quasi-

instantanément). La morphologie des dépôts est nettement améliorée et les premiers essais de reconnaissance chirale ont été effectués. Malheureusement, les statistiques sur les résultats obtenus montrent une forte disparité des résultats ne permettant pas de conclure quant à la sélectivité des électrodes. Les futurs travaux devront être axés sur l'élaboration d'un protocole permettant l'obtention de résultats reproductibles avant de s'intéresser à la synthèse asymétrique.

La deuxième partie de cette thèse a été dédiée à la modification d'objets non conducteurs. Dans un premier temps, des objets (plaques et billes de verre, de l'ordre du centimètre puis du millimètre) ont été recouverts de nickel par un procédé autocatalytique. Les objets cœur-coquille ainsi obtenus ont ensuite été utilisés en tant qu'électrode bipolaire afin de modifier localement la couche de nickel, induisant une asymétrie par polarisation sélective des extrémités de l'objet. Pour des plus petits objets (250 µm et 1 µm), le dépôt de nickel doit être amélioré afin de pouvoir conduire des expériences d'électrochimie bipolaire.

Références

[1] V. Farina, J. T. Reeves, C. H. Senanayake, J. J. Song, *Chem. Rev.* **2006**, *106*, 2734.

[2] W. Liu, J. Gan, D. Schlenk, W. A. Jury, *Proceedings of the National Academy of Sciences* **2005**, *102*, 701.

[3] A. Larios, H. S. Garcia, R. M. Oliart, G. Valerio-Alfaro, *Appl Microbiol Biotechnol* **2004**, *65*, 373.

[4] H.-U. Blaser, B. Pugin, F. Spindler, *Journal of Molecular Catalysis A: Chemical* **2005**, *231*, 1.

[5] T. J. Ward, K. D. Ward, *Anal. Chem.* **2010**, *82*, 4712.

[6] P. L. Polavarapu, *Chiroptical spectroscopy: fundamentals and applications*, Taylor & Francis, Boca Raton, **2017**.

[7] T. R. Hoye, C. S. Jeffrey, F. Shao, *Nat Protoc* **2007**, *2*, 2451.

[8] M. Ortega Lorenzo, C. J. Baddeley, C. Muryn, R. Raval, *Nature* **2000**, *404*, 376.

[9] D. S. Sholl, A. Asthagiri, T. D. Power, *J. Phys. Chem. B* **2001**, *105*, 4771.

[10] N. M. Maier, W. Lindner, *Anal Bioanal Chem* **2007**, *389*, 377.

[11] J. A. Switzer, H. M. Kothari, P. Poizot, S. Nakanishi, E. W. Bohannan, *Nature* **2003**, *425*, 490.

[12] G. S. Attard, *Science* **1997**, *278*, 838.

[13] D. J. Mitchell, G. J. T. Tiddy, L. Waring, T. Bostock, M. P. McDonald, *J. Chem. Soc., Faraday Trans. 1* **1983**, *79*, 975.

[14] A. M. Figueiredo Neto, S. R. A. Salinas, *The physics of lyotropic liquid crystals: phase transitions and structural properties*, Oxford University Press, New York, **2005**.

[15] C. Wattanakit, Y. B. S. Côme, V. Lapeyre, P. A. Bopp, M. Heim, S. Yadnum, S. Nokbin, C. Warakulwit, J. Limtrakul, A. Kuhn, *Nat Commun* **2014**, *5*, 3325.

[16] S. Butcha, S. Assavapanumat, S. Ittisanronnachai, V. Lapeyre, C. Wattanakit, A. Kuhn, *Nat Commun* **2021**, *12*, 1314.

[17] S. Assavapanumat, M. Ketkaew, A. Kuhn, C. Wattanakit, *J. Am. Chem. Soc.* **2019**, *141*, 18870.

[18] J. Cheng, G. Le Saux, J. Gao, T. Buffeteau, Y. Battie, P. Barois, V. Ponsinet, M.-H. Delville, O. Ersen, E. Pouget, R. Oda, *ACS Nano* **2017**, *11*, 3806.

Table of contents

List of abbreviations

AAO	Anodic aluminum oxide
AE	Acetophenone
BE	Bipolar electrode
BEC	Bipolar electrochemistry
BED	Bipolar electrodeposition
BQ	Benzoquinone
CA	Chronoamperometry
CABED	Capillary-assisted bipolar electrodeposition
CMME	Chiral mesoporous metal electrode
CV	Cyclic voltammetry
DOPA	Dihydroxy-3,4-phenylalanine
DPV	Differential pulse voltammetry
ECD	Electrochemical deposition
ECL	Electrochemiluminescence
EDS	Energy dispersive X-ray spectroscopy
ee	Enantiomeric excess
ELD	Electroless deposition
EP	Electrophoretic paint
HER	Hydrogen evolution reaction
HPLC	High-performance liquid chromatography
HQ	Hydroquinone
IBED	Indirect bipolar electrodeposition
ITO	Indium tin oxide

JP	Janus particles
LLC	Lyotropic liquid crystal
LSV	Linear sweep voltammetry
MA	Mandelic acid
MIP	Molecular imprinted polymers
NHE	Normal hydrogen electrode
OCP	Open-circuit potential
ORR	Oxygen reduction reaction
PE	Phenylethanol
PGA	Phenylglyoxylic acid
Ppy	Polypyrrole
RDE	Rotating disk electrode
RT	Room temperature
SEM	Scanning electron microscope
SE	Supporting electrolyte
TEM	Transmission electron microscopy
UME	Ultramicroelectrode
WE	Working electrode
XRD	X-Ray Diffraction

General introduction

I. Generalities

What is the common feature between hands, the shell of snails, limonene and helices? There are all characterized by chirality. From a general point of view, chirality is the property of an object of not being superimposable to its mirror image. This feature implies a lack of symmetry inducing an asymmetric center, a chiral axis or a chiral plane.

Molecules are among these objects. A large number of chiral molecules are of great interest for our society since they are widely used in pharmaceutics[1], agriculture[2] or fragrances[3]. In this case, the two "mirror images" are called enantiomers. They have the same global composition, but a different arrangement in space. This difference may cause very different biological effects. Regarding drugs, for instance, one enantiomer may be used to heal one disease while the other enantiomer may be useful for another disease, be inactive or even be toxic.

From these statements, it is clear why chirality has become a major concern for scientists and society. Thereby, many researches have been conducted in this field, trying to provide reliable methodologies to synthesize enantiomerically pure compounds, to separate mixtures of enantiomers and to analyze and identify each of the enantiomer.

More recently, evolution of processes has given access to chiral objects and allows the breaking of the symmetry of numerous objects from the macroscopic scale to the nanoscale. Asymmetric particles are receiving a great deal of attention upon the development of Janus particles (**JP**), in reference to the roman's God. These objects have the particularity of exhibiting different properties with respect to their local modification. They can, for example, act as amphiphilic molecules or be sensitive to a magnetic or electrical field.

II. Molecular chirality

The first part of this thesis will be devoted to molecular chirality which is of huge interest for the scientific community. Actually, it is a concern of society since chiral molecules are widely present in our daily life. In an achiral environment, enantiomers have the same physical and chemical properties. So, how a pure enantiomer can be obtained?

The easiest scenario is a synthesis leading preferentially to one form, called asymmetric synthesis [4]. In this case, it might not be necessary to separate the products, depending on the proportion of each enantiomer (the enantiomeric excess). For this purpose, chiral pool [5,6], biocatalysis [7,8] or chemocatalysis [9,10] are efficient strategies.

A more complicated scenario is when synthesis leads to a racemic mixture (equimolar mixture of enantiomer), where, in most cases, chiral separation (or resolution) [11] must be performed after the synthesis in order to obtain pure enantiomers. For such separations, several techniques exist. The most common one is chromatography, specifically high-performance liquid chromatography (**HPLC**) [12]. Supercritical fluid chromatography is also efficient for this kind of separation and appears to be more ecofriendly [13]. Apart from chromatography, electromigration techniques are another type of method for chiral resolution [14]. Finally, crystallization [15] and kinetic resolution [16] can also be used for this goal.

As mentioned above, enantiomers are quite hard to be distinguished since they have similar physico-chemical properties. Therefore, several methods of enantiodifferentiation have been developed to analyze the resulting mixture of a synthesis or a separation and determine the proportion of each enantiomer in the media. These techniques are either based on chiroptical spectroscopies [17,18], such as optical rotation [19] or circular dichroism [20]. Nuclear magnetic resonance spectroscopy can also be used to allow the differentiation of enantiomer but requires the use of a chiral auxiliary which interacts with the analyte [21].

III. Asymmetric particles

The second part of the thesis will deal with the synthesis of asymmetric objects. These particles are composed of different materials which are spatially separated and thus, provide

locally specific physico-chemical properties. The interest in these particles is continuously increasing since the end of the 1980s. De Gennes described for the first time particles being hydrophilic on one side and hydrophobic on the other side [22], like an amphiphilic molecule. Nowadays, many pathways for their synthesis have been developed, giving access to a wide range of particles [23].

The main approach to synthesize asymmetric particles is the use of an interface and to immobilize initially homogeneous particles by a reversible binding (physical or chemical) [24–26]. After the immobilization, the modification of the exposed site can be performed by several methods (molecular functionalization [27], metal sputtering [28], electroless deposition [29] …). Afterwards, the particles are released from the interface and bi-functional particles are obtained. This pathway offers a good regularity among the synthesized particles. However, the use of an interface limits the production since in one experiment only the equivalent of one monolayer of particles can be synthesized.

Other possibilities are the use of templates (such as aluminum oxide [30]), colloidal crystallization [31] or microfluidic approaches [32]. All these processes are robust and allow achieving a good homogeneity of the particles. The amount of synthesized asymmetric particles can be enough for the laboratory scale. However, a scale-up for industrial applications might be difficult. Therefore, bulk methods were developed in order to produce asymmetric particles in bigger quantities.

A first example is the use of emulsions such as Pickering emulsion [33] or seeded emulsion polymerization [34]. However, these approaches still require the presence of an interface. Polymerization techniques associated with metallic nanoparticles are among the most developed synthesis method without interfaces [35].

The use of an external electric field can also allow a straightforward access to asymmetric particles as exemplified by bipolar electrochemistry (**BEC**) [36]. Indeed, this method enables the modification of conducting materials based on the opposite polarization of each side, inducing different electrochemical reactions. This process will be developed in more detail in the fourth chapter.

The variety of existing particles gives them tremendous potential to be applied in many different fields. Due to their amphiphilic behavior, these objects have the capability to self-assemble and can thus be used as emulsion stabilizers [37,38], or as precursors to form superstructures [39,40]. Some studies also show an increase in hydrophobicity when compared

with homogeneous particles qualifying them as super hydrophobic and thus, allowing their use as water repellent [41].

Also, the anisotropy of the particles opens the possibility to induce motion. One option is to deposit a ferromagnetic material on one side and control the orientation with a magnetic field [42]. The orientation can also be controlled with a *d.c.* electric field. This ability allows the use of these particles in e-paper technology [43]. It can also provide autonomous microswimmers by modifying one side of the particle by a chemically active entity such as an enzyme [44] or other catalysts [45,46]. One very popular approach is the use of hydrogen peroxide as a fuel, combined with a catalyst (platinum for instance).

In the first part of this thesis, we tried to developed new materials with catalytic properties to perform enantiorecognition as well as asymmetric synthesis of enantiomers. It is a major concern to provide reliable technologies to obtain enantiomerically pure compounds.

In the first chapter, we will discuss chiral features induced in or on metals enabling chiral electrochemistry. Then, the possibility of increasing the surface area of an electrode by using a lyotropic liquid crystal (**LLC**) phase will be presented. Finally, the combination of this type of nanostructuration with a molecular imprinting approach will be shown.

The second chapter will be devoted to the electrodeposition of palladium at the macroscale. First, its electrochemical reactivity will be discussed as well as the reactivity of dihydroxy-3,4-phenylalanine (**DOPA**) at a bare palladium electrode, followed by its structuration by using a LLC phase.

The third chapter will present the synthesis of palladium at ultramicroelectrodes. The deposition at the macro- and microscale will be compared. Then, the results regarding the oxidation of DOPA at chirally-imprinted mesoporous metal electrodes (**CMME**) will be discussed.

The second part will be treated in the fourth and last chapter. It will present the use of BEC at core-shell structures, where the shell is the only conductive part at the macro- and micro-scale. Firstly, the principle and some applications of BEC will be presented. Afterwards, conventional electrochemistry will be used to provide crucial information for BEC experiments. Finally, core-shell structures will be studied with respect to their use for the electrochemical modifications. This work represents the first step for the modification of a wider range of objects such as silica nanohelices.

IV. References

[1] V. Farina, J. T. Reeves, C. H. Senanayake, J. J. Song, *Chem. Rev.* **2006**, *106*, 2734.

[2] W. Liu, J. Gan, D. Schlenk, W. A. Jury, *Proc. Natl. Acad. Sci.* **2005**, *102*, 701.

[3] A. Larios, H. S. Garcia, R. M. Oliart, G. Valerio-Alfaro, *Appl. Microbiol. Biotechnol.* **2004**, *65*, 373.

[4] H.-U. Blaser, B. Pugin, F. Spindler, *J. Mol. Catal. Chem.* **2005**, *231*, 1.

[5] J. E. Aaseng, O. R. Gautun, *Tetrahedron* **2010**, *66*, 8982.

[6] H. U. Blaser, *Chem. Rev.* **1992**, *92*, 935.

[7] R. Wohlgemuth, *Curr. Opin. Microbiol.* **2010**, *13*, 283.

[8] E. Ricca, B. Brucher, J. H. Schrittwieser, *Adv. Synth. Catal.* **2011**, *353*, 2239.

[9] K. L. Jensen, G. Dickmeiss, H. Jiang, Ł. Albrecht, K. A. Jørgensen, *Acc. Chem. Res.* **2012**, *45*, 248.

[10] H. Fernández-Pérez, P. Etayo, A. Panossian, A. Vidal-Ferran, *Chem. Rev.* **2011**, *111*, 2119.

[11] T. J. Ward, K. D. Ward, *Anal. Chem.* **2010**, *82*, 4712.

[12] M. Tang, J. Zhang, S. Zhuang, W. Liu, *TrAC Trends Anal. Chem.* **2012**, *39*, 180.

[13] C. West, *Curr. Anal. Chem.* **2013**, *10*, 99.

[14] G. Gübitz, M. G. Schmid, *J. Chromatogr. A* **2008**, *1204*, 140.

[15] A. Collet, *Angew. Chem. - Int. Ed.* **1998**, *37*, 3239.

[16] E. Vedejs, M. Jure, *Angew. Chem. Int. Ed.* **2005**, *44*, 3974.

[17] P. L. Polavarapu, *Chiroptical spectroscopy: fundamentals and applications*, Taylor & Francis, Boca Raton, **2017**.

[18] T. Daniel. Crawford, *Theor. Chem. Acc.* **2006**, *115*, 227.

[19] L. Kott, W. Brian Holzheuer, M. M. Wong, G. K. Webster, *J. Pharm. Biomed. Anal.* **2007**, *43*, 57.

[20] P. Salvadori, C. Rosini, C. Bertucci, *J. Org. Chem.* **1984**, *49*, 5050.

[21] T. R. Hoye, C. S. Jeffrey, F. Shao, *Nat. Protoc.* **2007**, *2*, 2451.

[22] P.-G. de Gennes, *Angew. Chem. Int. Ed. Engl.* **1992**, *31*, 842.

[23] J. Du, R. K. O'Reilly, *Chem. Soc. Rev.* **2011**, *40*, 2402.

[24] L. Petit, J.-P. Manaud, C. Mingotaud, S. Ravaine, E. Duguet, *Mater. Lett.* **2001**, *51*, 478.

[25] S. Yang, J. Xu, Z. Wang, H. Zeng, Y. Lei, *J. Mater. Chem.* **2011**, *21*, 11930.

[26] S. Pradhan, L. E. Brown, J. P. Konopelski, S. Chen, *J. Nanoparticle Res.* **2009**, *11*, 1895.

[27] X. Y. Ling, I. Y. Phang, C. Acikgoz, M. D. Yilmaz, M. A. Hempenius, G. J. Vancso, J. Huskens, *Angew. Chem. Int. Ed.* **2009**, *48*, 7677.

[28] Y. Lu, H. Xiong, X. Jiang, Y. Xia, M. Prentiss, G. M. Whitesides, *J. Am. Chem. Soc.* **2003**, *125*, 12724.

[29] J.-Q. Cui, I. Kretzschmar, *Langmuir* **2006**, *22*, 8281.

[30] T. R. Kline, M. Tian, J. Wang, A. Sen, M. W. H. Chan, T. E. Mallouk, *Inorg. Chem.* **2006**, *45*, 7555.

[31] O. D. Velev, *Science* **2000**, *287*, 2240.

[32] A. B. Subramaniam, M. Abkarian, H. A. Stone, *Nat. Mater.* **2005**, *4*, 553.

[33] Y. Yang, Z. Fang, X. Chen, W. Zhang, Y. Xie, Y. Chen, Z. Liu, W. Yuan, *Front. Pharmacol.* **2017**, *8*, 287.

[34] E. B. Mock, C. F. Zukoski, *Langmuir* **2010**, *26*, 13747.

[35] A. Ohnuma, E. C. Cho, P. H. C. Camargo, L. Au, B. Ohtani, Y. Xia, *J. Am. Chem. Soc.* **2009**, *131*, 1352.

[36] G. Loget, J. Roche, A. Kuhn, *Adv. Mater.* **2012**, *24*, 5111.

[37] B. P. Binks, P. D. I. Fletcher, *Langmuir* **2001**, *17*, 4708.

[38] Y. K. Takahara, S. Ikeda, S. Ishino, K. Tachi, K. Ikeue, T. Sakata, T. Hasegawa, H. Mori, M. Matsumura, B. Ohtani, *J. Am. Chem. Soc.* **2005**, *127*, 6271.

[39] S. Park, *Science* **2004**, *303*, 348.

[40] Z. Mao, H. Xu, D. Wang, *Adv. Funct. Mater.* **2010**, *20*, 1053.

[41] S. Berger, L. Ionov, A. Synytska, *Adv. Funct. Mater.* **2011**, *21*, 2338.

[42] G. Loget, G. Larcade, V. Lapeyre, P. Garrigue, C. Warakulwit, J. Limtrakul, M.-H. Delville, V. Ravaine, A. Kuhn, *Electrochimica Acta* **2010**, *55*, 8116.

[43] B. Comiskey, J. D. Albert, H. Yoshizawa, J. Jacobson, *Nature* **1998**, *394*, 253.

[44] N. Mano, A. Heller, *J. Am. Chem. Soc.* **2005**, *127*, 11574.

[45] Y. Wang, R. M. Hernandez, D. J. Bartlett, J. M. Bingham, T. R. Kline, A. Sen, T. E. Mallouk, *Langmuir* **2006**, *22*, 10451.

[46] J. G. Gibbs, Y.-P. Zhao, *Appl. Phys. Lett.* **2009**, *94*, 163104.

Chapter I – Chirality at surfaces

The omnipresence of chiral molecules makes them of great interest for research and industry. They are especially present in medicine, biology and chemistry. They have the particularity of existing under two similar arrangements called enantiomers. Enantiomers have the same chemical composition, but different spatial arrangements of the constituting atoms, leading to mirror symmetry. This difference has consequences. In case of drugs, one form can treat a disease whereas the other form is inactive in the best case, have a different effect or can be toxic in the worst case. Another example is in perfumery; two enantiomers can have a different smell as it is the case for the limonene enantiomers.

As enantiomers have identical physico-chemical properties, except their interaction with polarized light, it is very difficult to differentiate, separate or selectively synthesize them. Numerous methods and technologies have been developed so far. This chapter is devoted to chiral surfaces. Some of them can be used for enantiodifferentiation or asymmetric synthesis thanks to catalytic properties of the substrates.

First, some techniques to design chiral surfaces will be presented, as the adsorption of molecules on achiral substrates or the exposition of high Miller index planes as well as the molecular imprinting of polymer. The elaboration of mesoporous materials will also be described. Finally, the combination of the mesoporosity and chiral impression at metallic surfaces will be presented.

I. Chiral surfaces

Chiral surfaces represent a promising technology to develop asymmetric synthesis as well as enantiorecognition and separation of enantiomers. Such surfaces can be obtained either by interaction between a surface and a molecule (adsorption or impression) or by slicing crystals to exhibit high Miller index faces.

I.1. Adsorption of molecules on achiral substrates

The adsorption of molecules onto achiral metal appears to be the most used process to produce chiral surfaces. In order to study the interaction between adsorbates and surface, it is necessary to combine several techniques of analysis [1].

The adsorption of achiral molecules onto achiral substrates can lead to local chirality. It can result either in a point chirality (molecule-induced) or an organizational chirality implying the existence of chiral domains. However, the resulting substrate remains globally achiral as there is an equal probability for the molecules to assemble in one or the other spatial arrangement [2]. Humblot *et al.* studied the adsorption of succinic acid onto Cu (110) using several techniques of spectroscopy, diffraction and microscopy [3]. These complementary techniques allowed them to collect chemical and organizational data about the adsorbed layer. They demonstrated the existence of chiral domains resulting from the presence of the adsorbates and observed that there is an equal proportion of domains of each chirality (Figure 12).

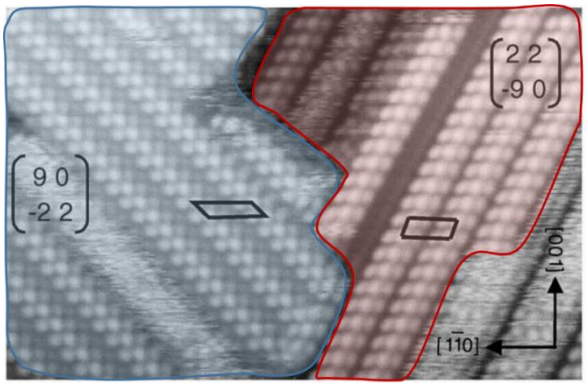

Figure 12: Scanning tunneling microscope image (260 Å×170 Å) of succinate adsorbates on Cu (110) showing the existence of the two enantiomorph phases. Adapted from [3]

One the other hand, the adsorption of chiral molecules leads to a unique domain and thus, a global chirality. In comparison to succinic acid, Humblot *et al.* studied also the adsorption of tartaric acid onto Cu (110) surface using the same methods of analysis [3]. They revealed the presence of a preferential chiral domain depending on the chirality of the adsorbate (Figure 13). A surface obtained by adsorbing (R,R)-tartaric acid shows a mirror organization compared to a surface obtained with (S,S)-tartaric acid.

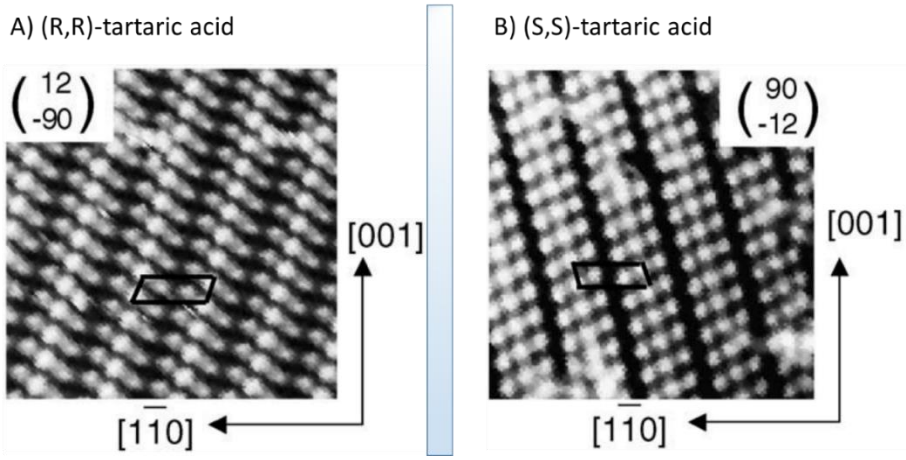

Figure 13: Scanning tunneling microscope images (108 Å×108 Å) of tartrate adsorbates on Cu (110) showing a distinct phase for (R,R)-tartaric acid (A) and (S,S)-tartaric acid (B). Adapted from [4]

These studies show the possibility to generate chiral properties on an achiral substrate by the adsorption of a chiral modifier. Thus, such modified surfaces were developed to be used in enantioselective synthesis. Among the most used configurations are the association of cinchona alkaloid with platinum [5,6] and tartaric acid with nickel [7,8] for the hydrogenation of ketones.

In these cases, it is important to note that the enantioselectivity originates from a chiral adsorbate and thus, the chirality disappears when the adsorbate leaves the surface which is a limitation of this concept.

I.2. Structural chiral surfaces

Metals are interesting for synthesis due to their catalytic properties. However, in the scope of asymmetric synthesis, their structures, which in general are highly symmetric, do not allow their use for this purpose. This drawback has been circumventing by using high Miller

index surfaces. Indeed, the presence of kink sites on such surfaces allows a differentiation of reactivity (Figure 14).

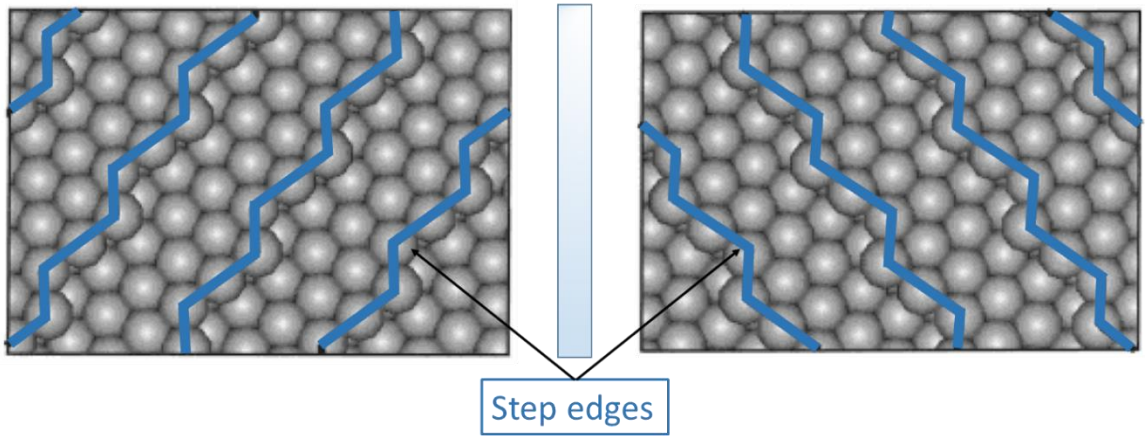

Figure 14: Model of examples of two enantiomeric surfaces. Adapted from [9]

Attard *et al.* reported the use of Pt {643} and Pt {531} to differentiate D- and L-glucose by electro-oxidation [10,11]. They used the platinum surface as a working electrode (**WE**) to record cyclic voltammetry (**CV**). The electrodes shows a difference in current density depending on the enantiomer in solution (Figure 15). These experiments opened the possibility to combine chirality with electrochemistry by using chiral metallic surfaces.

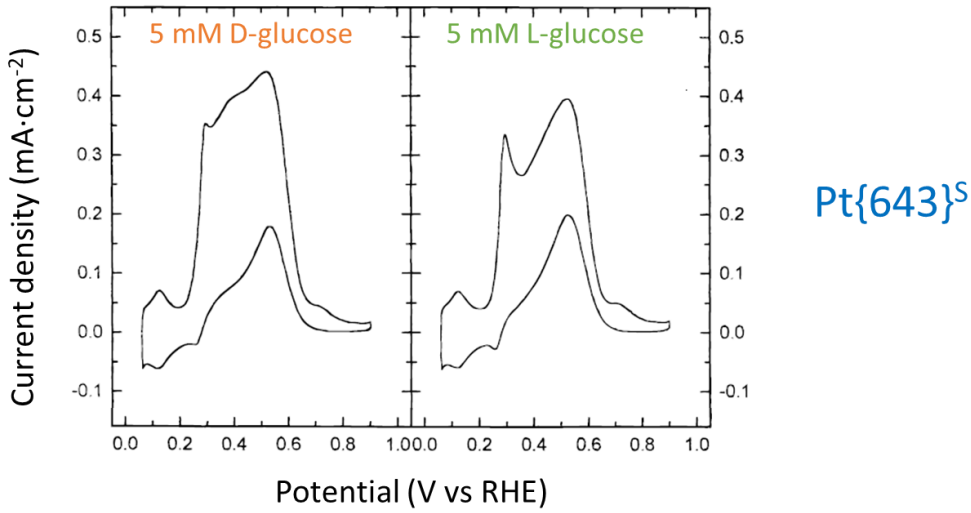

Figure 15: CV recorded in 0.05 M H_2SO_4 and 5 mM of glucose with a sweep rate of 50 mV·s^{-1}. Adapted from [10]

Switzer *et al.* developed another way of producing chiral catalysts by electrochemical deposition (**ECD**) [12]. In the presence of tartrate ions, they electrodeposited a copper oxide film onto a gold surface. Copper oxide presents a monoclinic structure and was studied by X-Ray Diffraction (**XRD**) and X-Ray pole figures. The XRD patterns show a strong orientation of the

copper oxide film and the X-Ray pole figures were used to determine the absolute configuration of copper films. The experiments show that the chirality of the electrodeposited film depends on the enantiomer present in solution during electrodeposition. Afterwards, they performed linear sweep voltammetry (**LSV**) with the obtained copper films to demonstrate the possibility of enantiodifferentiation. These electrochemical measurements reveal a different oxidation signal for a given enantiomer depending on the chirality of the electrodes (Figure 16). They also performed a control experiment by depositing CuO in the presence of a racemic mixture of tartrate ions. There is no enantioselectivity in this case.

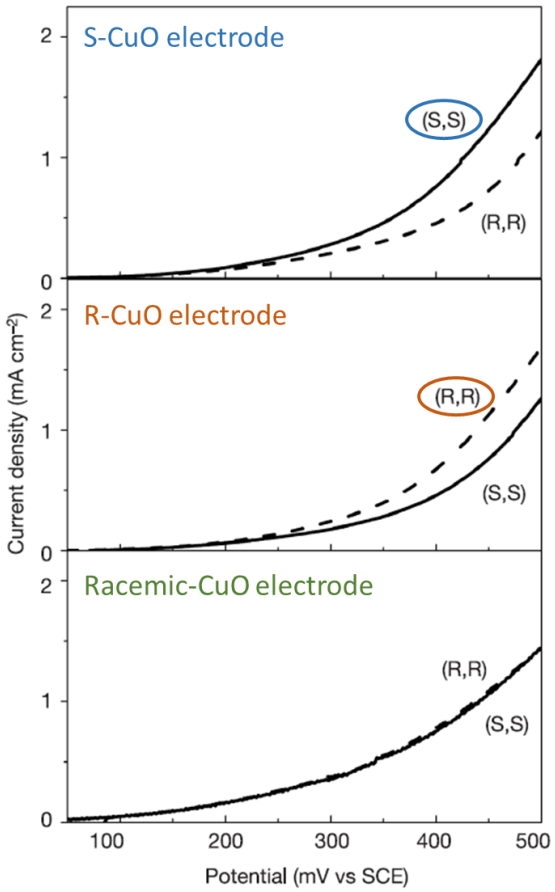

Figure 16: LSV recorded in 0.1 M NaOH, 5 mM (S,S)- or (R,R)-tartrate ions (respectively in solid and dashed lines) using either S-, R-, or racemic-tartrate for imprinting a CuO electrode. Sweep rate of 10 mV·s^{-1}. Adapted from [12]

I.3. Molecular impression

Molecular imprinted polymers (**MIP**) represent another approach for chiral recognition [13–15]. They have found applications in various fields such as sensing, drug delivery, purification

and separation. Their synthesis requires a template, functional monomers, cross-linkers, a polymerization initiator and a solvent.

Two main approaches can be followed to synthesize them: using covalent bonds between the templates and the functional monomers (Wulff approach [16]) or using non-covalent bonds (Mösbach approach [17]).

In the first case, the template molecules are bound to the appropriate monomers by covalent bonds (Scheme 1). During the polymerization, the polymers grow around the template molecule. This way of synthesis offers a great stability due to the high strength of the covalent bonds. Thus, this method leads to a more homogeneous distribution of the binding sites. The main disadvantage of this method is the limited variety of compounds that can establish a rapid and reversible covalent interaction between the templates and the monomers.

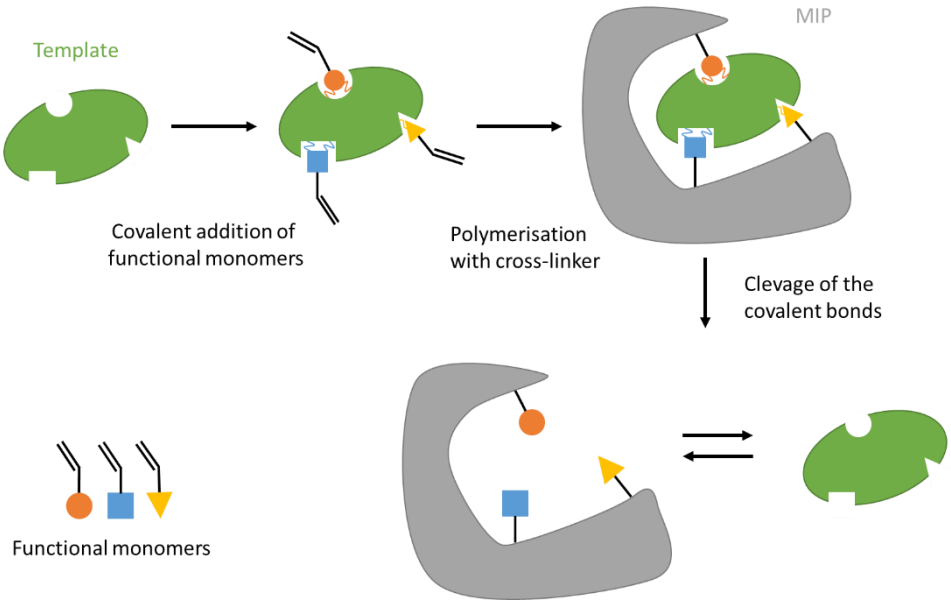

Scheme 1: Process of MIP synthesis based on covalent bonds.

Most of the MIPs are synthesized by using non-covalent bonds, such as hydrogen bonding, ionic interactions and Van der Waals forces, to form a template-monomer complex (Scheme 2). This method allows to design MIPs with a large number of target molecules. As the non-covalent bonds between the templates and the monomers are related to an equilibrium, it is necessary that the monomers are in excess in comparison with the templates. This excess leads to different configurations of the complex, thus, the MIPs will present a heterogeneous binding site distribution.

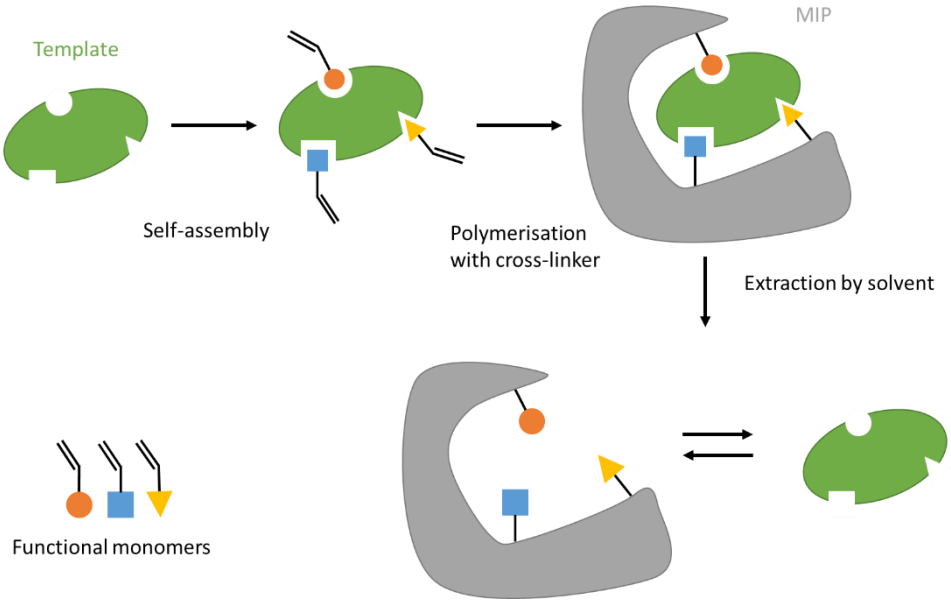

Scheme 2: Process of MIP synthesis by non-covalent bonds.

These materials present several advantages such as physical robustness, thermal and chemical stability, a versatile selectivity according to the used template and from a practical point of view, it is a low cost and straight forward technology.

However, there are still some challenges to be solved regarding the MIPs, such as their low compatibility with aqueous/polar media, their low binding capacity and slow mass transfer. In addition, in the second method, the polymers present heterogeneous binding sites related to their synthesis and during the formation of the polymer, the template molecules can leak out.

II. Mesoporous electrodes

The former systems show interesting properties with respect to enantiodifferentiation or the asymmetric synthesis. However, they suffer either from a low efficiency or from restricted operating conditions.

In the meantime, the field of mesoporous metals has been developed. Such materials show high surface area as well as regular and tunable pore sizes and are robust. Two main approaches have been developed to produce materials with controlled porosity: the hard-templating and soft-templating processes [18].

II.1. Hard templating

Hard-templating or nanocasting process requires the use of a solid structure. It can be either a porous film such as anodic aluminum oxide (**AAO**) or a colloidal crystal template as silica beads immobilized at the surface (Scheme 3). The first option can also lead to the formation of nanowires. It is important to pay attention to the stability of the mold and, afterwards, the synthesized materials. Another key point to take into account is the possibility to remove the template without destroying the replica material.

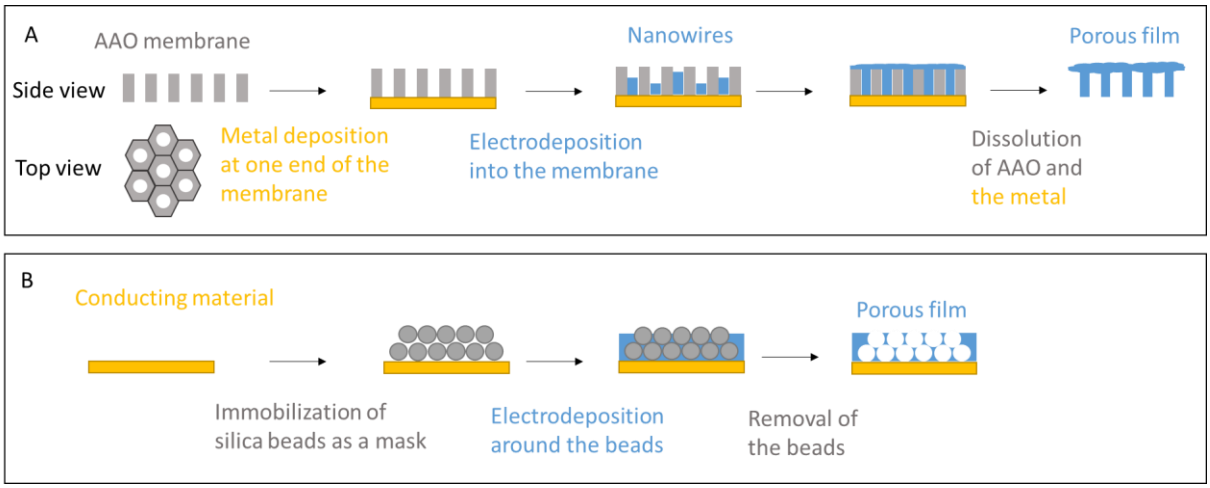

Scheme 3: Representation of the synthesis of porous films by hard-templating processes. A) Via AAO membranes; B) Through a template made out of silica beads

This approach gives access to highly ordered porous materials. However, once the preformed material is synthesized, it cannot be modified (or slightly, by etching for instance). Changing the different features (pore diameter, interpore distance, thickness, etc) requires the use of new templates. Thus, it is time-consuming and expensive.

II.2. Soft templating

Soft-templating is based on the use of surfactants which are amphiphilic molecules that can form a supramolecular self-assembly. These molecules consist of a hydrophobic and a hydrophilic part. These two antagonist properties give access to supramolecular arrangements which are studied by polarization optical microscopy and summarized in phase diagrams [19,20]. Some of these surfactants are qualified as “lyotropic”, which means that their arrangements

depend both on the temperature and the composition of the media. They can be used as a lyotropic liquid crystal (**LLC**) template. Polyoxyethylene surfactants are nonionic surfactants and can form LLC above a certain concentration in water. The high proportion of surfactant increases the viscosity of the media. Thus, mass transport limitations can be observed.

Soft-templating by LLC does not require the use of a porous material as template. Moreover, a single surfactant can lead to different arrangements (Scheme 4) and different sizes of pores by the addition of hydrophobic or hydrophilic compounds which can enlarge the surfactant structure. These possibilities are available for every surfactant which can form LLC phase.

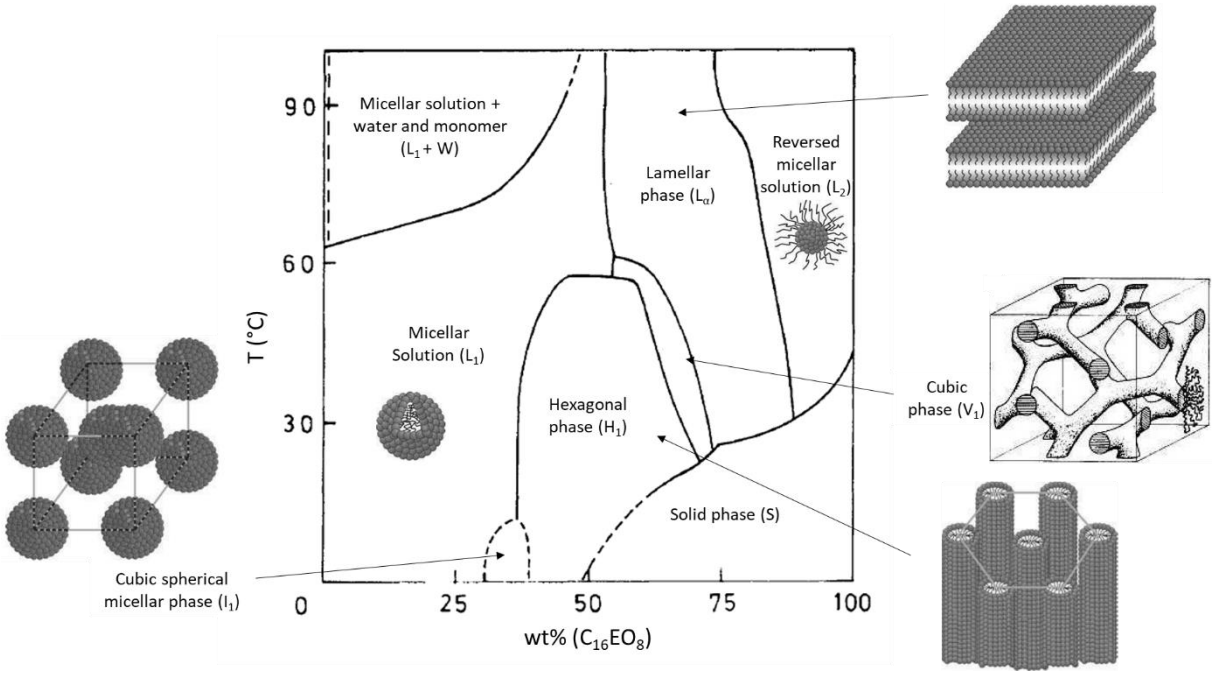

Scheme 4: Phase diagram obtained for the $C_{16}EO_8$ / water system showing the different arrangements: Micellar solution (L_1), cubic spherical micellar phase (I_1) hexagonal phase (H_1), cubic phase (V_1) and lamellar phase (L_α). Adapted from [19] and [21].

For the hexagonal arrangement, surfactant molecules are organized in columns. The hydrophobic part is turned towards the center of the column whereas the hydrophilic chain constitutes the external part. The aqueous solution is present all around the columnar structure.

Mesoporous platinum films have been the first example of metal obtained by ECD from a LLC phase [22]. An aqueous solution containing platinum ions ($PtCl_6^{2-}$) was mixed with a non-ionic surfactant ($C_{16}EO_8$) in specific proportions to form the hexagonal phase of the system (Figure 17).

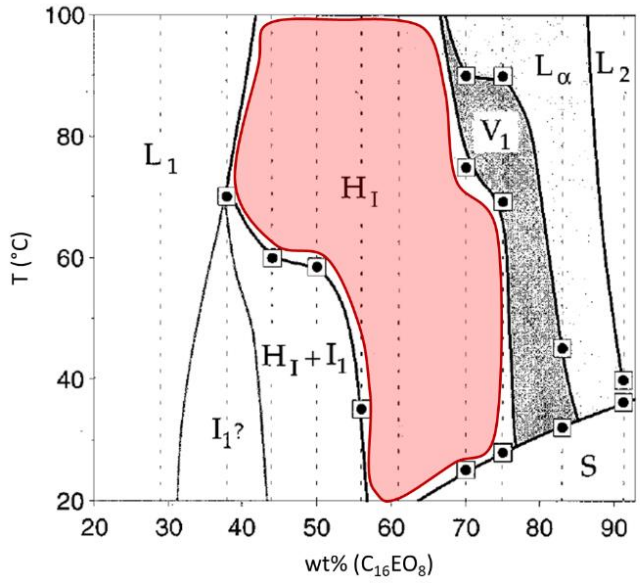

Figure 17: Pseudobinary phase diagram obtained for $C_{16}EO_8$ in water with 1.92 M H_2PtCl_6 with the hexagonal phase domain highlighted. Adapted from [23]

After the deposition, the template was removed by rinsing in water. Then, the electrodes were characterized by transmission electron microscopy (**TEM**) revealing the porous structure of the films. CV experiments in sulfuric acid were also performed to measure the electrochemically active surface area of the obtained materials (Figure 18). Under these conditions, CVs show the oxidation/reduction of the platinum surface and the adsorption/desorption of hydrogen. Both of these electrochemical reactions directly translate the active surface area of a platinum electrode [24,25]. The charges related to these reactions are higher for platinum deposited from LLC phase than platinum deposited without surfactant, which indicates an increase in surface area.

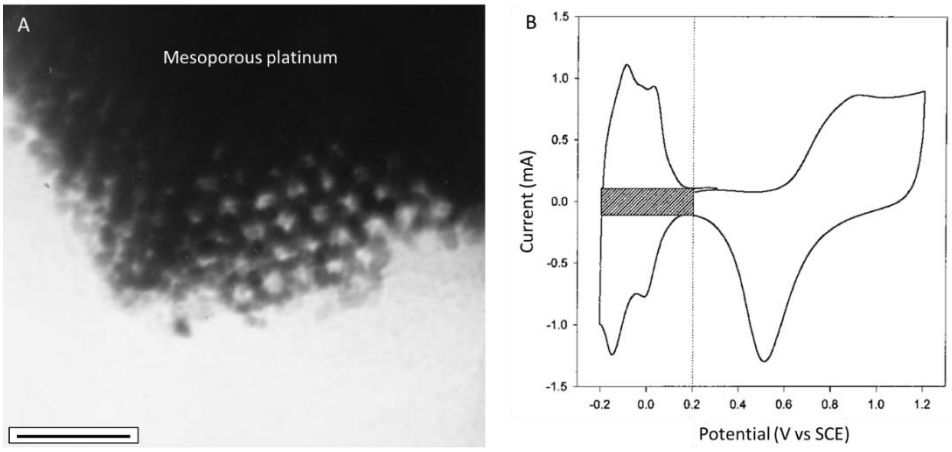

Figure 18: A) TEM image of mesoporous platinum (scale bar, 20 nm); B) CV of mesoporous platinum with the region of hydrogen adsorption/desorption highlighted. Adapted from [22]

This approach has been extended to other materials such as tin [26], cobalt [27] or rhodium [28]. These nanostructured metals present more interesting properties compared to the non-porous analogs thanks to the mesostructuration. Tin shows an interesting behavior when used in lithium ion batteries. Nanostructured cobalt has stronger magnetic features and rhodium was tested for the electrochemical reduction of nitrate. Mesoporous alloys have also been developed, such as platinum-ruthenium [29] or nickel-cobalt [30].

III. Chirally-imprinted mesoporous metal electrodes

Recently, chiral mesoporous metal electrodes (**CMME**) were developed. Inspired from MIPs, Wattanakit *et al.* combined the mesostructuration by a LLC phase and chiral imprinting [31]. Indeed, we saw previously that chiral surfaces suffer from a low efficiency regarding the enantiodifferentiation or the asymmetric synthesis, and that MIPs cannot be used with polar solvents. Thus, chiral imprinting of mesoporous metallic matrices should allow circumventing these limitations.

The proof-of-principle experiments have been performed with platinum due to its high stability. Platinum salt (H_2PtCl_6) in water, surfactant (Brij® 56) and the chiral molecule were mixed in well-defined proportions to obtain a LLC phase and more specifically, the hexagonal arrangement. In this configuration, as previously, the aqueous solution is present around the supramolecular arrangement of the surfactant. Therefore, the chiral molecules are adsorbed at the external part of the surfactant and platinum ions are also present around the columns. Thus, during the ECD, the reduced platinum reproduces the supramolecular structure of the surfactant and the chiral molecules, providing a mesoporous metal with chiral cavities. Subsequently, the template and the chiral molecules are removed by successive rinses in water (Scheme 5).

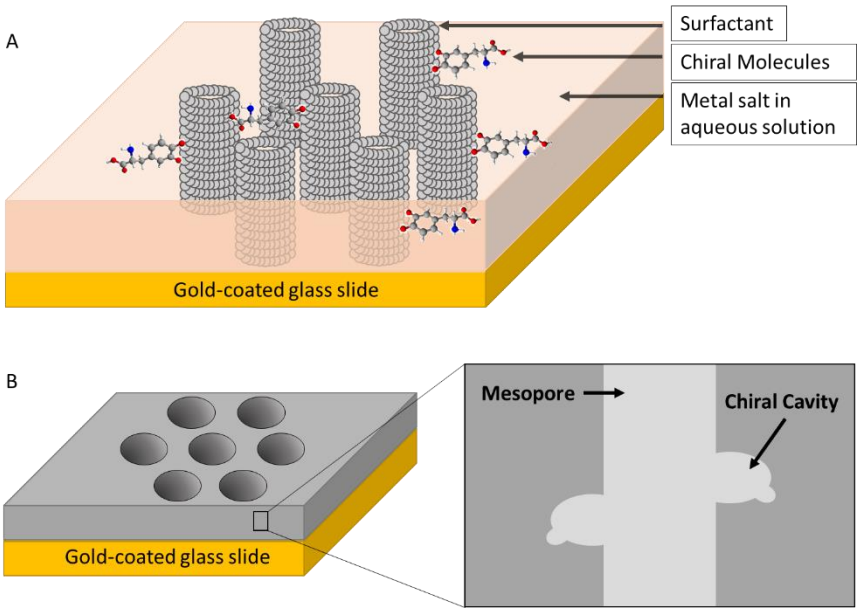

Scheme 5: Representation of the process to synthesize CMME. A) Before the electrodepositon, B) After electrodeposition and rinsing with solvent

Afterward, the electrodes were characterized by CV and TEM (Figure 19). The CV displays a very significant increase in current with the CMME compared to a flat electrode. The mesoporous structure has been observed by TEM. These results show that the addition of chiral molecules still allows the generation of a mesoporous structure.

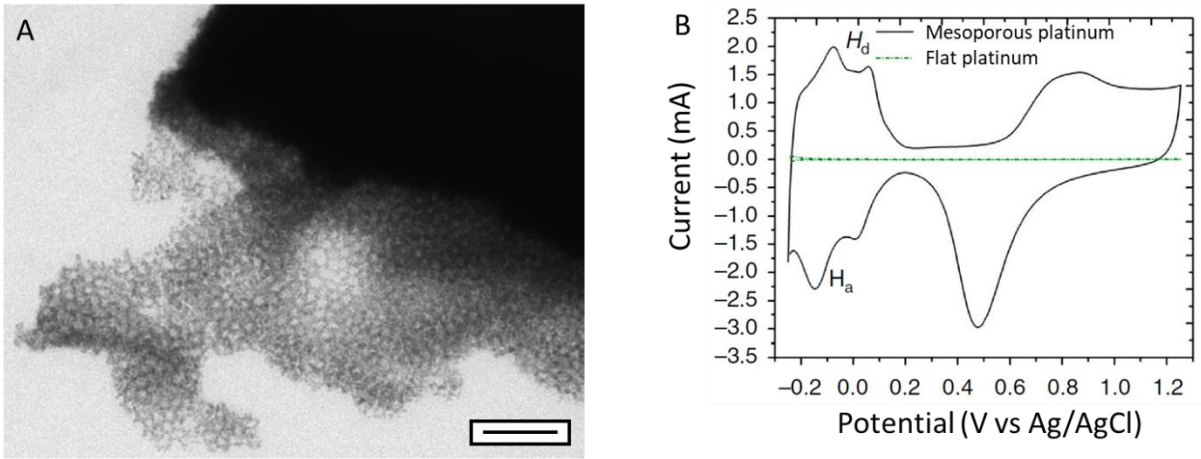

Figure 19: A) TEM image of a mesoporous platinum film (scale bar, 50 nm), B) CV in 0.5 M H_2SO_4 with mesoporous platinum (black line) and flat platinum (green dotted line). Adaped from [31]

Then, the chirality of the electrode was tested. Differential pulse voltammetry (**DPV**) experiments were carried out using the synthesized electrodes as WE. For the first work, L- and D-dihydroxy-3,4-phenylalanine (**DOPA**) were used as chiral templates. This molecule is electroactive in aqueous media and reacts at potentials where there is no interference with other

redox reactions, especially of platinum surface. This allows studying the reactivity (and more specifically its oxidation) of DOPA without modification of the platinum surface. Two types of electrodes were used, one imprinted by L-DOPA, another imprinted by D-DOPA. Two solutions containing the respective enantiomers at the same concentration with the same supporting electrolyte were tested. The electrodes imprinted with L-DOPA show a higher current for the oxidation of L-DOPA compared to D-DOPA molecules. The reverse trend was observed when using D-DOPA imprinted electrodes (Figure 20). These results demonstrate the possibility to distinguish two enantiomers by electrochemistry using CMME. However, after cycling in sulfuric acid in a wider potential window, no selectivity remained. It is assumed that the successive oxidations and reductions as well as the adsorption and desorption of protons rearrange the surface, and thus erase the chirality of the electrodes.

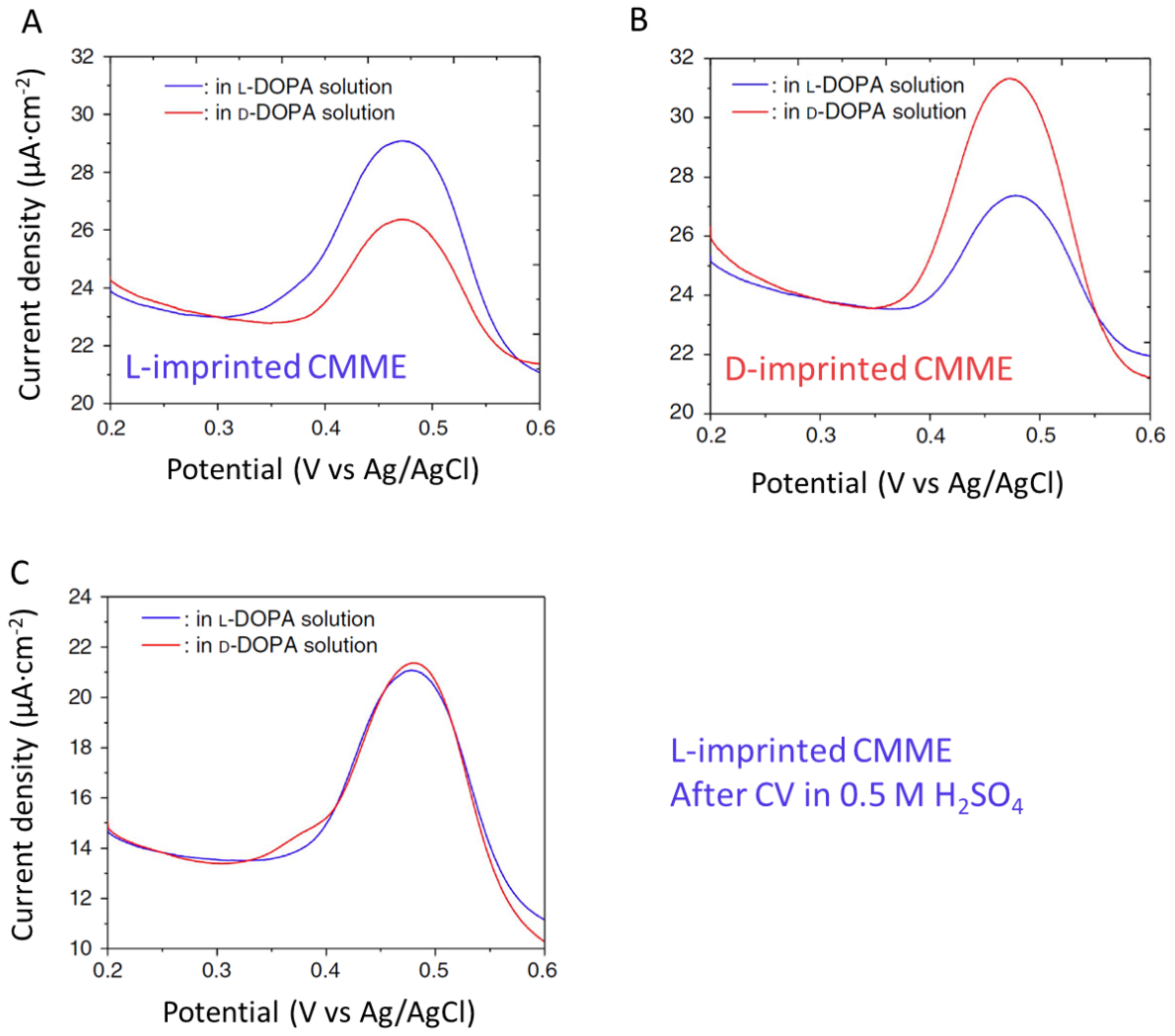

Figure 20: DPV in 4 mM L-DOPA (blue) and D-DOPA (red) solutions, with a CMME imprinted with A) L-DOPA, B) D-DOPA, C) L-DOPA after CV in 0.5 M H_2SO_4. Adapted from [31]

In a follow-up work, they studied the possibility to use these electrodes to perform asymmetric synthesis to obtain mandelic acid (**MA**) from phenylglyoxylic acid (**PGA**) [32]. The electrodes were imprinted with enantiomerically pure MA and used to reduce enantioselectively PGA into MA. The resulting mixture was analyzed by high-performance liquid chromatography (**HPLC**). The experiment reveals a modest enantiomeric excess (**ee**) but demonstrate encouraging results for asymmetric synthesis.

In a further extension of the concept, pulsed chronoamperometry (**CA**) was used to convert acetophenone (**AE**) into phenylethanol (**PE**) [33]. The relaxation time between the potential pulses improves the diffusion of molecule into and out of the CMME. An optimization of the experimental parameters allowed reaching an enhancement of the ee to up to 90 % for the shortest pulses (Figure 21).

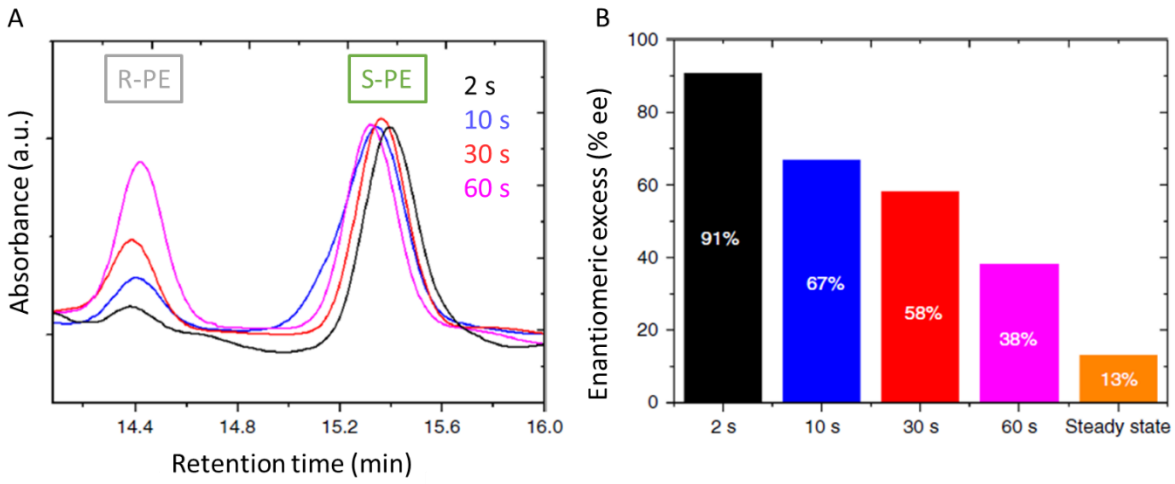

Figure 21: A) HPLC chromatograms of solutions after electrosynthesis using S-PE CMME with different pulse times (60 s, 30 s, 10 s, 2 s, in pink, red, blue and black, respectively). B) Comparison of the ee obtained depending on the pulse time. Adapted from [33]

Very recently, the stability of the mesoporous matrix could be improved by depositing a Pt-Ir alloy which showed good enantiodifferentiation even after several experiments (Figure 22) [34]. Regarding the asymmetric synthesis, these electrodes give access to an enantiomeric excess between 49 % (with constant CA) and 95 % (with pulsed CA) which represent a huge improvement compared to the results obtained with platinum only. Moreover, the efficiency decreases only very slightly even after prolonged use compared to CMMEs made out of pure platinum (Figure 23).

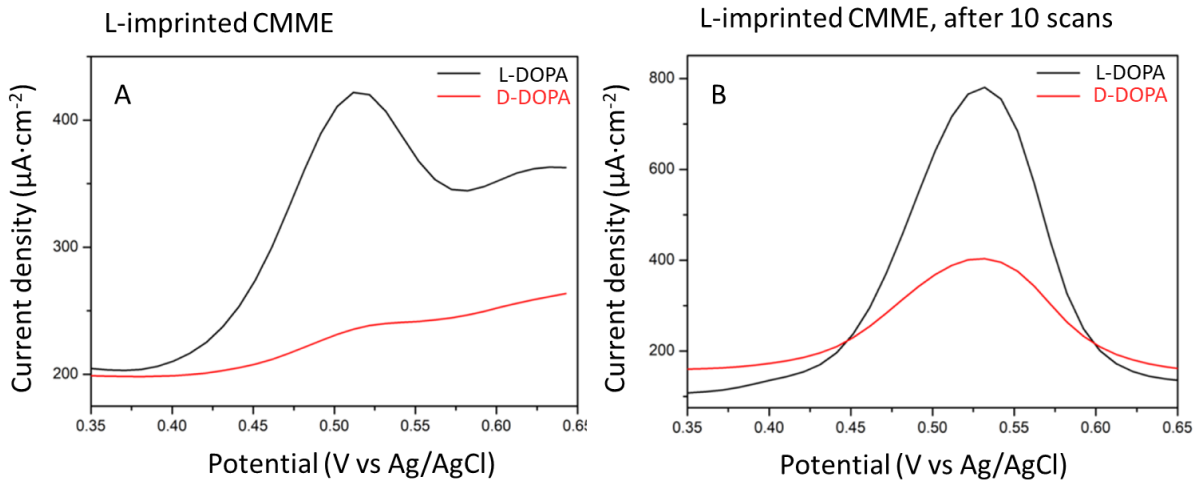

Figure 22: DPV in 4 mM L-DOPA (black) and D-DOPA (red) solutions, A) with a CMME imprinted with L-DOPA, B) After 10 scans in 0.5 M H_2SO_4. Adapted from [34]

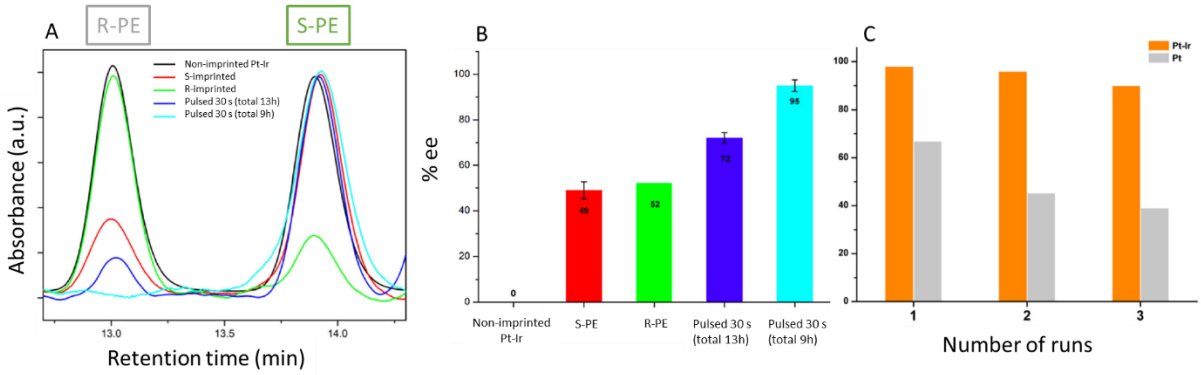

Figure 23: A) HPLC chromatograms of solutions after electrosynthesis of PE by constant (black, red and green lines) or pulsed (dark blue and light blue lines) CA with non-imprinted electrode (black), R-imprinted (green), S-imprinted (red, dark blue and light blue). B) comparison of the ee obtained for each synthesis. C) comparison of the ee obtained after 1, 2 and 3 runs with S-imprinted Pt-Ir (orange) and Pt (gray) electrodes. Adapted from [34]

Nevertheless, despite these promising results, these electrodes were made of platinum which is an expensive metal. Therefore, it is interesting to adapt the same concept to cheaper metals. Mesoporous nickel films were successfully imprinted with PE [35], using an analog procedure, and showed enantioselectivity. The ee evolved from 20 % for constant CA to 80% with pulsed CA (Figure 24).

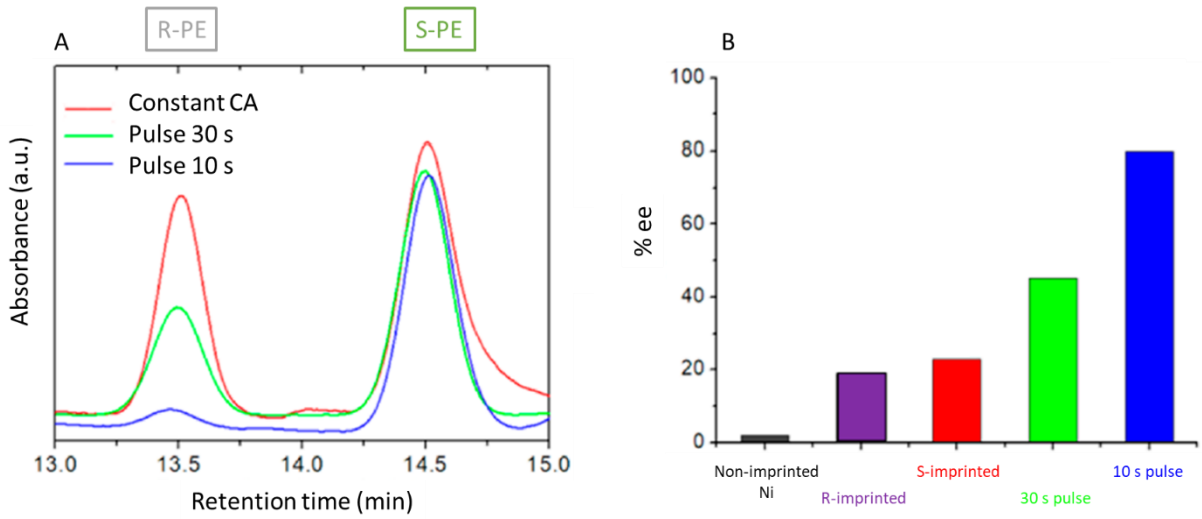

Figure 24: A) HPLC chromatograms of solutions after electrosynthesis with different pulse times using S-PE CMME made of nickel. B) Comparison of the ee obtained with R- and S- imprinted CMME and with S-PE electrodes with pulsed electroconversion. Adapted from [35]

In summary, two types of materials were tested with respect to the possibility to imprint chiral information. The first is based on the use of platinum. This provides a rather robust and stable material, especially when alloyed with iridium, but it is quite expensive. The second is based on nickel, which has the advantages of being cheaper than platinum, but suffers from low stability. Moreover, these materials show a rather modest conversion yield of prochiral molecules into enantiomers.

In the first part of this thesis, we try to deal with the latter issue by using another catalytic metal. Indeed, so far, hydrogenation reactions were performed and one of the best catalyst for this family of reactions is palladium [36,37]. Even if this metal is among the most expensive ones, we wanted to transpose this concept to palladium in order to improve the conversion yield of hydrogenation reaction. The results of the experiments performed in this context are described in the next chapter.

IV. References

[1] R. Raval, *Chem. Soc. Rev.* **2009**, *38*, 707.

[2] S. M. Barlow, R. Raval, *Surf. Sci. Rep.* **2003**, *50*, 201.

[3] V. Humblot, R. Raval, *Appl. Surf. Sci.* **2005**, *241*, 150.

[4] M. Ortega Lorenzo, C. J. Baddeley, C. Muryn, R. Raval, *Nature* **2000**, *404*, 376.

[5] H.-U. Blaser, M. Studer, *Acc. Chem. Res.* **2007**, *40*, 1348.

[6] T. Mallat, E. Orglmeister, A. Baiker, *Chem. Rev.* **2007**, *107*, 4863.

[7] V. Humblot, S. Haq, C. Muryn, W. A. Hofer, R. Raval, *J. Am. Chem. Soc.* **2002**, *124*, 503.

[8] M. A. Keane, *Langmuir* **1997**, *13*, 41.

[9] D. S. Sholl, A. Asthagiri, T. D. Power, *J. Phys. Chem. B* **2001**, *105*, 4771.

[10] G. A. Attard, A. Ahmadi, J. Feliu, A. Rodes, E. Herrero, S. Blais, G. Jerkiewicz, *J. Phys. Chem. B* **1999**, *103*, 1381.

[11] A. Ahmadi, G. Attard, J. Feliu, A. Rodes, *Langmuir* **1999**, *15*, 2420.

[12] J. A. Switzer, H. M. Kothari, P. Poizot, S. Nakanishi, E. W. Bohannan, *Nature* **2003**, *425*, 490.

[13] M. Kempe, K. Mosbach, *J. Chromatogr. A* **1995**, *694*, 3.

[14] S. A. Piletsky, K. Karim, E. V. Piletska, A. P. F. Turner, C. J. Day, K. W. Freebairn, C. Legge, *The Analyst* **2001**, *126*, 1826.

[15] N. M. Maier, W. Lindner, *Anal. Bioanal. Chem.* **2007**, *389*, 377.

[16] G. Wulff, *Angew. Chem. Int. Ed. Engl.* **1995**, *34*, 1812.

[17] K. Mosbach, *Trends Biochem. Sci.* **1994**, *19*, 9.

[18] Y. Yamauchi, K. Kuroda, *Chem. – Asian J.* **2008**, *3*, 664.

[19] D. J. Mitchell, G. J. T. Tiddy, L. Waring, T. Bostock, M. P. McDonald, *J. Chem. Soc. Faraday Trans. 1 Phys. Chem. Condens. Phases* **1983**, *79*, 975.

[20] G. Wanka, H. Hoffmann, W. Ulbricht, *Macromolecules* **1994**, *27*, 4145.

[21] A. M. Figueiredo Neto, S. R. A. Salinas, *The physics of lyotropic liquid crystals: phase transitions and structural properties*, Oxford University Press, New York, **2005**.

[22] G. S. Attard, *Science* **1997**, *278*, 838.

[23] G. S. Attard, P. N. Bartlett, N. R. B. Coleman, J. M. Elliott, J. R. Owen, *Langmuir* **1998**, *14*, 7340.

[24] T. Biegler, D. A. J. Rand, R. Woods, *J Electroanal Chem* **1971**, 9.

[25] J. M. Doña Rodríguez, J. A. Herrera Melián, J. Pérez Peña, *J. Chem. Educ.* **2000**, *77*, 1195.

[26] A. H. Whitehead, J. M. Elliott, J. R. Owen, G. S. Attard, *Chem. Commun.* **1999**, 331.

[27] P. N. Bartlett, P. N. Birkin, M. A. Ghanem, P. de Groot, M. Sawicki, *J. Electrochem. Soc.* **2001**, *148*, C119.

[28] P. N. Bartlett, J. Marwan, *Microporous Mesoporous Mater.* **2003**, *62*, 73.

[29] G. S. Attard, S. A. A. Leclerc, S. Maniguet, A. E. Russell, I. Nandhakumar, B. R. Gollas, P. N. Bartlett, *Microporous Mesoporous Mater.* **2001**, *44–45*, 159.

[30] Y. Yamauchi, T. Yokoshima, T. Momma, T. Osaka, K. Kuroda, *J Mater Chem* **2004**, *14*, 2935.

[31] C. Wattanakit, Y. B. S. Côme, V. Lapeyre, P. A. Bopp, M. Heim, S. Yadnum, S. Nokbin, C. Warakulwit, J. Limtrakul, A. Kuhn, *Nat. Commun.* **2014**, *5*, 3325.

[32] T. Yutthalekha, C. Wattanakit, V. Lapeyre, S. Nokbin, C. Warakulwit, J. Limtrakul, A. Kuhn, *Nat. Commun.* **2016**, *7*, 12678.

[33] C. Wattanakit, T. Yutthalekha, S. Asssavapanumat, V. Lapeyre, A. Kuhn, *Nat. Commun.* **2017**, *8*, 2087.

[34] S. Butcha, S. Assavapanumat, S. Ittisanronnachai, V. Lapeyre, C. Wattanakit, A. Kuhn, *Nat. Commun.* **2021**, *12*, 1314.

[35] S. Assavapanumat, M. Ketkaew, A. Kuhn, C. Wattanakit, *J. Am. Chem. Soc.* **2019**, *141*, 18870.

[36] A. Klinkova, P. De Luna, C.-T. Dinh, O. Voznyy, E. M. Larin, E. Kumacheva, E. H. Sargent, *ACS Catal.* **2016**, *6*, 8115.

[37] M. Shao, Q. Chang, J.-P. Dodelet, R. Chenitz, *Chem. Rev.* **2016**, *116*, 3594.

[38] P. N. Bartlett, B. Gollas, S. Guerin, J. Marwan, *Phys. Chem. Chem. Phys.* **2002**, *4*, 3835.

Chapter II – Macroscopic palladium deposition and chirality

Following on from previous work performed on chirally-imprinted mesoporous metal electrodes (**CMME**) made of platinum [1], platinum-iridium alloy [2] and nickel [3], Palladium was chosen to address the problematic of a low yield during asymmetric synthesis.

In this chapter, first, we will study the reactivity of a palladium electrode regarding the dihydroxy-3,4-phenylalanine (**DOPA**) enantiomers oxidation. Afterwards, electrochemical deposition (**ECD**) from liquid lyotropic crystal (**LLC**) phase will be performed at the macroscopic scale in order to obtain mesoporous palladium following the procedure of the literature which use microscopic substrates [5].

I. Reactivity of a flat palladium electrode

In this section, we used a commercial flat palladium electrode as a working electrode (**WE**) in a three-electrode setup with an Ag/AgCl (3 M NaCl) electrode and a platinum mesh as a reference electrode and a counter electrode, respectively. All the following potentials will be given versus the Ag/AgCl reference. Prior to the electrochemical measurements of the DOPA system, it is necessary to find an appropriate supporting electrolyte (**SE**). As the experiments with platinum, platinum-iridium and nickel electrodes were performed in 50 mM hydrochloric acid, this electrolyte was tested.

A cyclic voltammetry (**CV**) in such an electrolyte shows a huge increase of the oxidative current starting from 0.3 V (Figure 25). Indeed, it has been shown that the presence of chloride ions in acid solution increases the rate of the anodic dissolution of palladium [4]. It is assumed that, in addition to the formation of an oxide layer, the palladium reacts with the chloride to form $PdCl_2$ or $[PdCl_4]^{2-}$ (Figure 26). This behavior would disturb the measurement of the oxidation of DOPA molecules and damage the electrode. Therefore, a chloride-free electrolyte was tested. In 50 mM sulfuric acid, the current density remains at a low level when going towards anodic potentials. A small increase can be noticed from 0.6 V which correspond to the oxidation of palladium. Comparing these two results, sulfuric acid appears to be more appropriate as a SE to study DOPA oxidation than hydrochloric acid when a palladium electrode is used as a WE.

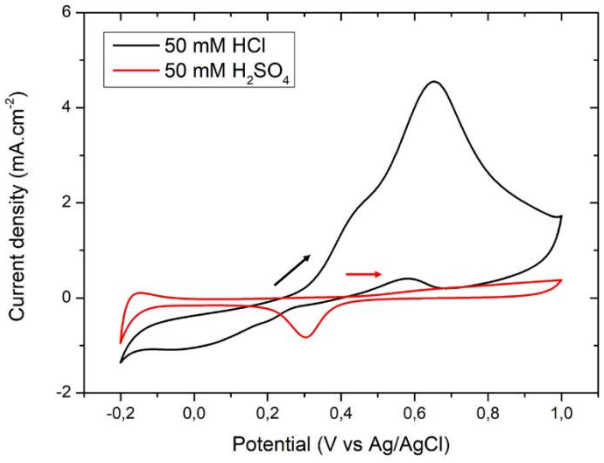

Figure 25: CVs performed in 50 mM HCl (black line) and 50 mM H_2SO_4 (red line). WE: Pd disc (A = 2 mm²), scan rate: 100 mV·s^{-1}

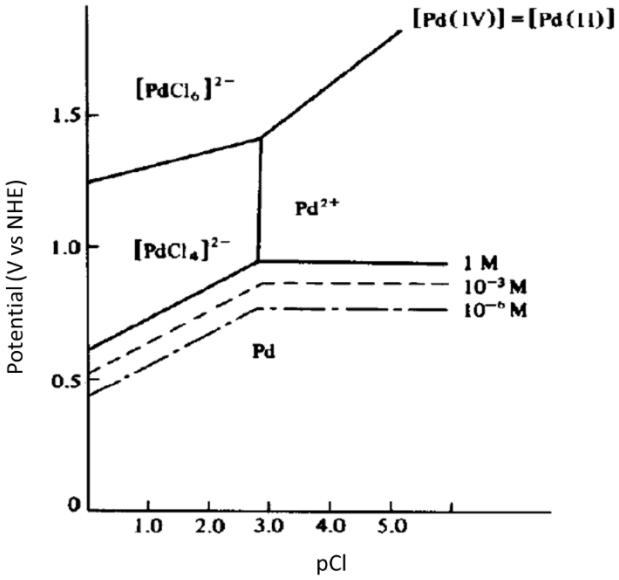

Figure 26: Potential-pCl diagram for palladium at 25 °C. Adapted from [4]

Afterwards, the electrochemical behavior of DOPA molecules at the palladium electrode was studied by CV and differential pulse voltammetry (**DPV**). CVs were performed with each enantiomer and the racemic solution (Figure 27 A). The experiments were started at the open-circuit potential (**OCP**), around 0.0 V for each solution, scanning toward the anodic potential. Each CV shows the oxidation of DOPA molecules around 0.6 V and reaches a stable current density from 0.8 to 1.0 V corresponding to the palladium oxidation. At the reverse scan, a reduction peak is present at 0.3 V which was not present at the forward scan. Thus, this peak is related to species oxidized during the forward scan. The reaction can be related either to the reduction of DOPA, to the reduction of palladium oxide or to the overlapping of both reactions. It has not been investigated in this work, but the distinction can be done by varying the DOPA concentration.

Afterwards, DPVs were performed with L- and D-DOPA solutions. The DPVs present the advantage of being more sensitive than CV and to remove the capacitive current from the measurement. These experiments show the oxidation of DOPA around 0.55 V. Due to the DPV features, it is normal to observe this shift in potential.

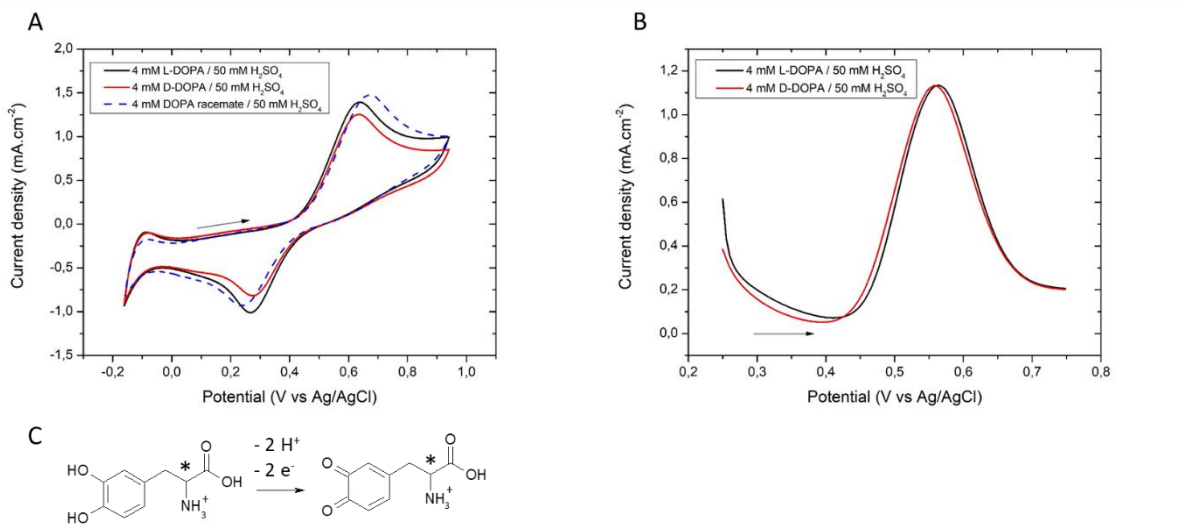

Figure 27: A) CV of 4 mM DOPA in 50 mM H_2SO_4: L-DOPA (in black line), D-DOPA (in red line), racemate (in blue dotted line). WE: Pd disc (A = 2 mm²), scan rate: 100 mV·s^{-1}

B) DPV of 4 mM DOPA in 50 mM H_2SO_4. L-DOPA (in black line), D-DOPA (in red line). WE: Pd disc (A = 2 mm²), scan rate: 50 mV·s^{-1}

C) Oxidation of DOPA molecules in acidic media

As there is no chiral induction in the media, the signals of current density overlay for each measurement (CV and DPV). As expected, there is no enantiodifferentiation.

The oxidation of DOPA molecules occurs around the oxidation of palladium metal. This feature is not suitable for our system, since the oxidation of the palladium will modify the surface and hence, modify the reactivity and the selectivity of the CMME. The DPV also shows that the current density after the oxidation peak does not reach 0 mA·cm^{-2} which means that there is still a faradaic reaction that occurs at the surface (corresponding to the palladium oxidation).

Prior to thinking about changing the chiral molecule, we investigated the possibility of DOPA adsorption at the palladium surface. Indeed, if DOPA can adsorb spontaneously at the surface, the selectivity of the electrode can be measured by the measured oxidation charge which is related to the amount of adsorbed molecules.

For this purpose, a first DPV was recorded in SE only, then the electrode was immersed in DOPA solution, rinsed in water, then a new DPV in SE was recorded (Figure 28).

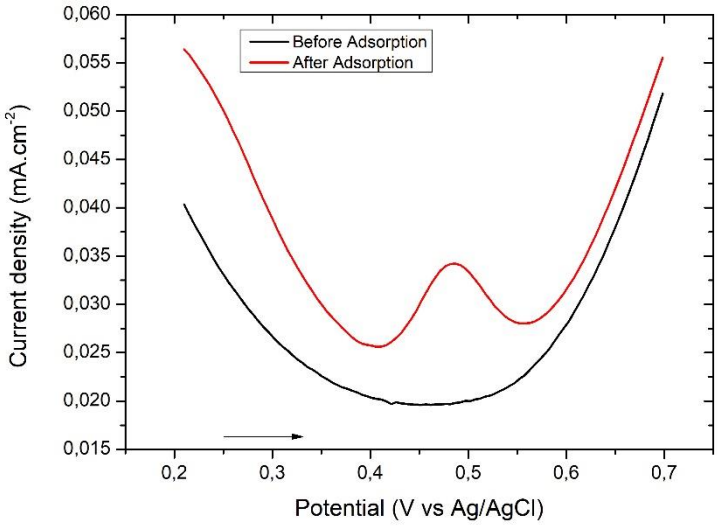

Figure 28: DPV in SE before (black line) and after (red line) DOPA adsorption. Immersion in DOPA solution: 4 mM DOPA in 50 mM H_2SO_4 for 30 min, then 10 min in water.

The DPV before immersion is considered as a blank measurement. The DPV after immersion shows an oxidation signal which is not present on the first record. This result shows that DOPA molecules were adsorbed at the surface. Moreover, we can notice a lower potential of oxidation (comparing to the DPV in DOPA solution) corresponding to an easier oxidation, which is in good agreement with an adsorption process.

Different parameters were varied in order to modulate this phenomenon, namely: the concentration of DOPA, the immersion time in DOPA solution, the immersion time in the rinsing solution and the nature of the rinsing solution (water, ethanol and 50 mM KOH). The results show that a short rinsing time (10 min) in water after a long immersion time (30 min) in the solution at the highest DOPA concentration (4 mM) provides the highest charge related to the DOPA oxidation, thus a larger amount of adsorbed molecules.

Finally, we show that sulfuric acid is more appropriate than hydrochloric acid as a SE when the electrode material is palladium. The study of the DOPA redox system on palladium shows that the oxidation potential of DOPA is close to the potential of oxidation of palladium, which is a drawback for the chiral recognition step. However, the DOPA molecules can be adsorbed at the surface of the palladium electrode quite easily which allow us to circumvent this issue. Afterward, ECD of palladium from LLC will be discussed. Mesoporous palladium has already been obtained in the literature [5–8], however only ultramicroelectrodes (**UME**) were

used as WE. As one of the goals of the work is to synthesize chiral molecules with CMME, we tried to scale up the process to macroscopic electrodes.

II. Deposition of palladium from LLC

II.1. Phase diagram and electrochemical analysis of the electrolyte

Prior to performing ECD, it is essential to choose the right composition of the electrolyte to form a hexagonal supramolecular arrangement, giving access to mesoporous structuration of the material. Therefore, it is necessary to analyze the phase diagram of the lyotropic mixture (Figure 29). The phase diagram shows the different domains of arrangement of the surfactant in the presence of an aqueous solution of palladium at 1.40 mol·L^{-1}. The hexagonal domain of this system is wide thus, slight changes in the electrolyte composition (as water evaporation, for instance) should not represent a problem regarding the mesostructuration.

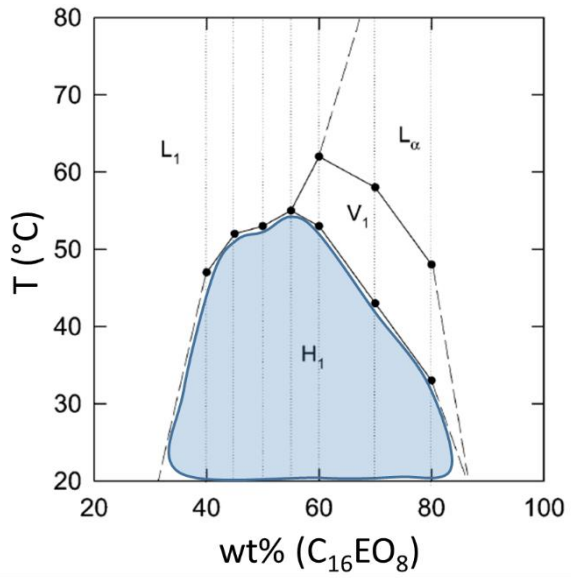

Figure 29: Pseudobinary phase diagram obtained for $C_{16}EO_8$ in water with 1.40 M $(NH_4)_2PdCl_4$ with the hexagonal phase domain highlighted. Adapted from [5]

We reproduced the composition of the electrolyte from the work of Bartlett's group [5] without the addition of heptane, which is added only to widen the diameter of the supramolecular columns: 12 wt.% $(NH_4)_2PdCl_4$, 40 wt.% H_2O, 48 wt.% surfactant. This composition presents a hexagonal arrangement until 52 °C. It is important to note that this

mixture is highly viscous. Then, a CV has been recorded with this electrolyte to study the electrochemical behavior of such system (Figure 30).

The first scan (black line) shows an increasing reduction current starting from 0.2 V (C_1) followed by a second step around -0.1 V (C_2). The reverse scan crosses the forward scan indicating a surface change while scanning. The peak C_1 occurs at less and less negative potential with the number of scans, meaning that the reduction reaction becomes easier at each scan. The peak C_2 is still not well defined but is more pronounced in the last scan. From the second scan, an anodic peak is observed (A_2) and the current related to this reaction increases from the second to the fifth scan.

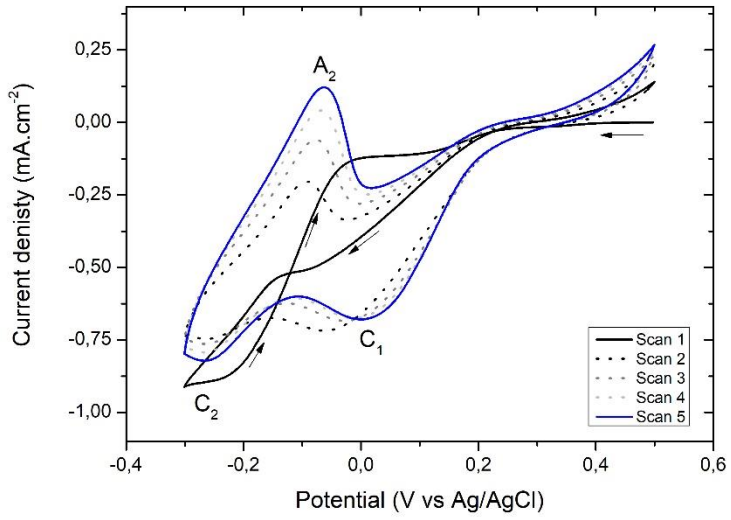

Figure 30: 5 successive scans with the electrolyte used for the electrodeposition: 12 wt.% $(NH_4)_2PdCl_4$, 40 wt.% H_2O, 48 wt.% Brij® C10. WE: Au-coated glass slide, A = 0.25 cm^2, scan rate: 20 $mV{\cdot}s^{-1}$

From these observations, the peak C_1 can be associated to the palladium deposition. Indeed, the nucleation loop at the first scan is indicating a surface change between the forward and the reverse scan, which is in favor of the palladium deposition. Moreover, the following scans show an easier reaction after the modification during the first scan, meaning that palladium had been deposited since there is higher affinity between palladium and palladium than between gold and palladium.

The second reduction peak, C_2, can be related to proton reduction. In the first scan, the reverse part shows a higher current compared to the forward scan meaning a higher activity for

this reaction with the modified surface. It is well-known that palladium is a good catalyst for reduction reactions and a good material for hydrogen formation.

The anodic peak appears only from the second scan. Thus, it is an oxidation induced by a former modification and cannot be related to the reduction at C_1 since the oxidation potential of A_2 (-0.1 V) is lower than the reduction potential of C_1 (0 V). From these elements, this peak should be the oxidation of hydrogen which was reduced on palladium during the forward scan.

$$PdCl_4^{2-} + 2e^- \rightarrow Pd^0 + 4Cl^- \qquad \text{Eq. C1}$$

$$H^+ + e^- \rightarrow H_{ads} \qquad \text{Eq. C2}$$

$$H_{ads} \rightarrow H^+ + e^- \qquad \text{Eq. A2}$$

In our case, we are interested by the reduction of palladium (C_1). An appropriate potential of deposition should be between 0.2 V and -0.1 V. The higher limit is given by the necessity to ensure a sufficient overpotential to trigger the palladium deposition. The lower limit is imposed by the second reduction, in order to do not induce undesired electrochemical side reactions.

II.2. Electrochemical deposition of palladium

From the voltammogram, we saw that the deposition starts to be significant at 0.2 V. In order to select the most appropriate potential, depositions were performed at different potentials and analyzed by scanning electron microscope (**SEM**, Figure 31). The lowest tested potential was 0.1 V, then 0.15 V, 0.2 V and finally 0.25 V. The SEM images give morphological information about the deposits. Mesoporous palladium is expected to present a smooth surface, otherwise, the non-imprinted surface could be too high compared to the chiral surface which is inside the pores. The electrodes deposited at different potentials show heterogeneous and rough surfaces. For the deposit obtained at 0.1 V, it can even be seen that there are clusters which present an additional rough surface. The deposit at 0.15 V displays also an inhomogeneous surface, as well as the deposit obtained at 0.2 V. These observations are in favor of a lack of palladium during the electrodeposition. Thus, deposits have been performed at 0.25 V. At this potential, it is expected to observe a slow deposition as the overpotential is small. This rate of deposition should allow the palladium precursor to reach homogeneously the surface of the

electrode by diffusion during the ECD. As expected, the deposition leads to a smoother surface compared to the electrodes obtained at higher overpotential. However, the deposit still present irregularities. Moreover, the electrodeposition was slow (around 8 hours to reach 2 $C \cdot cm^{-2}$) and the electrolyte might dry up, leading to a change of the supramolecular arrangement.

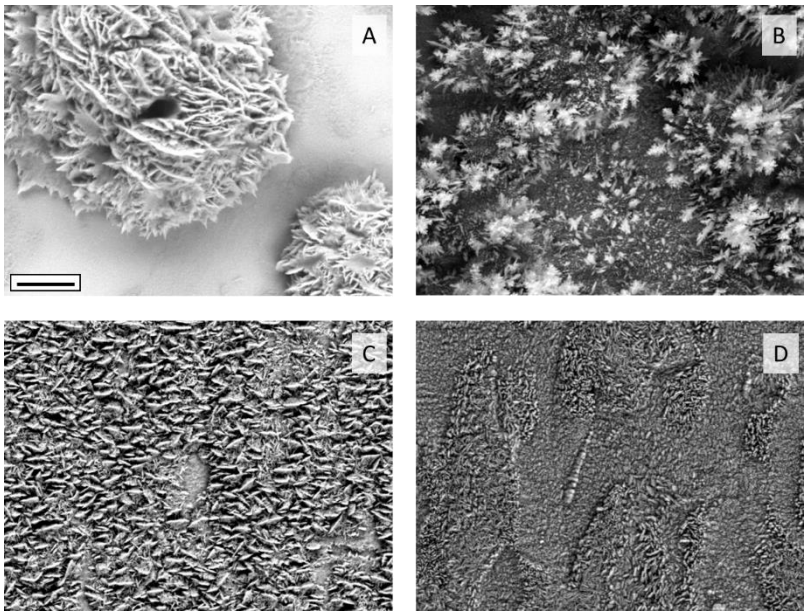

Figure 31: SEM images of palladium deposited from a LLC phase at A) 0.1 V, B) 0.15 V, C) 0.2 V, D) 0.25 V for 2 $C \cdot cm^{-2}$. WE: Au-coated glass slide, A=0.25 cm^2. Scale bar, 5 µm LLC phase : 12 wt.% $(NH_4)_2PdCl_4$, 40 wt.% H_2O, 48 wt.% Brij® C10

From these results, a potential of 0.2 V was chosen. Afterward, the influence of other parameters such as the temperature during the deposition, the influence of the surfactant, the substrates and finally the injected charge for the deposition was studied.

An increase of the temperature reduces the viscosity of the electrolyte and thus increase the diffusion rate of the palladium ions. A better diffusion of the metallic ions should improve the homogeneity of the electrolyte and thus, the morphology of the deposit.

Four temperatures have been tested for the ECD, room temperature (**RT**, *ca.* 25 °C), 40 °C, 60 °C and 80 °C. The obtained electrodes were observed by SEM (Figure 32). At RT, a mix of needle and lamellar morphology is observed. An increase to 40 °C allows to reduce the inhomogeneity, showing a major needle-shaped morphology. At 60 °C, we can observe oblong shapes more curved than the needles observed at 40 °C. The deposits at 80 °C show a complete different morphology with circular grains. The latter result is not surprising since at 80 °C, the surfactant presents a micellar arrangement according to its phase diagram (Figure 29). The

morphology observed at 60 °C can be seen as the transition between the hexagonal and the micellar arrangement of the surfactant.

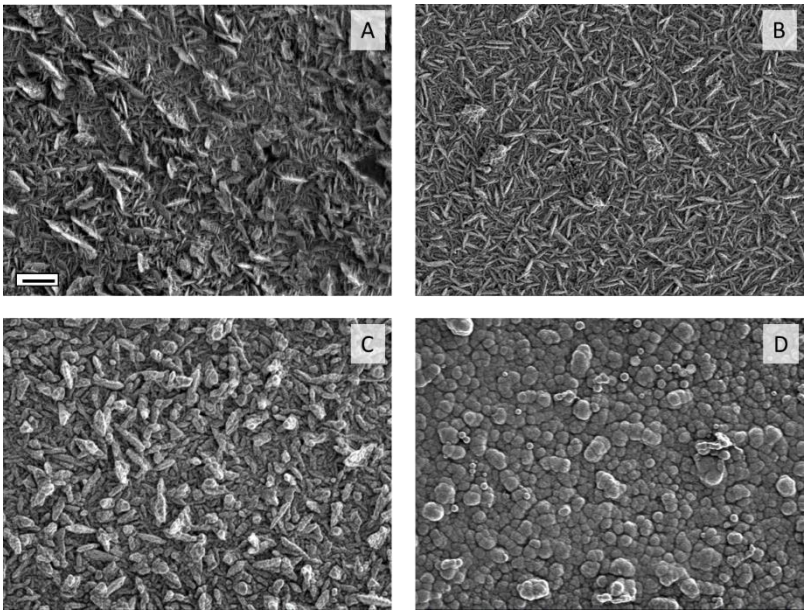

Figure 32: SEM images of palladium deposited from a LLC phase at A) RT, B) 40 °C, C) 60 °C, D) 80 °C for 2 C·cm^{-2} at 0.2 V vs Ag/AgCl. WE: Au-coated glass slide, A=0.25 cm^2. Scale bar, 1 µm
LLC phase : 12 wt.% $(NH_4)_2PdCl_4$, 40 wt.% H_2O, 48 wt.% Brij® C10

Finally, increasing the temperature to 40 °C allows a better homogeneity of the deposit. However, the obtained surface is still highly rough which is not satisfying.

Afterward, the impact of the surfactant has been studied. The interaction between the hexagonal phase and the substrates might be involved in the ECD process. Three surfactants have been tested: Brij® 56, Brij® C10 (which is a more recent formulation of Brij® 56) and $C_{16}EO_8$. All these surfactants are principally based in the same ingredient: Brij® is a mixture of molecules of different size. There is a distribution around one molecular length meaning that all the molecules do not have the same length. This is not the case with $C_{16}EO_8$, which contains only molecules of one length. The pure surfactant is expected to provide more homogeneous surface compared to the Brij®.

The morphology of the obtained electrodes has been analyzed by SEM (Figure 33). The surface obtained with Brij® 56 is highly heterogeneous. There are some clusters composed of needle-shaped grains above a film of needle-shaped particles. Moreover, the electrode was not fully covered, gold was still observable even by naked eyes. The use of Brij® C10 improves the coverage of the substrate, no gold could be observed. However, the morphology is still

irregular. Finally, the use of $C_{16}EO_8$ provides a good coverage with a homogeneous morphology. However, the surface roughness is still high.

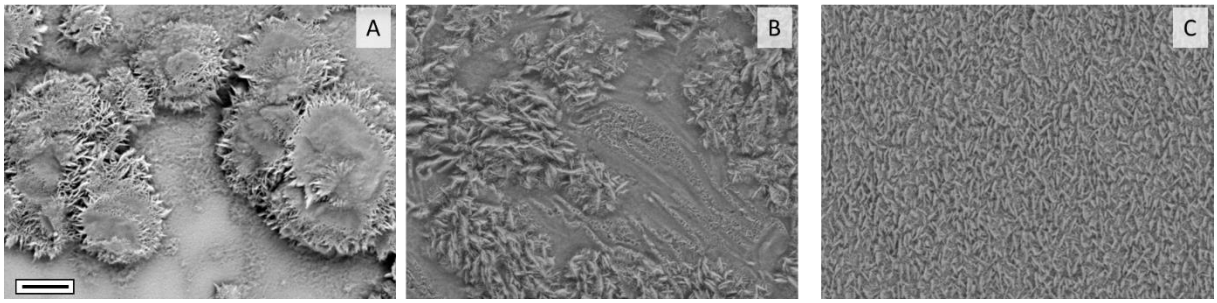

Figure 33: SEM images of palladium deposited from an LLC phase with A) Brij® 56, B) Brij® C10, C) $C_{16}EO_8$ for 2 C·cm^{-2} at 0.2 V vs Ag/AgCl. WE: Au-coated glass slide, A=0.25 cm^2. Scale bar, 5 µm
LLC phase : 12 wt.% $(NH_4)_2PdCl_4$, 40 wt.% H_2O, 48 wt.% surfactant

The impact of the substrate during the ECD process has also been studied. So far, all the depositions were made on gold-coated glass electrodes.

Prior to each deposition, a surface treatment has been performed. The influence of this parameter has been studied. Oxygen plasma, piranha solution, cycling in sulfuric acid and immersion in isopropanol under ultrasound were used in order to improve the affinity between the electrolyte and the electrode surface. No noticeable evolution has been observed using these different surface treatments. Moreover, the relaxation time (the time during which the electrolyte is in contact with the substrate without applied potential) prior to the deposition has also been varied, without a substantial change of the morphology.

Another possibility is to change the nature of the substrate. We made depositions on platinum and compared them with the results obtained with gold substrates. The Brij® C10 and $C_{16}EO_8$ were used for the comparison and the results were analyzed by SEM (Figure 34). With Brij®, it can be seen that there is no significant difference between gold (A) and platinum (B) substrates. As seen previously, changing from Brij® to $C_{16}EO_8$ provides smoother surfaces, also with platinum substrates. For the comparison of the surfaces obtained on a gold substrate (C) and on platinum (D) with $C_{16}EO_8$, a slight improvement of the roughness is observed using platinum.

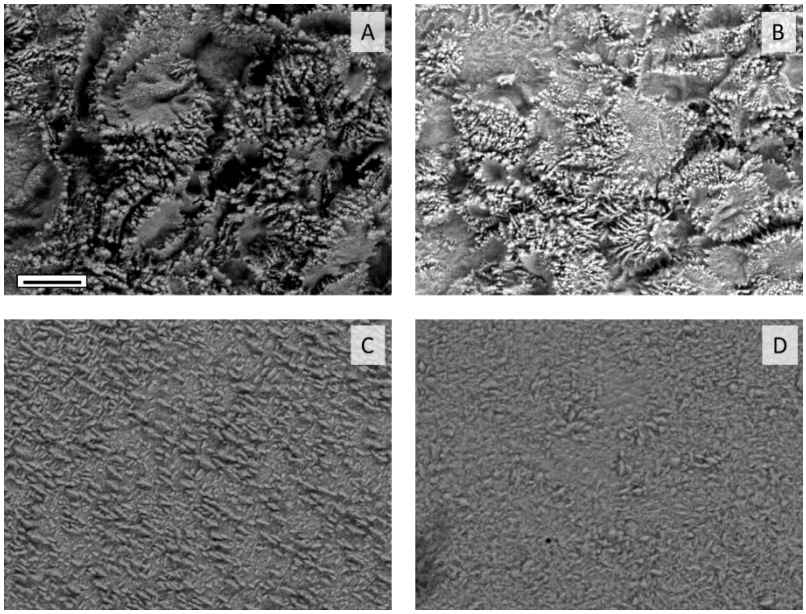

Figure 34: SEM images of palladium deposited from a LLC phase on Au-coated glass slide (A and C) and Pt-coated glass slide (B and D) with Brij® C10 (A and B) and $C_{16}EO_8$ (C and D) for 2 C·cm^{-2} at 0.2 V vs Ag/AgCl, A = 0.25 cm^2. Scale bar, 5 µm
LLC phase : 12 wt.% $(NH_4)_2PdCl_4$, 40 wt.% H_2O, 48 wt.% surfactant

Finally, deposits have been synthesized with different charge densities. Rising the injected charge increases the quantity of the product of the electrochemical reaction (Eq. 1) according to Faraday's law (Eq. 2):

$$Pd^{2+} + 2\,e^- \rightarrow Pd^0 \qquad \text{Eq. 1}$$

$$Q = \mathrm{z} \times n_M \times F \qquad \text{Eq. 2}$$

with Q being the injected charge [C], z the number of electrons exchanged during the electrochemical transformation, n_M, the mole number of the product of the reaction [mol] and F, the Faraday's constant (F = 96485 C·mol^{-1}). Furthermore, the mole number can be related to the thickness of the deposit (Eq. 3):

$$n_M = \frac{\rho_M \times e_M \times A}{\mathrm{M}_M} \qquad \text{Eq. 3}$$

with ρ_M being the density of the deposit [g·cm^{-3}], e_M, its thickness [cm], A, the area of the electrode [cm^2] and M_M, the molecular weight of the material [g·mol^{-1}].

Thus, the thickness can be related to the charge (Eq. 4):

$$e_M = \frac{Q \times M_M}{\rho_M \times A \times z \times F} \qquad \text{Eq. 4}$$

This equation give access to the maximum thickness reachable, assuming a faradaic yield of 100%. However, even if the yield is not maximal, an increase of the charge should lead to an increase of the thickness.

The variation of the injected charge has two objectives. On the one hand, morphological observations can indicate whether the deposition is diffusion limited or not. On the other hand, as we expect a mesoporous structure, thicker deposit should lead to an increase of the active surface area that can be measured by CV in sulfuric acid.

Four charge densities have been tested, 0.5, 1, 2 and 8 $C \cdot cm^{-2}$. The electrodes were observed by SEM (Figure 35). The electrode with the smallest charge presents the smallest grain size and an increase of the grain size is observed for a higher value of injected charge. This observation is in agreement with a depletion of palladium ions at the surface of the electrode. Indeed, for a low deposition charge the grains are rather small, but the surface is already rough, meaning that palladium ions are depleted at some part of the electrode surface (Scheme 6). Consequently, the irregularities will even further increase when the amount of deposited materials increases.

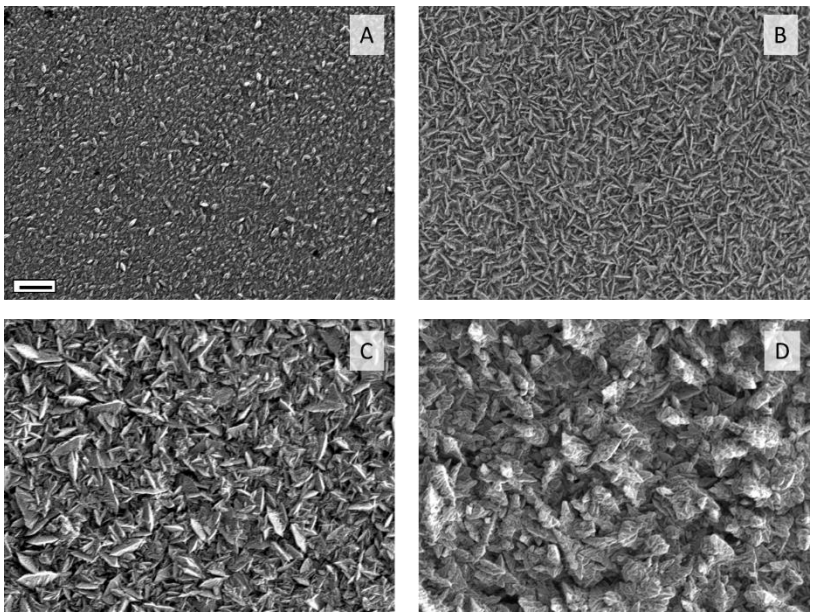

Figure 35: SEM images of palladium deposited from a LLC phase for A) 0.5 $C \cdot cm^{-2}$, B) 1 $C \cdot cm^{-2}$, C) 2 $C \cdot cm^{-2}$, D) 8 $C \cdot cm^{-2}$ at 0.2 V vs Ag/AgCl. WE: Au-coated glass slide, A = 0.25 cm^2. Scale bar, 1 µm
LLC phase : 12 wt.% $(NH_4)_2PdCl_4$, 40 wt.% H_2O, 48 wt.% Brij® C10

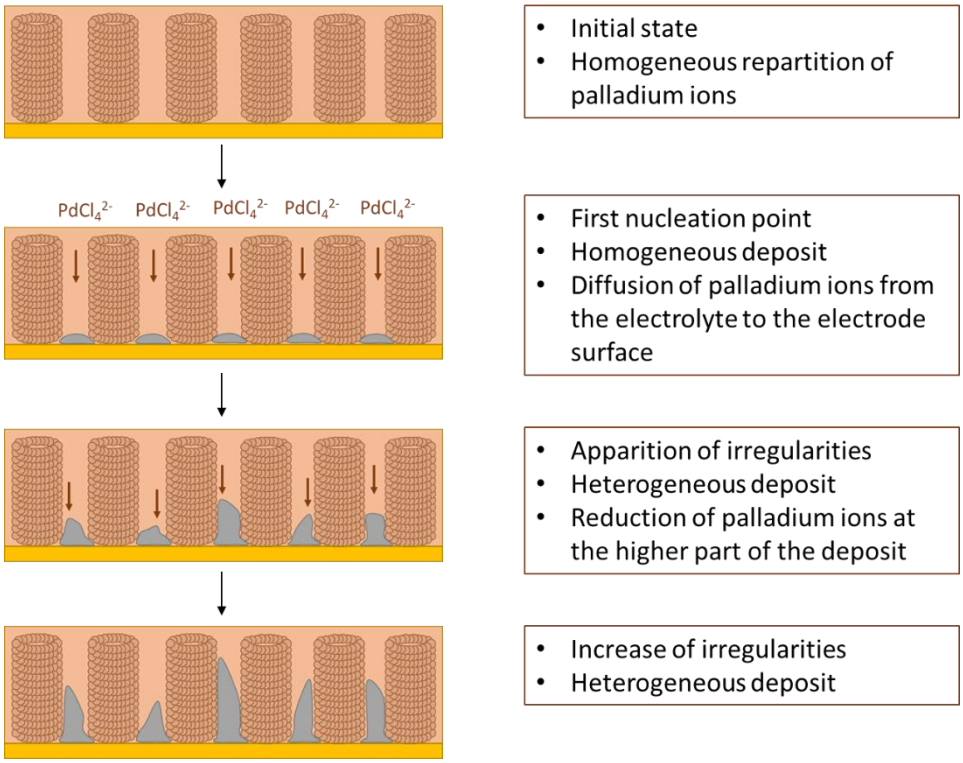

Scheme 6: Representation of the different steps of ECD from the beginning to the end.

However, even if a rough surface is observed in the SEM top view, it does not exclude the formation of mesopores. As explained previously, an increase of the charge leads to an increase of the thickness. In the case of mesoporous materials, increasing the thickness should lead to an increase of the active surface area, which can be evaluated by CV in sulfuric acid from the stripping peak of the palladium oxide.

CVs in sulfuric acid with the deposited palladium have been performed and compared with the CV of a flat palladium electrode (Figure 36). The potential limits were chosen in a way to record the oxidation/reduction of the palladium surface as well as the hydrogen region. The voltammograms show a similar level of current density for each electrode. Only the flat palladium presents a slightly lower current density. This difference is due to the fact that the palladium was polished prior to the CV so the surface was smooth, whereas the surfaces of the deposited palladium were rough, as it has been seen on the SEM images.

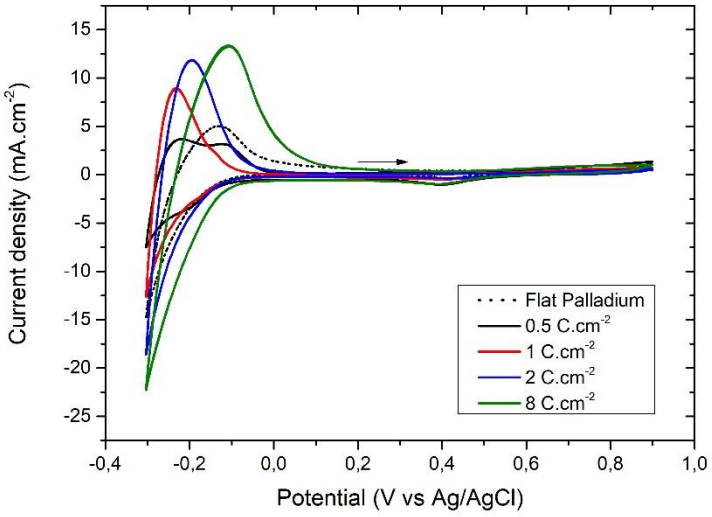

Figure 36: CVs performed in 1 M H_2SO_4 with palladium deposited from a LLC phase with different charge, 0.5 C·cm^{-2} (black line), 1 C·cm^{-2} (red line), 2 C·cm^{-2} (blue line) and 8 C·cm^{-2} (green line), compared to a flat palladium electrode (black dot line)

As there is no significant evolution of the current density despite an increase of the injected charge, it is unlikely that the deposited palladium is mesoporous. As the LLC phase has been checked by a polarized optical microscope, showing the hexagonal phase, the missing nanostructuration might be related to the electrodeposition step.

In summary, we studied many different parameters that affect the ECD process. We determined that a deposition potential of 0.2 V is the best option to produce homogeneous surfaces in a reasonable time to avoid drying of the electrolyte. Afterwards, the effect of the temperature was studied. The morphology obtained at 40 °C is more homogeneous than the one obtained at RT, certainly due to a better diffusion thanks to a lower viscosity of the electrolyte. At higher temperatures, the electrolyte evolves toward the micellar arrangement, which induces morphological changes. Then, it has been shown that the pure surfactant provides a more homogeneous surface compared to Brij®, but the surface still displays a high roughness. A study concerning the substrate have been conducted. Different surface treatments were applied without noticeable evolution. The change from gold to platinum slightly improves the homogeneity and the roughness of the electrode. Finally, the variation of injected deposition charge highlights depletion of the palladium ions at the electrode surface but especially, it shows that the deposited palladium is not mesoporous.

III. Conclusion and perspectives

In summary, we have studied the reactivity of flat palladium. A commercial electrode has been used to determine an appropriate SE. Hydrochloric acid and sulfuric acid were tested by CV. In agreement with the literature, an important oxidation reaction occurred in acidic media containing chloride. In sulfuric acid, a slight oxidation of palladium occurs starting from 0.6 V.

Afterwards, oxidation of the two enantiomers of DOPA has been studied by CV and DPV. First, no differentiation between the enantiomers could be observed since there are no chiral features present. Second, the oxidation of DOPA starts slightly before the palladium oxidation. For values more positive than 0.6 V the recorded current corresponds to an overlap of palladium oxidation as well as DOPA oxidation. For the planned enantiorecognition experiments, this feature is a drawback since the oxidation of palladium modifies the surface and thus, may modify the chiral selectivity.

To overcome this issue, the adsorption of DOPA has been studied. It has been show that DOPA molecules adsorb on the palladium surface spontaneously. Thus, the selectivity of the palladium electrode can be studied by adsorbing DOPA molecules and measuring the amount of adsorbed molecules by DPV.

After showing that the study can in principle be performed using DOPA, we tried to deposit mesoporous palladium (without impression) at a macroscopic scale following the procedure that was previously established for UME.

The composition of the electrolyte was chosen to allow the formation of a hexagonal phase of the surfactant according to the pseudobinary phase diagram. The amount of surfactant required to obtain the hexagonal arrangement results in a quite viscous electrolyte. This electrolyte was studied by CV in order to determine an appropriate deposition potential. A potential between 0.2 V and -0.1 V should lead to a palladium deposit. A too low potential would cause the co-reduction of palladium ions and hydrogen. It is necessary to avoid this situation since the palladium can store a high proportion of hydrogen which can change the structure of the deposit.

The electrodes were mainly analyzed by SEM. Varying the potential gave access to different morphologies, highly heterogeneous at high overpotentials (0.1 V and 0.15 V) and

rather homogeneous but rough at lower overpotentials (0.2 V and 0.25 V). The deposit at 0.25 V was too slow to ensure a constant concentration of water in the electrolyte, so a potential of 0.2 V has been selected for the following experiments.

Afterwards, several parameters have been studied, starting with the temperature. An improvement of the homogeneity is obtained at 40 °C compared to the results at RT, probably due to an easier diffusion of palladium ions. On the other hand, at 60 °C, a different morphology is observed which is more curved than the needle-shape observed for a lower temperature. An increase until 80 °C shows a completely different morphology with circular grains. This evolution of morphology is explained by the fact that at these temperatures, the electrolyte changes from a hexagonal organization to a micellar solution.

Different surfactants were used in order to reduce the roughness of the electrode: Brij® 56, Brij® C10 and $C_{16}EO_8$. The use of the pure surfactant improves the homogeneity of the deposit but still results in rough electrodes.

The influence of the substrate was also investigated. Several surface treatments were tested and different relaxation times were applied before the deposition without significant evolution. Finally, we studied two different materials, gold and platinum, as substrates with Brij® and $C_{16}EO_8$. No significant change has been observed with Brij®, but with $C_{16}EO_8$, the deposits appears smoother when platinum is used as substrate.

Finally, the injected charge has been varied. An evolution of the morphology has been observed. A higher charge provides rougher surfaces which is explained by the slow diffusion inside the electrolyte. Moreover, we performed CV in sulfuric acid with these electrodes obtained for different deposition charges. They should have a different thickness and thus present a higher active surface area by CV. The voltammograms show similar current densities for all electrodes, which are also close to the values observed with flat palladium. From these experiments, it can be concluded that the deposited palladium is not mesoporous.

The aim of this part was to find the appropriate conditions to obtain mesoporous palladium in order to perform chiral impression and then enantiodifferentiation and enantiosynthesis with these electrodes. However, none of the studies provided an encouraging evolution toward this goal.

A better understanding of the deposition mechanism should provide some insights to reach the mesostructuration at a macroscopic scale. Following the deposition by

electrochemical quartz microbalance could be one possibility, as well as a follow up by XRD at different stages of the deposition.

Finally, we decided to work with UME as mesoporous palladium has been already obtained on such substrate. The first step was to reproduce the mesoporous structuration and then perform the chiral impression to evaluate if the palladium can retain the chiral information in its structure. The results are presented in the next chapter.

IV. References

[1] C. Wattanakit, Y. B. S. Côme, V. Lapeyre, P. A. Bopp, M. Heim, S. Yadnum, S. Nokbin, C. Warakulwit, J. Limtrakul, A. Kuhn, *Nat. Commun.* **2014**, *5*, 3325.

[2] S. Butcha, S. Assavapanumat, S. Ittisanronnachai, V. Lapeyre, C. Wattanakit, A. Kuhn, *Nat. Commun.* **2021**, *12*, 1314.

[3] S. Assavapanumat, M. Ketkaew, A. Kuhn, C. Wattanakit, *J. Am. Chem. Soc.* **2019**, *141*, 18870.

[4] J. Genesca, R. Duran, *Electrochimica Acta* **1987**, *32*, 541.

[5] P. N. Bartlett, B. Gollas, S. Guerin, J. Marwan, *Phys. Chem. Chem. Phys.* **2002**, *4*, 3835.

[6] P. N. Bartlett, J. Marwan, *Phys. Chem. Chem. Phys.* **2004**, *6*, 2895.

[7] M. Serrapede, G. Denuault, M. Sosna, G. L. Pesce, R. J. Ball, *Anal. Chem.* **2013**, *85*, 8341.

[8] M. Serrapede, G. L. Pesce, R. J. Ball, G. Denuault, *Anal. Chem.* **2014**, *86*, 5758.

Chapter III - Mesoporous palladium at ultramicroelectrodes

In the previous chapter, we tried to synthesize mesoporous palladium at the macroscopic scale from a lyotropic liquid crystal (**LLC**) phase. Several electrochemical and physico-chemical parameters have been varied in order to reduce the roughness of the deposit without success. Moreover, the variation of the injected charge did not confirm the mesoporous structuration of the deposit. Our assumption to explain these observations is that the mass transport rate is too low due to the high viscosity of the plating mixture and thus it results in a more chaotic deposition.

The goal of this part is to obtain a mesoporous structure which can be imprinted with chiral information as it has been already shown with platinum [1,2], a platinum-iridium alloy [3] and nickel [4]. Mesoporous palladium has already been obtained by using ultramicroelectrodes (**UME**) as a working electrode (**WE**) [5]. Therefore, this chapter will be devoted to the use of UME to obtain the desired structuration.

In this introduction, UME will be presented. A first part will deal with some theoretical considerations which explain why these electrodes are better in terms of transport processes. Then, their advantages will be presented.

I. Ultra microelectrodes

I.1. Presentation

To be qualified as UME, the electrode needs to have at least one dimension smaller than the scale of the diffusion layer [6], δ, which is a characteristic length close to the electrode surface where the electrolyte is not influenced by natural convection.

During an electrochemical reaction; one or several species are consumed at the electrode surface. This induces a local depletion of the reactive species. Therefore, a concentration gradient appears locally at the electrode. The distance to the electrode where this gradient exists, is the diffusion layer. This length is constant in a stationary mode (with forced convection for instance) but is time-dependent in a transient mode:

$$\delta = \sqrt{\pi D t} \qquad \text{Eq. 5}$$

with D being the coefficient diffusion and t, the time of experiment

Thus, this distance increases with the time of the experiment and leads to evolving concentration profiles (Figure 37).

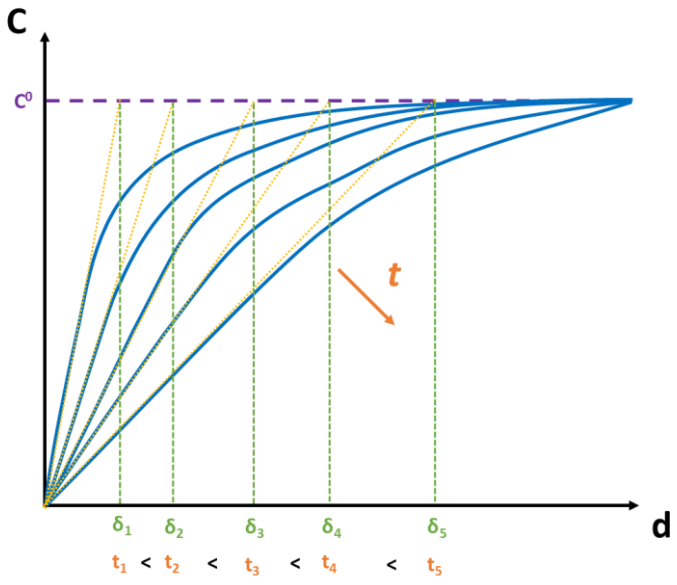

Figure 37: Concentration profiles of a reactive species at the electrode surface for different times of the experiment

In the literature, a value of 50 µm for the diameter is predominant to qualify electrodes as UME [7]. They can be made out of several materials such as platinum, gold, iridium or carbon

fibers, which are embedded in an insulating material. Different geometries can be obtained depending on the synthesis process (Scheme 7) [8,9]. The most used geometry is the disk configuration.

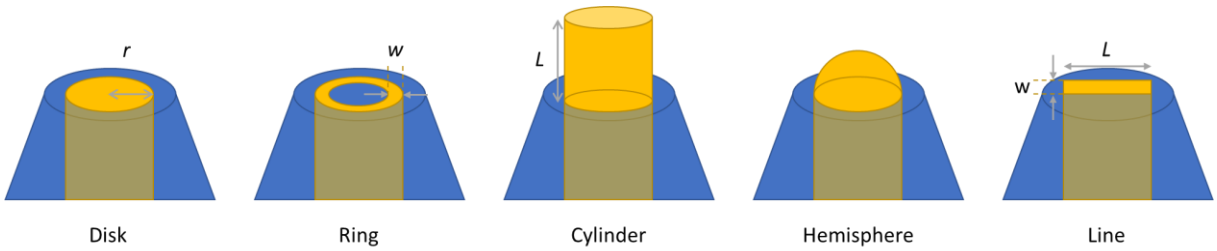

Scheme 7: Representation of different UME geometries and their characteristic dimension: r, the radius, w, the width, L the length

I.2. Theory

The electroactive species can move in the solution by three different modes (Scheme 8):

- Convection: it is a global motion of the whole solution. It can be natural or imposed. In the first case, it is the consequence of inhomogeneities present inside the solution (gradient of density, temperature, pressure…). In the second case, an external stimulus induces the motion such as in the case of a rotating disk electrode (**RDE**) or a magnetic stirrer.
- Migration: The charged species move under the influence of an electric field. This mode is specific to each species.
- Diffusion: it is another mode specific to each species. Diffusion occurs when there is a concentration gradient and tends to homogenize the distribution of the species. It mainly concerns the electroactive species since the non-electroactive species are not supposed to react at the electrode. However, in some cases, chemical reactions can follow electrochemical reactions which would induce the diffusion of even non-electroactive species.

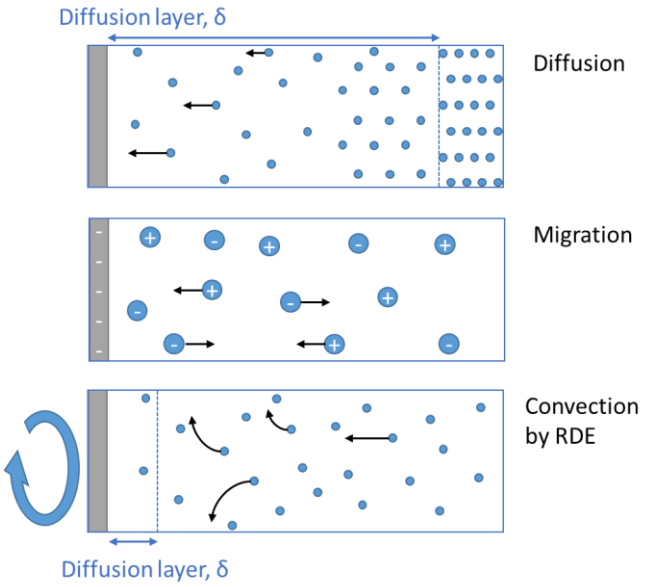

Scheme 8: Representation of the three different mass-transport modes

It is possible to express a flux (*J*) for each species which is influenced by a gradient of one or several parameters. The Nernst-Planck equation gives the flux to an electrode (for one dimension):

$$J(x,t) = -D\frac{\partial C(x,t)}{\partial x} - \frac{zFDC}{RT}\frac{\partial \phi(x,t)}{\partial x} + C(x,t)V(x,t) \qquad \text{Eq. 6}$$

Where:

- D is the diffusion coefficient
- $\frac{\partial C(x,t)}{\partial x}$ is the concentration gradient
- z is the charge of the electroactive species
- F is the Faraday constant
- C is the concentration of the electroactive species
- R is the gas constant
- T is the temperature
- $\frac{\partial \phi(x,t)}{\partial x}$ is the potential gradient
- V(x,t) is the hydrodynamic velocity

The current is directly related to the flux:

$$i = -nFAJ \qquad \text{Eq. 7}$$

Where:

- i is the current
- n is the number of exchanged electron
- A is the electrode surface

Three separated terms are present in Eq. 6 related to each mode of transport. The first one corresponds to the diffusion (which is the Fick's first law), the second is related to the migration and the last one, to the convection. The simultaneous presence of the three mass-transport modes makes the interpretation of the measured current quite complicated.

Nevertheless, this equation can be simplified. Indeed, the migration of the electroactive species can become negligible in the presence of a supporting electrolyte (**SE**). The contribution of the convection can be removed by considering only the diffusion layer and limiting the study to this distance. In addition to these considerations, external stirring should not be performed. Thus, the flux can be express only by the gradient of concentration in a pure diffusional mode:

$$J(x,t) = -D\frac{\partial C(x,t)}{\partial x} \qquad \text{Eq. 8}$$

Hence, the current is described as

$$i = nFAD\frac{\partial C(x,t)}{\partial x} \qquad \text{Eq. 9}$$

It can be noticed that the diffusional flux is time dependent and this characteristic is described by Fick's second law:

$$\frac{\partial C(x,t)}{\partial t} = D\frac{\partial^2 C(x,t)}{\partial x^2} \qquad \text{Eq. 10}$$

This equation is valid for planar diffusion (Scheme 9).

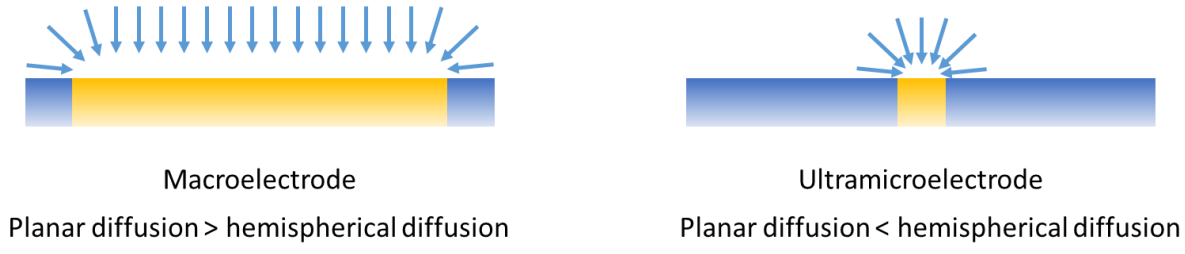

Scheme 9 : Representation of planar diffusion at a macroelectrode (left) and hemispherical diffusion at an UME (right)

When the size of the electrode decreases, edge effect contributions become more important and below a certain size (smaller than the diffusion layer), the planar diffusion becomes negligible with respect to the hemispherical diffusion. Thus, the system of coordinates needs to be changed into radial coordinates and this modifies the Fick's second law as

$$D\left[\frac{\partial^2 C(r,t)}{\partial r^2}+\frac{1}{r}\frac{\partial C(r,t)}{\partial r}\right]=-\frac{\partial C(r,t)}{\partial t} \qquad \text{Eq. 11}$$

The resolution of Eq. 11 gives the following expression for the flux for a spherical electrode

$$J(r,t)=-D(C^s-C^{el})\left[\frac{1}{\sqrt{\pi Dt}}+\frac{1}{r}\right] \qquad \text{Eq. 12}$$

Where *r* is the radius of the electrode and *t* the time of the experiment

By combining Eq. 7 and **Erreur ! Source du renvoi introuvable.**, the current is expressed as

$$i=\frac{nFAD(C^0-C^{el})}{\sqrt{\pi Dt}}+\frac{nFAD(C^0-C^{el})}{r} \qquad \text{Eq. 13}$$

During step potential experiments, depending on the overpotential, it can be assumed that the electroactive species are completely consumed at the electrode surface. Thereby, under pure diffusional conditions, the expression of the current for a spherical electrode becomes

$$i=\frac{nFADC^0}{\sqrt{\pi Dt}}+\frac{nFADC^0}{r} \qquad \text{Eq. 14}$$

The first term is the Cottrell equation and is related to the planar diffusion. The second term is related to the radial diffusion and is not time-dependent.

From Eq. 14, a parameter can be defined to determine the predominant diffusion:

$$\frac{\pi Dt}{r^2}$$

When this ratio is much smaller than 1, planar diffusion is the most important diffusion mode. In the contrary, when it is larger than 1, radial diffusion is the favorite transport mode. Thereby, below a certain radius of the electrode, hemispherical diffusion becomes predominant

and thus time independent. When this condition is fulfilled, we speak about UME. Thus, the current is mainly due to the radial diffusion described by the global expression:

$$i \cong i_{radial} = arnFDC \qquad \text{Eq. 15}$$

where *a* is a parameter which depend on the electrode geometry:

Geometry	Values of *a*
Disk	4
Hemisphere	2π
Sphere	4π

I.3. Advantages

From the above sections, the advantages of the miniaturization of the electrodes can be deduced.

One of the most important changes compared to the macroscale is the mass transport. At the microscale, the radial diffusion is predominant, therefore a steady-state current is quickly established.

As discussed previously, the value of the ratio $\frac{\pi Dt}{r^2}$ determines the favorite diffusion mode. The radius of the electrode is important, but the time of the experiment can also impact the mass transport mode. Indeed, even with a UME, it is possible to observe diffusion-limited behavior at short time scales. To illustrate this feature, cyclic voltammetry (**CV**) experiments were carried out at different scan rates with the same electrode and the same solution (Figure 38) [10].

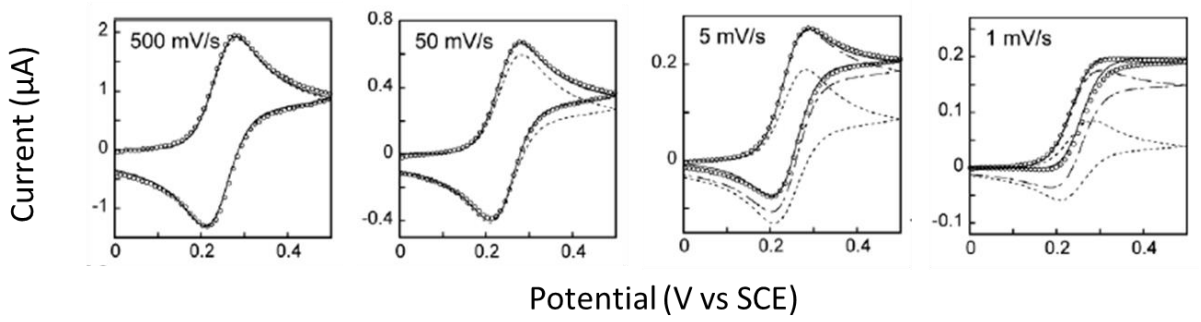

Figure 38 : CVs recorded in 2 mM $K_4Fe(CN)_6$ and 1 M KCl with a 250 µm radius Pt electrode (symbols) and comparison with theoretical CVs considering either planar diffusion (dashed curves) or radial diffusion with (solid curves) or without (long-short dashed curves) natural convection. Adapted from [10]

For slow scan rates, the CV shows a S-shaped curve which correspond to a steady-state behavior. When increasing the scan rate, the curves change toward peak-shaped curve which is related to a semi-infinite diffusion-limited reaction. These experiments were performed with a 250 µm radius Pt electrode, which is quite large to be consider as a UME, however, both behaviors (transient and steady-state) can be observed. The decrease of the electrode size allows increasing the scan rate until $MV \cdot s^{-1}$ to perform ultrafast CV [11].

During electrochemical experiments, the current is composed of two contributions, the faradaic and the capacitive charging current. The first is the current of interest which is related to the electrochemical reactions. The second is related to surface charge and is present each time the charge of the electrode surface is varied. Its presence disturbs the measurements, therefore, it is necessary to find solutions to increase the faradaic response and decrease the charging current. This current depends on the RC constant of the electrochemical cell and this parameter is directly proportional to the radius of the electrode. Thereby, UMEs are interesting to limit the influence of the capacitive current on measurements. On the other hand, the current density, *j*, at UME increases as the size of the electrode decreases

$$j = \frac{i}{\mathrm{A}} \qquad \text{Eq. 16}$$

And

$$i \propto r \; and \; A \propto r^2$$

Hence

$$j \propto \frac{r}{r^2} \; or \; \frac{1}{r}$$

This feature is an additional benefit to measure fast electron transfer experiments with a good signal-to-background ratio.

Another undesired aspect in electrochemical experiments is the ohmic drop. The polarization of electrodes induces a potential gradient and allows the passing of the current through the solution and hence leads to an ohmic drop. This can distort the experimental data, therefore, it is necessary to minimize its impact. Once again, the decrease of the electrode size is a solution to decrease the influence of this parameter.

A more basic aspect is their small size. Indeed, some experiments require to be performed in small volumes and thus, macroelectrodes cannot be used for these cases. Initially, UMEs were developed for biological purposes [12,13]. Another advantage of the small size of the electrode is to provide a good spatial resolution for scanning electrochemical microscope experiments [14,15].

In the previous chapter, we did not find a way to obtain mesoporous palladium at the macroscale. This obstacle might come from a too low diffusion rate. Indeed, the LLC phase is highly viscous and thus is an obstacle for the diffusion of the palladium species. So we decided to perform experiments at the microscale. The use of UMEs appears to circumvent this difficulty as showed in the literature [5].

In the following section, we will first focus on the deposition of palladium from a LLC phase. Brij® C10 and $C_{16}EO_8$ were used to perform electrochemical deposition (**ECD**) and the resulting morphology was analyzed by scanning electron microscopy (**SEM**). Then, CV was performed with the obtained electrode to measure the surface. In a second time, palladium was deposited from a LLC phase containing enantiomers to produce a chiral metal. The chirality of the deposits was tested by differential pulsed voltammetry (**DPV**).

II. Results and discussion

II.1. Non-imprinted mesoporous palladium

Prior to perform chiral impression in mesoporous palladium, ECD of mesoporous palladium on UME was performed in order to study the obtained material and compare the result with the material obtained at the macroscale.

As in the previous chapter, we prepared the LLC phase with the same proportion of components found in the literature [16]: 12 wt% $(NH_4)_2PdCl_4$, 40 wt% H_2O, 48 wt% surfactant.

A first electrolyte was prepared with Brij® C10. Depositions were performed on a platinum-coated glass slide and on a Pt UME at 0.1 V vs Ag/AgCl and with 2 $C \cdot cm^{-2}$ of injected charge. The obtained deposits were analyzed by SEM (Figure 39). The left image displays the result for the macroscopic electrode, whereas on the right is depicted the deposit on a UME. Both electrodes have a rough surface with irregularities. At the macroscale, a needle-shaped morphology is observed. At the microscale, needles are not observed, but some clusters appear.

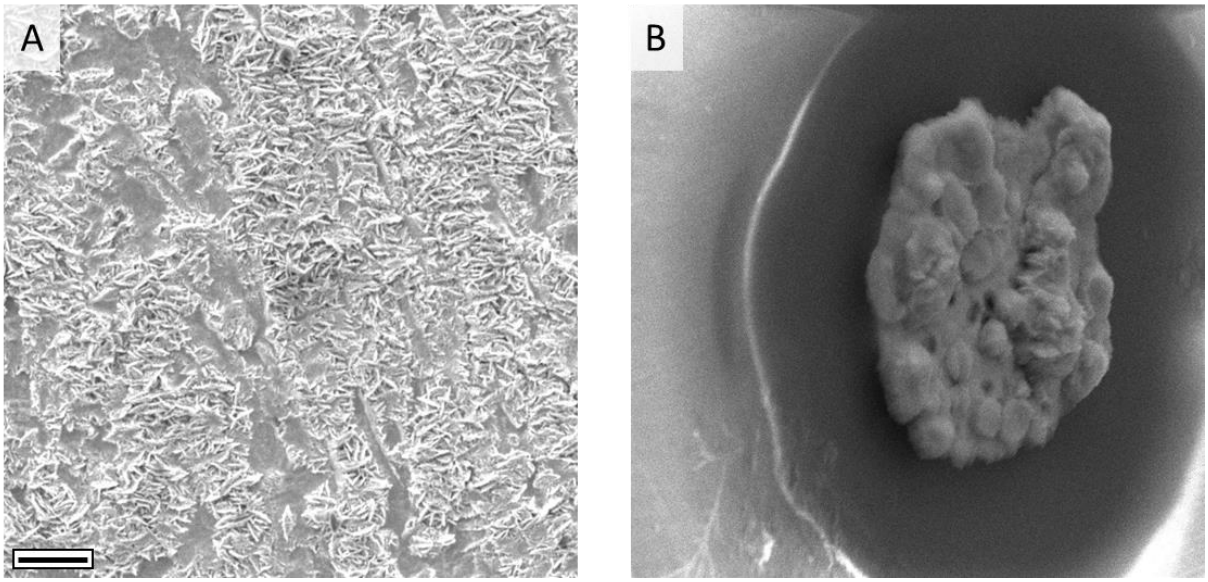

Figure 39 : SEM images of palladium deposited from a LLC phase made with Brij® C10. A) on a Pt-coated glass slide (A = 1 cm²) B) on a Pt UME (A = $7.8.10^{-7}$ cm²). Scale bar, 5 µm

Afterwards, we worked with the pure surfactant molecules, $C_{16}EO_8$. Again, two deposits were synthesized, one at the macroscale and a second one at the microscale. Their morphologies were observed by SEM (Figure 40). The morphology at the macroscale (left image) still presents irregularities, whereas the deposit on the UME presents a smooth surface (right image).

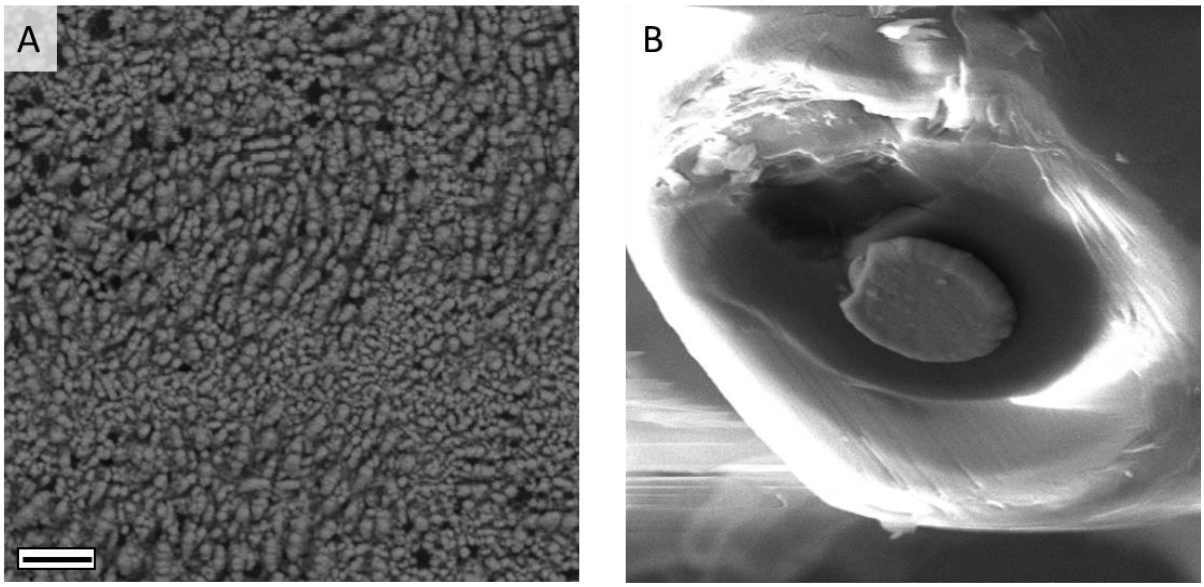

Figure 40 : SEM images of palladium deposited from a LLC phase made with $C_{16}EO_8$. A) on a Pt-coated glass slide (A = 1 cm²) B) on a Pt UME (A = 7.8.10^{-7} cm²). Scale bar, 5 µm

So far, it is not well understood, why $C_{16}EO_8$ provides a better morphology than Brij® C10. It might result in a better molecular arrangement since all the molecules have the same length.

From these observation, we decided to perform the following experiments by using $C_{16}EO_8$. We performed CV experiments in sulfuric acid in order to determine the electrochemical active surface area of this electrode (Figure 41). In total, 45 scans were recorded. For the first scans (left panel), the current related to the surface reactions, namely, the oxide formation and its stripping peak at the reverse scan, increases, from the curve in blue to the red one. From the 15th scan to the end of the measurement, the current falls down, from the blue curve to the red one (right panel).

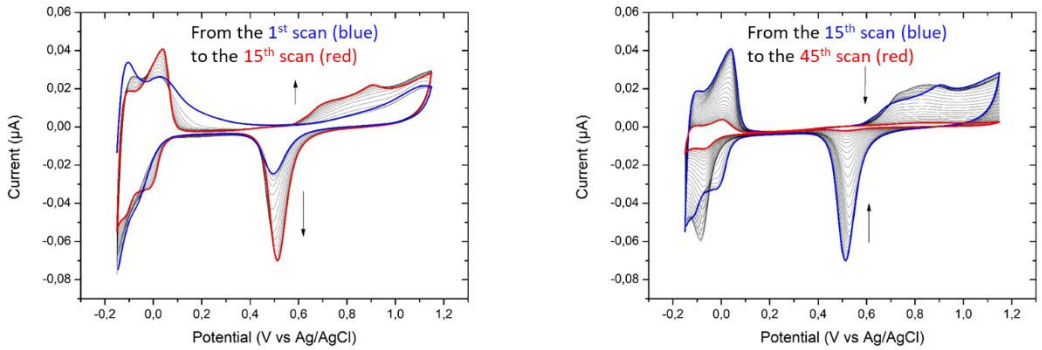

Figure 41 : CVs in 1M H_2SO_4 of an UME with palladium deposited from a LLC phase obtained with $C_{16}EO_8$

According to the literature, the current increases during the first scans and then stabilizes [16]. In the meantime, some authors reported that the oxidation current is related to the formation of palladium oxide but also to the dissolution of palladium, especially in acidic media [17–20].

In our case, we assume that the increase of the current is related to a cleaning of the electrode. Indeed, the deposition mixture is highly viscous. Even if the electrodes are soaked for at least 24h in water, we cannot be sure that the surface is completely free from surfactant and thus, cycling in sulfuric acid might remove remaining surfactant molecules from the nanostructure, giving access to a larger surface.

Another hypothesis is an uncontrolled partial dissolution of palladium which might increase the surface due to an increasing roughness. The subsequent decrease of the current could be related to the decomposition of the nanostructure. If a too high proportion of palladium is dissolved, then the hexagonal structure becomes too fragile and finally collapses. SEM images were taken before and after the CV experiment (Figure 42). After the CV, the deposit appears dug which is in agreement with the fact that the palladium was dissolved during the CV measurements.

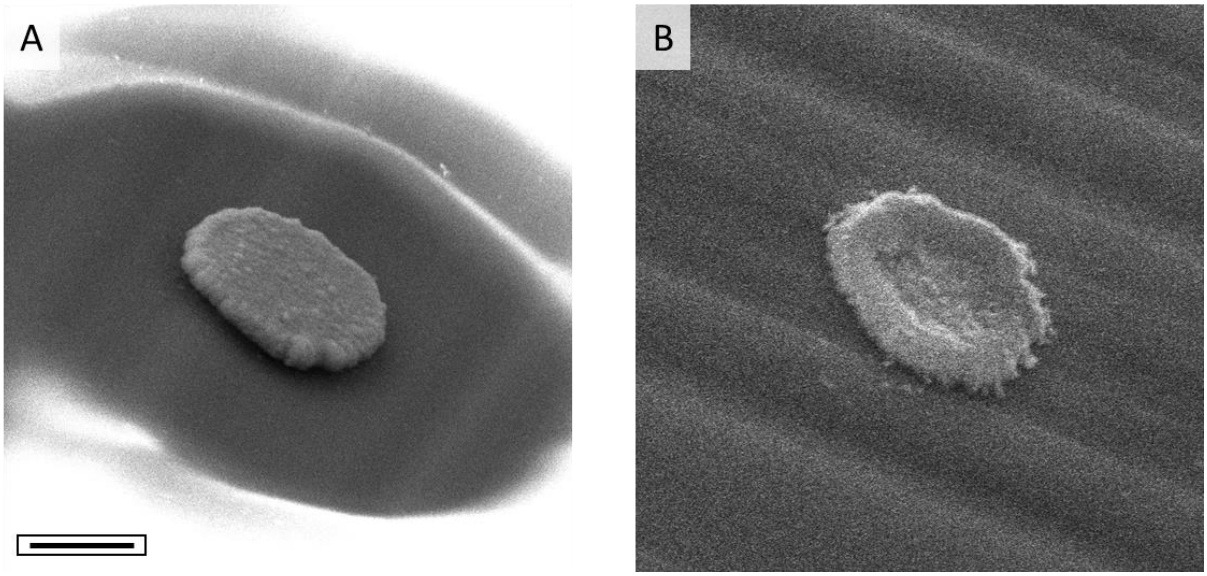

Figure 42: SEM images of deposited palladium from a LLC phase A) before CV, B) after CV. Scale bar, 5 µm

In order to know whether the deposited palladium is mesoporous or not, the charge related to the stripping peak of the oxide was measured and converted into surface area using a conversion factor of 424 $\mu C \cdot cm^{-2}$ [21]. We decided to use the first scan, even if some surfactant molecules could still be inside of the structure and hinder the measurement.

On the first scan, the integration of the reduction peak of the oxide gives an electroactive surface area of $6.5.10^{-5}$ cm² which is 100 times higher than the geometric area. Based on this result, we can assume that the palladium deposited from the LLC phase is mesoporous.

Afterwards, we synthesized new electrodes and added a chiral molecule in the plating mixture in order to create chiral cavities along the mesopores to induce chiral properties to the mesoporous palladium, as it has been done previously for platinum [1], platinum-iridium [3] and nickel [4].

II.2. Chirally-imprinted mesoporous palladium electrodes

II.2.1. DPV in DOPA solution

The aim of this work is to provide new materials with chiral properties for enantiorecognition and asymmetric synthesis. Electrodes were synthesized using LLC mixtures containing chiral molecules. From previous work performed with platinum, an optimum value seems to be 10 % of chiral molecule with respect to the amount of surfactant [2]. For this study, dihydroxy-3,4-phenylalanine (**DOPA**) enantiomers were used.

For a first series of electrodes, L-DOPA was added to the plating mixture. The obtained electrodes were used as WE to perform DPV in L- and D-DOPA solutions in order to define whether the electrodes are selective or not for DOPA oxidation. As it has been observed previously for other metals, we expect a differentiation in favor of L-DOPA since it is the imprinted molecule.

DPVs were performed in L- and D-DOPA solutions (Figure 43). Afterwards, CV experiments were performed to measure the surface of the palladium and thereby, the current density could be calculated allowing the comparison of the voltammograms. First of all, the end of the oxidation of L-DOPA (black line) is hidden by a side reaction. In the D-DOPA solution, this reaction is not observed. However, this current shape is not related to the L-DOPA solution since it does not appear on all measurements and it can also be observed sometimes with D-DOPA solutions (a total of over 10 experiments for each enantiomer). This oxidation seems to appear randomly. One hypothesis could be that some surfactant molecules are still present inside the pores and that the electron transfer occurs through the surfactant layer, hence at a

higher oxidation potential as the electron transfer is more difficult. Thereby, the cleaning procedure should be changed to obtain a reproducible signal.

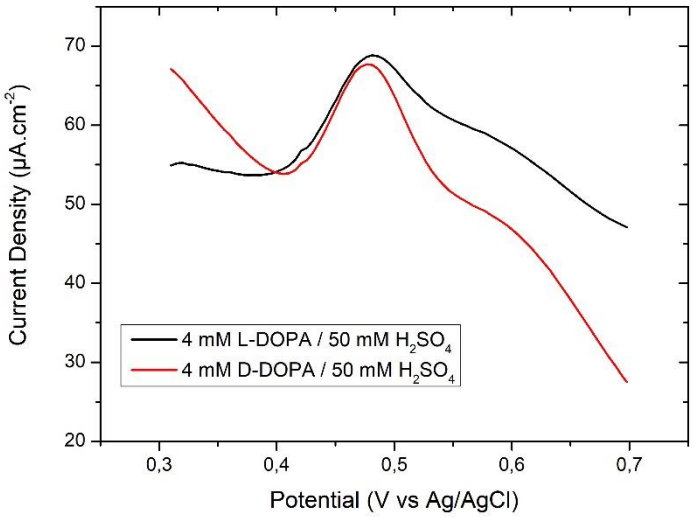

Figure 43: DPVs obtained in L-DOPA (black line) and in D-DOPA solution (red line) with a L-DOPA imprinted electrode

Nevertheless, it is obvious that there is no differentiation between the enantiomers. Two hypothesis could explain these observations. Regarding the randomly appearing oxidation signal beyond the DOPA oxidation, it could originate from surfactant inside the pores. Indeed, the structure is not perfectly organized in an hexagonal array, but is composed of many domains of different orientation [22]. The orientation as well as the size of the domains cannot be controlled. For some electrodes, the surfactant might have difficulties to leave the structure.

The second hypothesis is that the electrodes are not selective. We need to keep in mind that these deposits are synthesized on UME. Even if there is a mesostructuration of the layer, the geometrical area is roughly the same as for the bare electrode, which means that radial diffusion is predominant. The recognition concept is based on the presence of chiral footprints along the mesopores which allow the differentiation. Molecules which have the right conformation have access to the cavities whereas the “wrong” enantiomers react preferentially on non-imprinted surface (Scheme 10). However, in the case of UME, both enantiomers might mostly react at the outer part of the deposit which is the non-imprinted part, which could explain the non-selectivity of the electrodes.

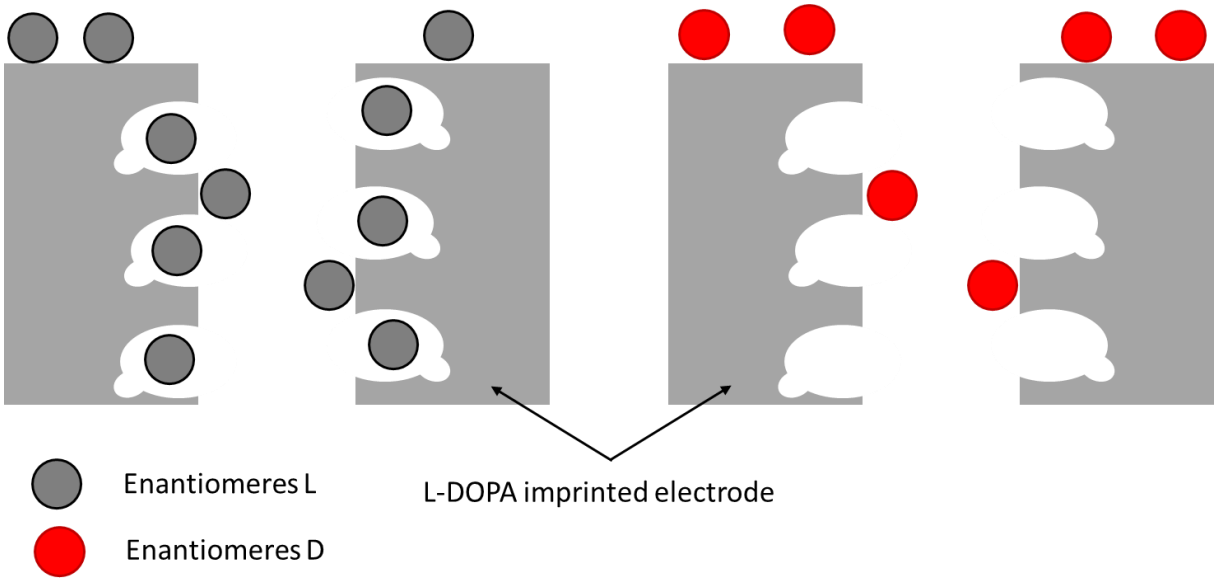

Scheme 10: Representation of L-DOPA imprinted electrode in presence of L-enantiomer (left) and D-enantiomer (right)

As shown in the previous chapter, DOPA molecules can be adsorbed at the palladium surface. As micrometer-sized electrodes seems to be a problem due to a dominating activity at the external surface, measuring only adsorbed molecules might circumvent this problem.

II.2.2. Detection of adsorbed DOPA by DPV

For the following experiments, DPVs were performed in SE only (50 mM sulfuric acid). A first voltamogram was recorded before the immersion in DOPA solution and a second one, after DOPA adsorption.

L-DOPA imprinted electrodes were used for the next experiments. The electrodes were rinsed in water for 24h. Afterwards, DPVs in SE were recorded, then the electrodes were soaked in L- or D-DOPA solution, and finally, new DPVs in SE were recorded (Figure 44). Finally, the surface of the electrodes was measured by CV in order to normalize the current of the DPV.

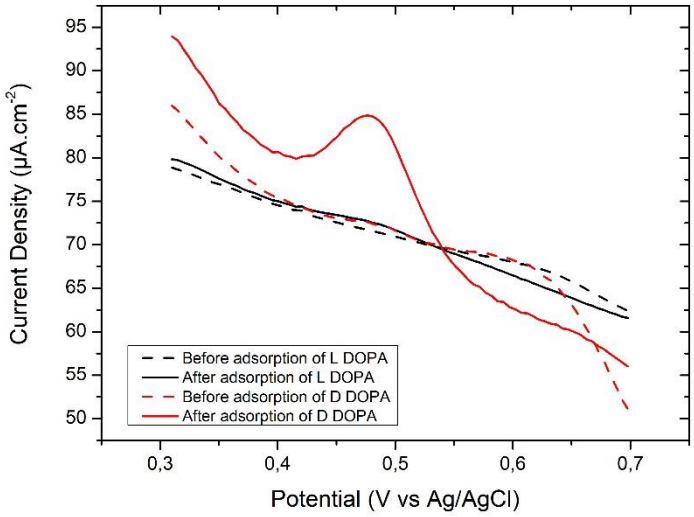

Figure 44: DPV in SE before (dashed line) and after (solid line) adsorption of L-DOPA (black line) and D-DOPA (red line). WEs: L-DOPA imprinted electrodes

As the first DPVs in SE do not show an oxidation peak, we can assume that there are no more DOPA molecules inside the electrode, eventually left over from the templating mixture. After the adsorption step, the electrode that was exposed to a D-DOPA solution shows an oxidation peak of the adsorbed molecules. However, for the electrode which was soaked in L-DOPA solution, no oxidation peak is detected. On the other hand, this behavior is not reproducible. Our assumption is the random cleaning of the electrode surface by a simple immersion in water which can be either complete or incomplete.

To deal with this hypothesis, we decided to compare the DPVs obtained after several CV in sulfuric acid in order to polarize the electrode and maybe help the cleaning of the pores. DPVs were recorded with electrodes which were not cycled in sulfuric acid, or which underwent 1, 2 or 3 cycles (Figure 45) and subsequently were used for the adsorption experiment.

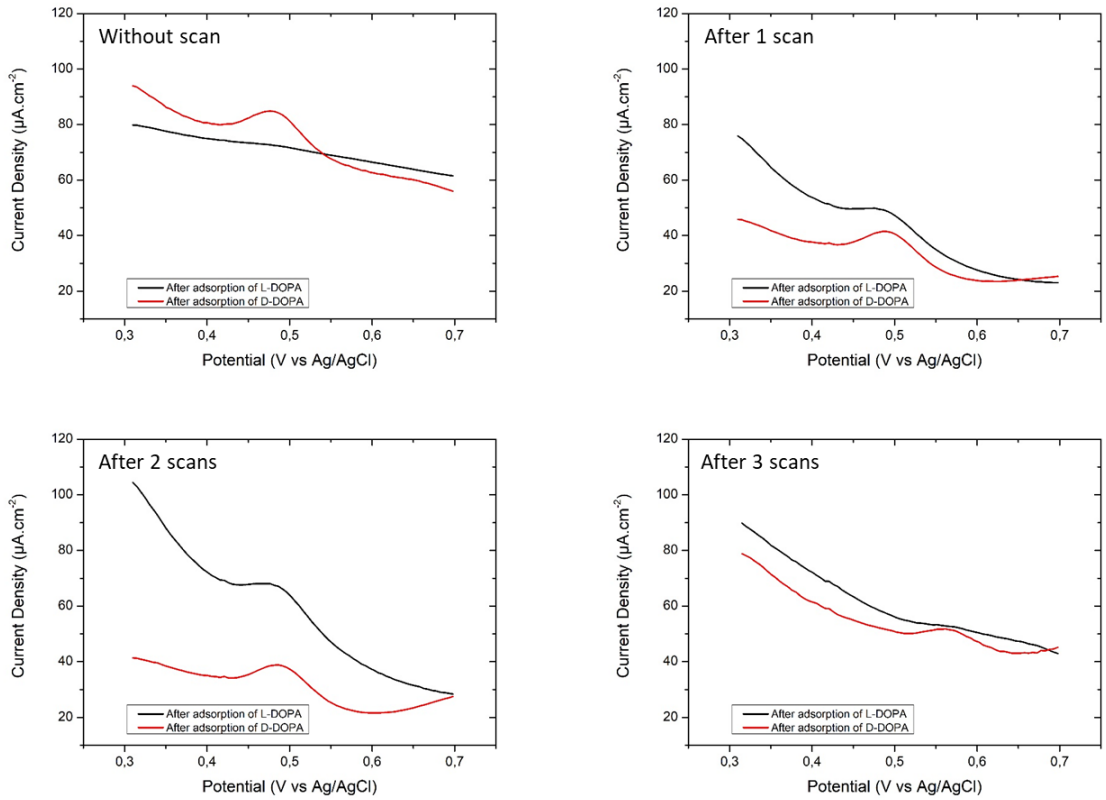

Figure 45 : DPVs obtained with L-DOPA imprinted electrodes after rinsing in water for 24h followed by 0, 1, 2 or 3 CV in sulfuric acid to clean the surface and finally, DOPA adsorption

The DPVs obtained without a preliminary scan in sulfuric acid show no oxidation after the immersion in L-DOPA, whereas there is an oxidation signal for the electrode immersed in D-DOPA solution. After one cycle in sulfuric acid, the signal for the D-DOPA remains constant and the signal for the L-DOPA increases, which indicates that the potential cycle activated the electrode surface and allowed the adsorption of L-DOPA. After two cycles in sulfuric acid, the signal for D-DOPA remains constant again and the signal for L-DOPA is slightly improved. After 3 scans, a potential shift is observed for the oxidation of D-DOPA, indicating a more difficult oxidation of the molecules, maybe due to a less effective adsorption. For L-DOPA, no oxidation peak is detected. This behavior might be explained by the fragile nanostructured deposit and the various changes of the solution (water, sulfuric acid, SE, then DOPA solution and finally SE again) together with the potential scans which could destroys the structure.

From these experiments, we decided to clean the electrodes in water for 24h and then, perform only one cycle in sulfuric acid prior to DPV to avoid damaging the nanostructure.

In these series of experiments, two kinds of electrodes were synthesized. One type was imprinted with L-DOPA and the other one with D-DOPA (Figure 46).

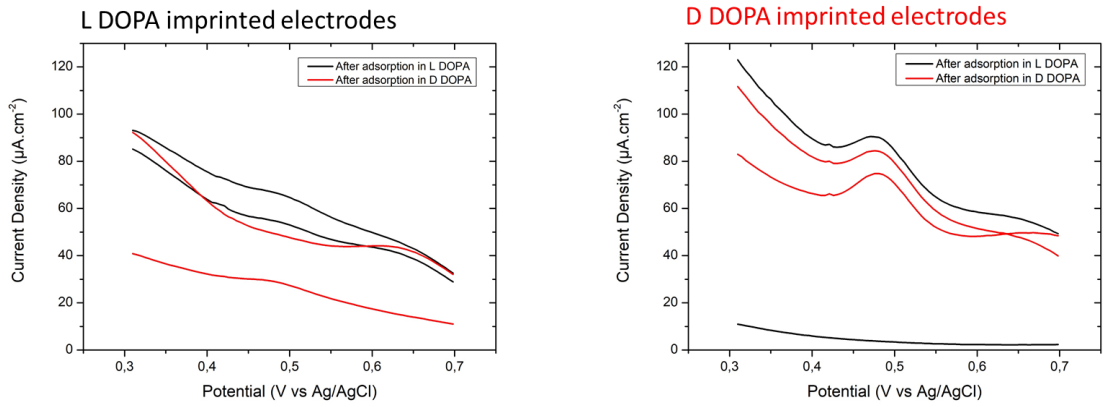

Figure 46 : DPV recorded in SE after immersion in L-DOPA (black lines) or in D-DOPA (red lines) with L-DOPA imprinted (left) or D-DOPA imprinted (right) electrodes.

The L-DOPA imprinted electrodes show a weak activity regarding the oxidation of each DOPA enantiomer. This could be explained by a non-efficient cleaning of the electrodes which could disturb the DOPA adsorption.

The D-imprinted electrodes have a higher reactivity. Indeed, each electrode which was immersed in D-DOPA solution displays an oxidation peak of the adsorbed molecules. For the electrodes immersed in L-DOPA, one shows an oxidation signal slightly weaker than the ones observed for D-DOPA, whereas the other voltamogram presents no sign of oxidation.

The difficulty with these results is to find a trend because the results are not reproducible. We finally performed statistics with all the obtained results.

For this statistical analysis, we gathered all the experiments performed after a rinsing in water for 24h and one cycle in sulfuric acid, which is the procedure which appears to provide the best answer regarding DOPA oxidation and to be the safest for the electrode structure.

We analyzed four cases (Figure 47):

- The L-DOPA imprinted electrodes immersed in L-DOPA solution (black column)
- The L-DOPA imprinted electrodes immersed in D-DOPA solution (hatched red column)
- The D-DOPA imprinted electrodes immersed in L-DOPA solution (hatched black column)
- The D-DOPA imprinted electrodes immersed in D-DOPA solution (red column)

We measured the charge related to the DOPA oxidation for each electrode, divided by the surface of the electrode. These statistics are based on 20 experiments for each case.

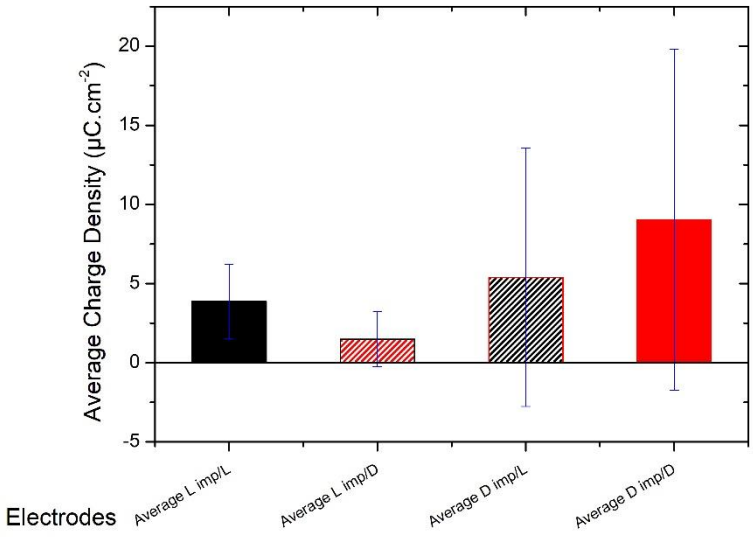

Figure 47 : Overall statistics of the enantiorecognition experiments

If we only look at the average charge density, we can notice that:

- For the L-DOPA imprinted electrodes, the average charge density related to the L-DOPA oxidation is higher than the one related to the D-DOPA oxidation
- For the D-DOPA imprinted electrodes, the average charge density related to the D-DOPA oxidation is higher than the one related to the L-DOPA oxidation

From these values, we could conclude that the electrodes are selective. However, taking into account the standard deviation, we can notice huge variations, which reflects the unpredictability and the lack of reproducibility of the system. This behavior is not explained so far, it could result from a non-reproducible deposition process or a difference in the nanostructuration which hinders the electrode cleaning and thus the subsequent adsorption. Moreover, we did not identify a preliminary experiment which could allow distinguishing an efficient electrode from an electrode which should not be used.

III. Conclusion and perspectives

To summarize, we first studied the deposition of palladium from a LLC phase using UMEs as WE. We saw that the use of an UME improves the morphology of the deposited palladium. Also, the use of $C_{16}EO_8$ provides a smoother surface than Brij® C10.

CVs were performed with the electrodes to check the mesoporosity of the deposit. Interestingly, the CV shows an increase of current during the first scans and a decrease from the 15^{th} scan. This behavior could be explained by a fragile structure and the partial dissolution of palladium at each cycle at the palladium oxidation potential, starting from 0,6 V vs Ag/AgCl. SEM images were taken before and after CV which seem to indicate palladium dissolution during the CV experiment.

Despite this observation, we calculated the electrochemically active surface area from the charge of the oxide stripping peak, which is related to the surface by a conversion factor of 424 $\mu C \cdot cm^{-2}$. The initial surface (at the first scan) appears to be 100 times higher than the geometric area, which is in favor of the presence of a mesoporous structure.

Afterwards, palladium was deposited in the presence of a chiral molecule, the DOPA enantiomers. The obtained imprinted electrodes were tested by DPV in DOPA solution. These first DPVs did not show a selective oxidation for the imprinted enantiomer. We assume that this is related to the electrode size which favors hemispherical diffusion. Thus the outer surface, which is not imprinted, is more active that the internal surface.

From this assumption, we decided to control the selectivity by adsorption. For the first experiments, higher oxidation currents were measured for D-DOPA, however the electrodes were imprinted with L-DOPA. Moreover, we observed irreproducible measurements, maybe due to a random cleaning of the electrodes.

Then, we studied the influence of a preliminary cleaning CV in sulfuric acid to see if this could help us to improve the reliability of the measurements. The signal after two scans appears to be the most promising, however, after 3 scans, the oxidation signal is completely lost. Thus, we decided to perform only one scan to prevent damaging of the structure.

Finally, L- and D- DOPA imprinted electrodes were compared. The cleaning procedure was 24h in water followed by a cycle in sulfuric acid. The results show a quasi-inexistent oxidation current in the case of L-DOPA imprinted electrodes, whereas the D-DOPA imprinted

electrodes displayed a more important activity for the DOPA oxidation. However, these behaviors were mostly random and we decided to analyze the results based on statistics.

The statistics show that globally, L-DOPA imprinted electrodes have a higher activity for L-DOPA and the D-DOPA imprinted electrodes, for the D-DOPA enantiomer. However, the standard deviation shows that the variations (20 electrodes for each series) are huge, which translates a non-reproducible behavior.

To pursue this work, it is essential to understand the reasons of the random measurements. The current assumption is a cleaning procedure which is not efficient enough. The electrodes could be soaked in other solvent, or the electrodes could be dried and heated in order to decompose the surfactant molecules. Ultrasound might be used to improve the cleaning procedure. However, it is necessary to keep in mind that the structure is fragile, that ultrasound can destroy the deposit and that heating might erase the chiral information due to surface diffusion of the atoms.

Once a procedure is defined and provides reproducible results, the possibility of performing synthesis could be studied. For this purpose, the use of UME is a drawback because of their small size. So far, mesoporous palladium could not be obtained at the macroscale, however, an electrode of 500 µm diameter provides still mesoporous palladium [16]. To circumvent this problem, arrays of micrometric-sized electrodes could be used to perform asymmetric synthesis.

From a more general point of view, the concept still lacks a detailed understanding especially at the molecular level. Indeed, it is assumed that chiral footprints are responsible for the geometrical recognition of molecules, however, they have not been directly observed so far. The difficulty is the small size of what needs to be characterized. One possibility could be to perform focused ion beam experiments coupled with transmission electron microscope, but the beam will damage the electrodes, and the surface structure might change due to the energy of the beam.

Complementary analysis could be performed such as X-ray diffraction with pole figures. This technique has been used by the group of Switzer to demonstrate the chirality of CuO [23]. It could, at least, indicate if the chirality of the electrodes is due to a lattice arrangement or not. A second option would be to perform optical measurement on these electrodes. Indeed, enantiomers were initially differentiated by optical methods and a chiral metal structure should also yield to a characteristic signal when examined with the right spectroscopical tools.

IV. References

[1] C. Wattanakit, Y. B. S. Côme, V. Lapeyre, P. A. Bopp, M. Heim, S. Yadnum, S. Nokbin, C. Warakulwit, J. Limtrakul, A. Kuhn, *Nat Commun* **2014**, *5*, 3325.

[2] C. Wattanakit, T. Yutthalekha, S. Asssavapanumat, V. Lapeyre, A. Kuhn, *Nat Commun* **2017**, *8*, 2087.

[3] S. Butcha, S. Assavapanumat, S. Ittisanronnachai, V. Lapeyre, C. Wattanakit, A. Kuhn, *Nat Commun* **2021**, *12*, 1314.

[4] S. Assavapanumat, M. Ketkaew, A. Kuhn, C. Wattanakit, *J. Am. Chem. Soc.* **2019**, *141*, 18870.

[5] T. Imokawa, K.-J. Williams, G. Denuault, *Anal. Chem.* **2006**, *78*, 265.

[6] I. Montenegro, A. Queiros, J. L. Daschbach, *Microelectrodes: Theory and Applications*, Vol. 197, Springer Science, Portugal, **1990**.

[7] A. J. Bard, L. R. Faulkner, *Electrochemical methods: fundamentals and applications*, 2nd ed., Wiley, New York, **2001**.

[8] Y. Liu, H. Cai, H. Li, *Journal of Manufacturing Processes* **2015**, *17*, 162.

[9] L. Danis, D. Polcari, A. Kwan, S. M. Gateman, J. Mauzeroll, *Anal. Chem.* **2015**, *87*, 2565.

[10] C. Amatore, C. Pebay, L. Thouin, A. Wang, *Electrochemistry Communications* **2009**, *11*, 1269.

[11] C. Amatore, E. Maisonhaute, G. Simonneau, *Electrochemistry Communications* **2000**, *2*, 81.

[12] J. Pandard, Etude de l'exocytose vésiculaire par détection couplée électrochimie-microscopie de fluorescence, Sorbonne Université, **2020**.

[13] C. Amatore, S. Arbault, M. Guille, F. Lemaître, *Chem. Rev.* **2008**, *108*, 2585.

[14] U. M. Tefashe, M. E. Snowden, P. D. Ducharme, M. Danaie, G. A. Botton, J. Mauzeroll, *Journal of Electroanalytical Chemistry* **2014**, *720–721*, 121.

[15] M. Serrapede, G. L. Pesce, R. J. Ball, G. Denuault, *Anal. Chem.* **2014**, *86*, 5758.

[16] P. N. Bartlett, B. Gollas, S. Guerin, J. Marwan, *Phys. Chem. Chem. Phys.* **2002**, *4*, 3835.

[17] D. A. J. Rand, R. Woods, *J. Electroanal. Chem.* **1972**, *35*, 209.

[18] A. E. Bolzan, M. E. Martins, A. J. Arvia, *J. Electroanal. Chem.* **1984**, *172*, 221.

[19] L. D. Burke, J. K. Casey, *J. Electrochem. Soc.* **1993**, *140*, 1284.

[20] M. Grdeń, M. Łukaszewski, G. Jerkiewicz, A. Czerwiński, *Electrochimica Acta* **2008**, *53*, 7583.

[21] D. A. J. Rand, R. Woods, *J. Electroanal. Chem.* **1971**, *31*, 29.

[22] K. A. Asghar, J. M. Elliott, A. M. Squires, *J. Mater. Chem.* **2012**, *22*, 13311.

[23] J. A. Switzer, H. M. Kothari, P. Poizot, S. Nakanishi, E. W. Bohannan, *Nature* **2003**, *425*, 490.

Chapter IV – Wireless electrochemical modifications of non-conductive substrates

Previously, we focused on chirality at the molecular scale. Thanks to top-down and bottom-up processes, it is possible to generate chiral objects at nanometer and sub-micrometer scales such as helices (Figure 48). Silica helices made from self-assembled gemini surfactants have been developed [1]. Such objects show interesting optical properties especially when they are covered by gold nanoparticles which enhance their circular dichroism response [2,3]. It has been shown that helices are also promising for motion [4]. Indeed, when they are covered by cobalt, they can act as autonomous swimmers under the influence of a magnetic field.

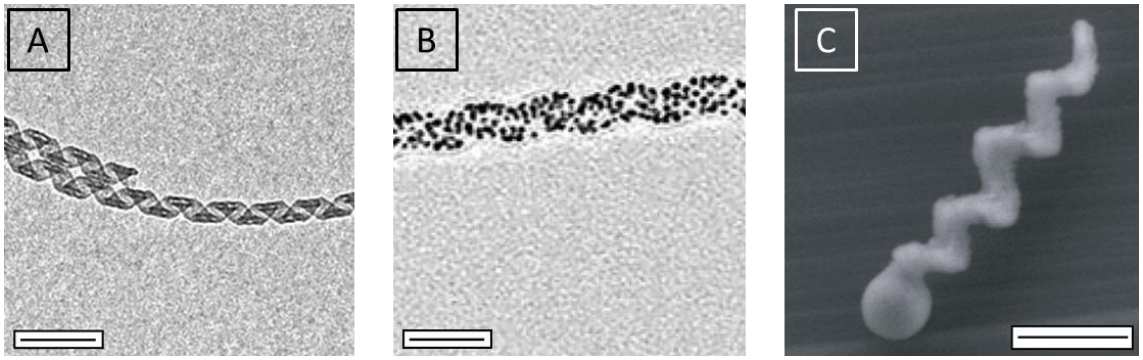

*Figure 48:Transmission electron microscope (**TEM**) images of (A) raw silica helices and (B) silica helices covered by gold nanoparticles. Scale bar, 100 nm. (C) Scanning electron microscope (SEM) image of silica helices prior to cobalt deposition. Scale bar, 500 nm. Respectively adapted from [1,3,4]*

We focused our interest on the development of an electrochemical procedure to modify silica nanohelices. The electroless deposition (**ELD**) process was selected to cover the helices by a layer of metal. This process allows a homogeneous metallic modification of substrates and is a powerful approach for non-conductive materials since no potential is required. Afterwards, such metallic helices might be used in a bipolar electrochemical (**BEC**) setup to induce asymmetric reactions on these substrates. BEC is an electrochemical concept based on the site selective polarization of a conductive object (the bipolar electrode, **BE**) in a wireless manner. The BE, under the influence of an electric field, experiences electrochemical reactions at its extremities, thus enabling a break of symmetry.

Our approach is to study such a procedure first at the centimeter scale and then decrease the size, adapt the geometry and the composition of the substrates. First, we used glass slides

that can be easily manipulated. Afterwards, the geometry has been changed and the size decreased by using glass beads (from 1 mm to hundreds of µm diameter). Finally, silica beads of 1 µm diameter have been used. These latter objects are the most similar to the silica helices in term of size and composition.

In the following sections, BEC will be explained with an emphasis on different key points of this method. The features of this technology allow using it for many applications and some of them will be presented. Afterwards, experimental results obtained during this thesis concerning the use of BEC for material modifications will be presented. As BEs need to be conducting or at least semi-conducting, we modified the substrates by ELD prior to BEC experiments.

I. Bipolar electrochemistry

The concept of BEC was observed more than 50 years ago [5–10]. It has found applications in electrosynthesis [11] or photoelectrochemical cells [12,13]. However, it is only since the beginning of the 21st century that this technology is attracting more and more interest. The phenomena which occur during BECs experiments have been widely studied and modeled (kinetic, electric field perturbation) [14–17]. BEC has opened interesting applications in various domains such as sensing and screening [18,19], motion [20,21] and material science [22,23].

I.1. Setup for bipolar electrochemistry

I.1.1. Electrodes

Usually, in conventional electrochemistry, two or three electrode-systems are used, a cathode and an anode which are physically distinct, and eventually a reference electrode. Each of these electrodes are directly plugged into and controlled by a potentiostat. In the case of BEC, only two electrodes are connected to a power supply (feeder electrodes) and a conductive object, the BE composed of the material of interest, is positioned in between. It is important to note that the BE is addressed by the electric field in a wireless manner, and thus, without direct electrical connection.

Feeder electrodes (also called source or driving electrodes) are plugged into a power supply and generate an electric field inside the electrochemical cell. Noble metals (mainly gold and platinum) are used as such electrodes. Indeed, BEC may require high voltages (from some V to MV) and therefore, it is necessary to use stable materials to avoid excessive electrochemical degradations. Also, it is important to use materials with a low resistivity to limit potential drops at the solution/electrode interface.

The most important electrode in BEC is the BE. This electrode is controlled without any electrical contact, only by the electric field imposed by the feeder electrodes. Under the influence of a sufficiently high electric field, the BE gets polarized with respect to the solution potential and can undergo faradaic reactions at each extremity facing the feeder electrodes, a reduction on one side and an oxidation on the opposite side. Indeed, the whole BE is at a homogeneous equilibrium potential in the electrolyte. When an electric field is applied, the

potential of the electrolyte changes across the cell. Therefore, the difference of potential at the interface between the conductive object and the solution along the BE evolves when going from one side to the other. In this configuration, a reduction and an oxidation can occur on the same object, thus there are two poles hence the term "bipolar" to qualify this technology.

I.1.2. Formalism

A difference of potential, $E_{imp} = E_a - E_c$, with E_a being the anode potential and E_c, the cathode potential, is imposed between two feeder electrodes separated by a distance L, thus inducing an electric field, $\mathcal{E}$:

$$\mathcal{E} = \frac{E_{imp}}{L} = \frac{E_a - E_c}{L} \qquad \text{Eq. 17}$$

The potential of the electrolyte, resulting from the imposed potential difference, E_{imp}, decreases linearly across the solution. Therefore, a conductive object placed in this electric field does not experience the same electrical field at different positions of the object (Scheme 11). The polarization potential, E_{pol}, varies along the object and is defined for a linear object as:

$$E_{pol} = \mathcal{E} \times x \qquad \text{Eq. 18}$$

With x being the position on the linear object.

For a spherical object, E_{pol} can be calculated with:

$$E_{pol} = \mathcal{E} \times \mathrm{r} \times \cos\theta \qquad \text{Eq. 19}$$

with r being the radius of the sphere and θ, the angle with respect to the electric field lines.

From these two equations (Eq. 18 and Eq. 19), it can be concluded that a maximum polarization is present at the extremities of the BE. The difference of potential between both extremities of BE can be defined as:

$$\Delta \mathrm{V} = \mathcal{E} \times d = E_{imp} \times \frac{d}{L} \qquad \text{Eq. 20}$$

With d being the length or the diameter of a linear or spherical object, respectively.

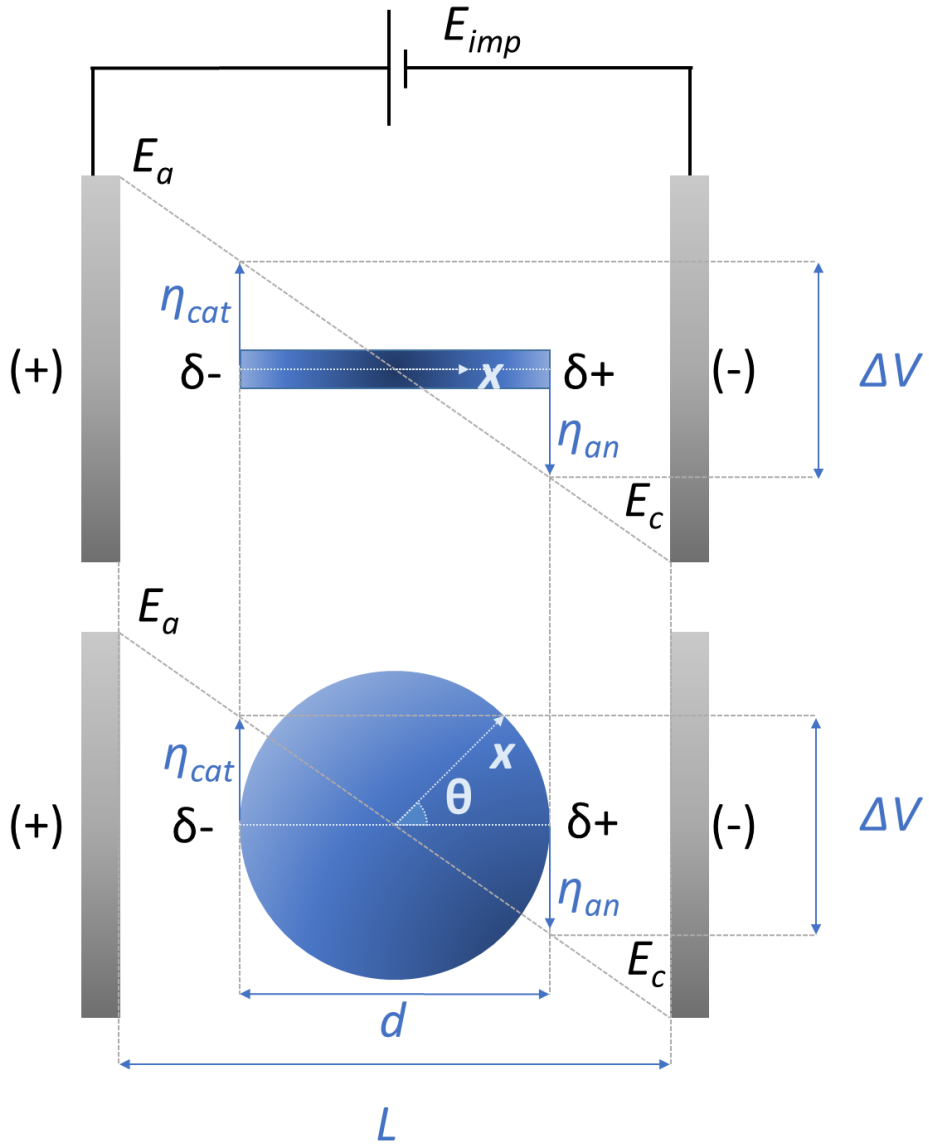

Scheme 11: BEC setup representing the polarization of a BE (linear and spherical objects) under the influence of an electric field imposed by the feeder electrodes (positive and negative poles). Illustration of the localized polarities on the BE (δ- and δ+), local overpotentials (η_{cat} and η_{an}) and the global potential difference experienced by the BE (ΔV).

The features presented above are general considerations to describe BEC experiments. What is interesting with this setup, is the possibility to induce electrochemical reactions on the BE without electrical contact.

When electroactive species are added to the electrolyte, they can undergo electrochemical reactions on the BE (Scheme 12).

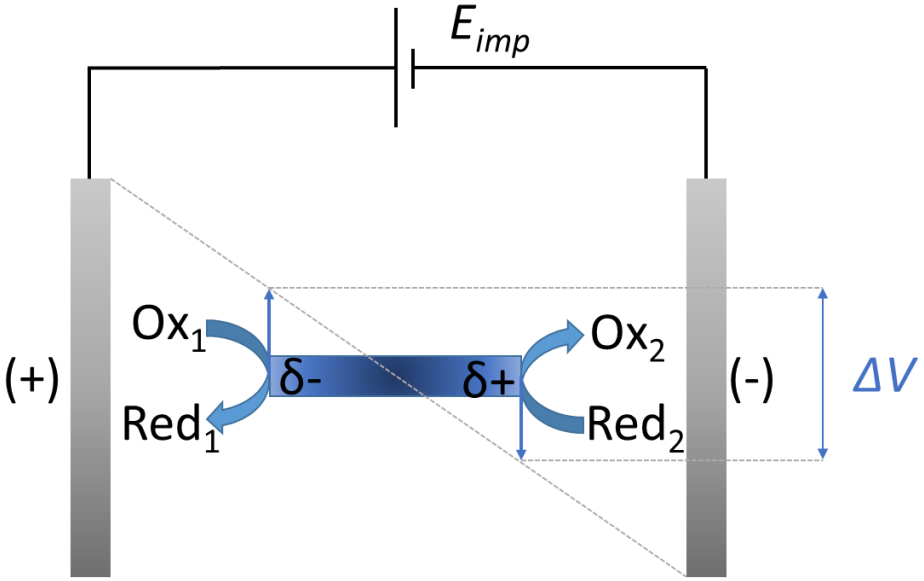

Scheme 12: Illustration of a BEC experiment when electroactive species are present in the electrolyte

Considering two redox couples:

$$Ox_1 + n_1\,e^- \rightarrow Red_1 \qquad \text{Eq. 21}$$

$$Red_2 \rightarrow Ox_2 + n_2\,e^- \qquad \text{Eq. 22}$$

with n_1 and n_2 being the number of electrons required for the electrochemical transformation of the two redox couples Ox_1/Red_1 and Ox_2/Red_2, respectively. In order to trigger the reactions of these couples on the BE, a minimum potential difference, ΔV_{min}, is required and can be defined by:

$$\Delta V_{min} = |E°_1 - E°_2| \qquad \text{Eq. 23}$$

with E_i^0 being the potential of the redox couple Ox_i/Red_i under standard conditions:

- Temperature at 25 °C
- Concentration of species at 1 mol·L^{-1}
- pH = 0

ΔV_{min} represents, in a first order approximation, the minimum potential difference required to induce the redox reactions at the extremities of the BE on each side of the object. Thus, the thermodynamic potentials of the redox couples are important to design the experimental set-up. However, it is not the only key parameter. As presented by the equations (Eq. 20), the length of the BE and the electric field are essential as well.

Loget *et al.* performed a series of experiments to illustrate the influence of these parameters [24]. First, they showed the impact of the electric field on graphite bars of the same length, *d* (Figure 49). They electrodeposited silver on the cathodic side under the influence of different electric fields for the same duration. They observed that below a certain electric field there is no deposition. Silver started to deposit above a limit value of electric field and the size of the deposit increased with the electric field until a maximum value.

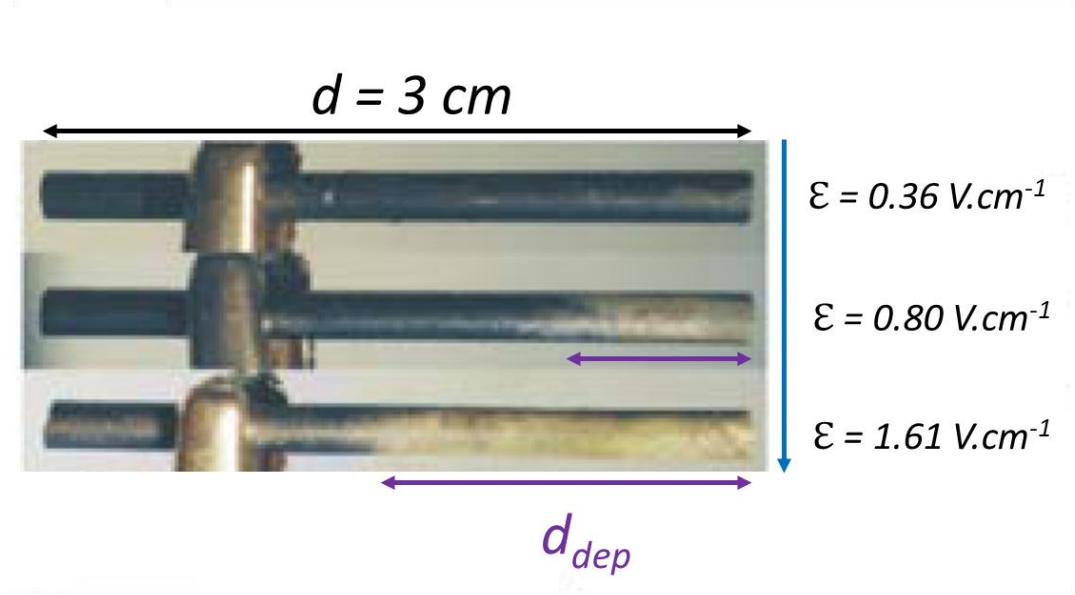

*Figure 49: Optical micrographs of graphite bars of the same length after bipolar electrodeposition (**BED**) of silver from a silver nitrate solution at different electric field values (adapted from [24])*

Afterwards, they showed the influence of the BE length with graphite bars of different sizes exposed to the same electric field (Figure 50). There is no deposition on BEs below a certain length. Above a threshold length, deposition can occur and the deposit covers a larger surface fraction on longer BEs.

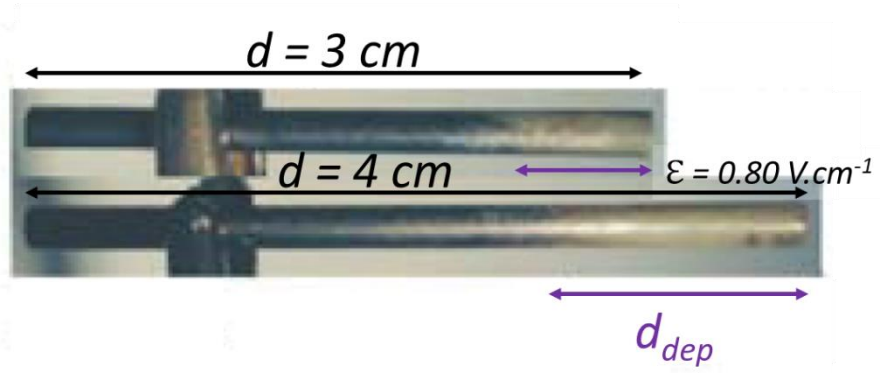

Figure 50: Optical micrographs of graphite bars of different lengths after deposition of silver by BEC at the same electric field value (adapted from [24])

These critical values are specific to one system and cannot be generalized. However, from these experiments, the impact of the electric field and the length of the BE on electrochemical reactions becomes obvious.

Another important parameter to take into account in electrochemistry is the current. Until now, we discussed mainly about potentials, but the current cannot be neglected, even in BEC.

A BEC cell without BE is similar to a classical electrolysis and thus, the whole current, i_{tot}, goes through the solution. However, when a BE is placed between the feeder electrodes, the current has two possibilities, either it goes through the solution, named the by-pass current, i_{bps}, or it goes through the BE, i_{BE} (Eq. 24 and Scheme 13).

$$i_{tot} = i_{BE} + i_{bps} \qquad \text{Eq. 24}$$

To favor the faradaic reaction on the BE, it is necessary to maximize the current going through the conductive object (i_{BE}). To reach this goal, it is beneficial to decrease as much as possible the conductivity of the solution (thus to increase its resistivity) by lowering its ionic strength and, simultaneously, to have the best conductivity for the BE.

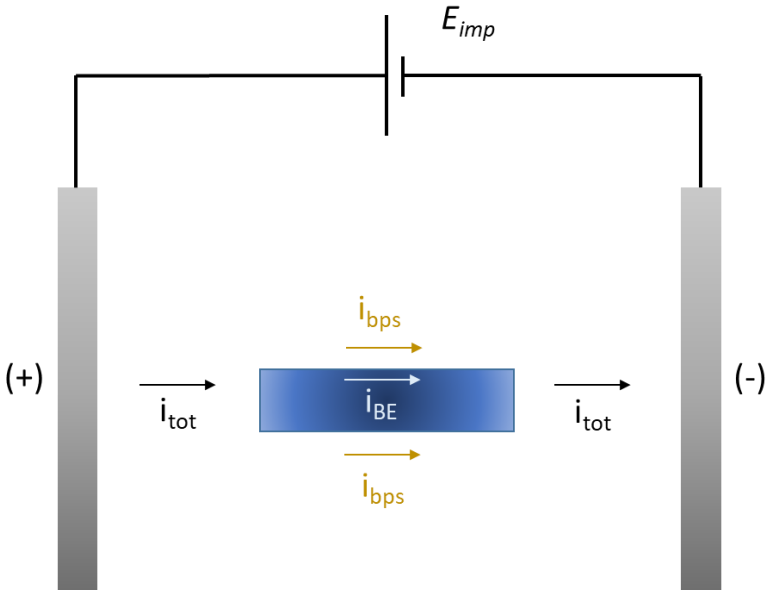

Scheme 13: Illustration of current pathways through a BEC cell

Several studies have been carried out to investigate the current in bipolar electrochemistry [25–29]. In particular, the BE current was studied by using a split BE [24]. This setup allows the direct measurement of the current going through the BE. Indeed, such electrodes are made of two separated conductive materials, immersed in the electrolyte, which are linked by two electrical connections that go outside the cell to be plugged into an ammeter (Scheme 14). Then, the by-pass current can be deduced according to Eq. 24.

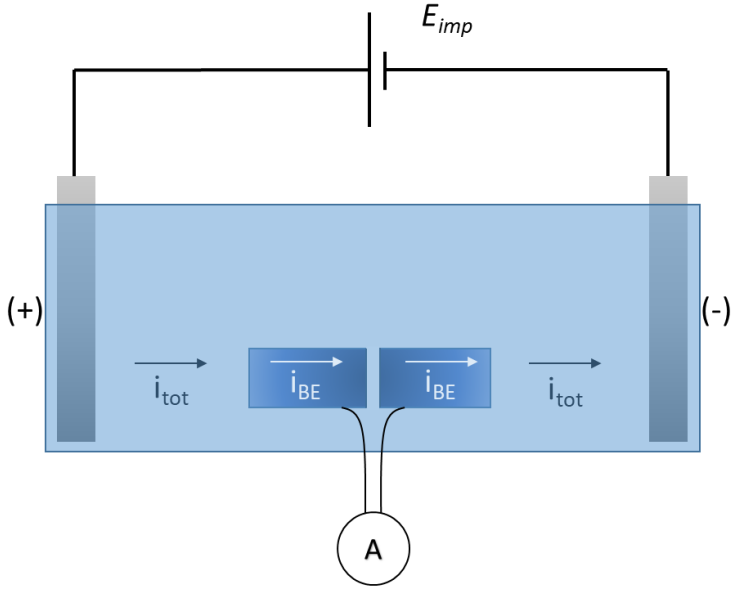

Scheme 14: Illustration of a split BE in a BEC cell

Experiments performed with split BEs showed the influence of the electric field as well as the concentration of charged species on i_{BE}. They confirmed the previous observations that

the electric field needs to be strong enough to allow a fraction of the total current to go through the BE and to induce the faradaic reactions. Moreover, they highlighted that the concentration of charged species has to be at a low level to favor the bipolar faradaic reactions.

In order to avoid the by-pass current, experiments can also be performed in so-called closed configurations [30–33], which means that the anodic and the cathodic compartments are separated (Scheme 15). The anodic and the cathodic parts are connected by the BE and the only way for the current to cross the cell is to go through the BE.

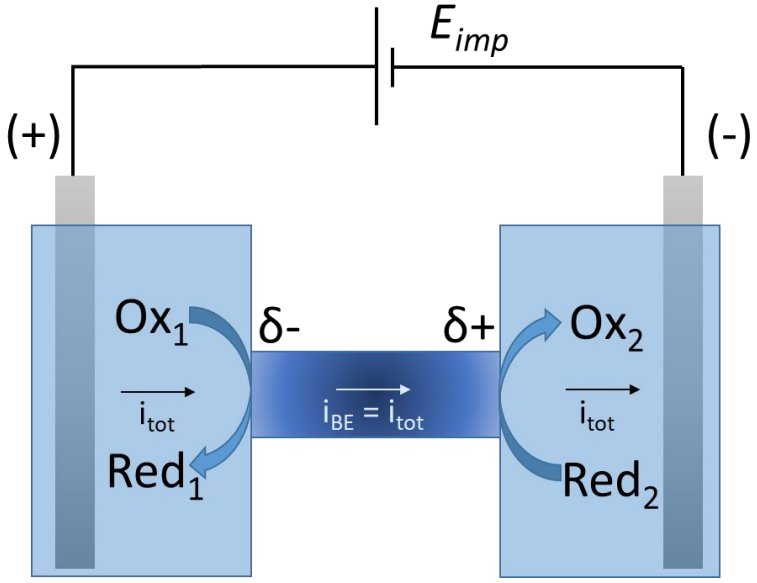

Scheme 15: Illustration of a BEC setup in a closed configuration

Previously, ΔV_{min} was introduced as the difference of the standard potentials of the electrochemical species in solution (Eq. 23). However, the formal potentials of these redox couples under BEC conditions are necessarily different since experiments are not performed under standard conditions (namely, a concentration of 1 mol·L^{-1} and pH = 0). Indeed, as we have just explained before, it is necessary to work at low ionic strength to favor the current through BE. In order to get closer to the effective potentials, linear sweep voltammetry (**LSV**) or cyclic voltammetry (**CV**) experiments can be performed in conditions near the ones used for BEC experiments.

The working electrode (**WE**) needs to be as similar as possible to the material used as a BE. The main difference in the experimental conditions is the electrolyte. In BEC, there is no supporting electrolyte (**SE**), whereas it is required for the voltammetric measurements. However, this difference should not disturb too much the estimation of the potential of each redox system and thus, the determination of ΔV_{min}.

Finally, experiments showed that the electric field and the length of BEs are two critical parameters in BEC. In the presence of redox species, it is possible to induce electrochemical reactions in a site selective way. The characteristic value of ΔV_{min} of a system can be studied by LSV or CV. Taking into account these considerations, BEC is a powerful technique enabling its use in many different fields thanks to the wireless addressing of the BE. We will now present some applications of the process.

I.2. Applications

BEC presents many advantages that allow applications in diverse domains. The wireless features, as well as the possibility of controlling several BEs at the same time, gives the opportunity to use it in analytical chemistry [34,35], for motion generation [20,36–38] and in material science [37,39,40].

I.2.1. Analytical chemistry

At the beginning of the 21st century, Manz *et al.* studied the possibility to develop sensors coupling BEC with electrochemiluminescence (**ECL**) [41]. ECL is a phenomenon of light emission obtained by the electrochemical generation of highly reactive species at an electrode surface. It presents many advantages for analytical applications such as high sensitivity, low background signal and since it requires an electron transfer, it can be used in BEC.

Usually, a reduction reaction is associated to the light emission induced by ECL located at the anodic side. Indeed, if a reaction requires electrons at one extremity of the BE, they need to be provided by the other end. This balance enables the correlation between both reactions occurring on each side of the BE. As seen previously with silver deposition, the electric field and the length of the BE are crucial parameters to control electrochemical reactions and, in the case of ECL, the light-emission (Figure 51 a) [42]. Another work shows the possibility to control 1000 BE at the same time using BEC [43]. The experiment showed a homogeneous emission of light which indicates that every BE experienced the same electric field inducing the same anodic and cathodic overpotentials (Figure 51 b).

One difficulty in BEC is the complexity to monitor the direct current going through BE. Some works showed the possibility to correlate the current with the intensity of ECL. This coupling allows the detection, but also the quantification of analytes by BEC [44].

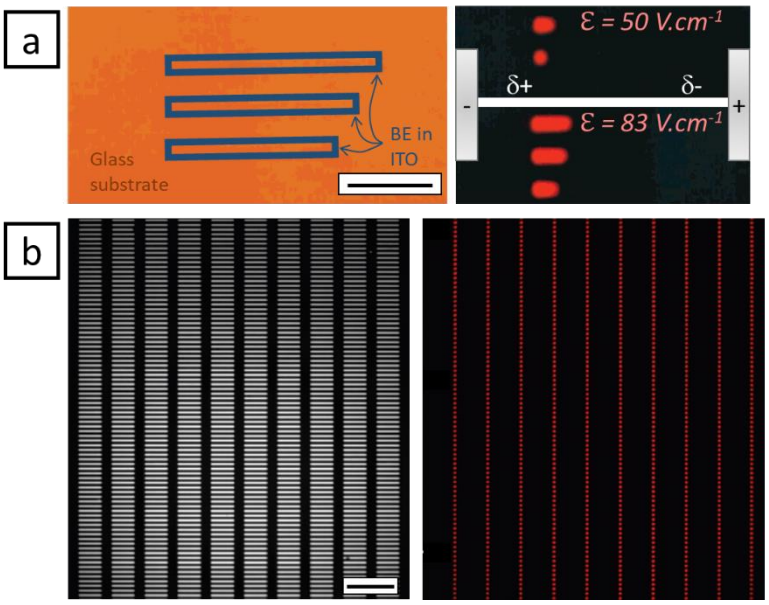

Figure 51: ECL coupled with BEC

a) Optical micrograph of BEs (left) and luminescence micrographs during light emission (right). Scale bar, 1 mm (adapted from [42])

b) Optical micrograph of an array of BE (left)and luminescence micrograph during the experiment (right). Scale bar, 200 µm (adapted from [43])

BEC can also be used to screen electrocatalysts. Fosdick *et al.* studied the efficiency of materials for reduction reactions like oxygen reduction reaction (**ORR**) [34] and hydrogen evolution reaction (**HER**) [45]. On the cathodic side, the BE carried the electrocatalyst to be tested and, on the anodic side microbands of sacrificial metals are deposited (silver or chromium). The material on the BE which induced the highest number of dissolved microbands is the best catalyst for the studied reaction. Indeed, when more microbands are dissolved, the distance between the two extremities decreases. As the electrochemical reactions on BE depend on this distance (Eq. 20), if under the influence of the same electric field, a catalyst (cathodic side) allows dissolution of more sacrificial material (anodic side), it means that the catalyst required a lower overpotential than the other materials to perform the electrochemical reaction. For ORR, it has been shown that platinum is more efficient than gold and that indium tin oxide (**ITO**) is the less efficient material among the three tested materials (Figure 52).

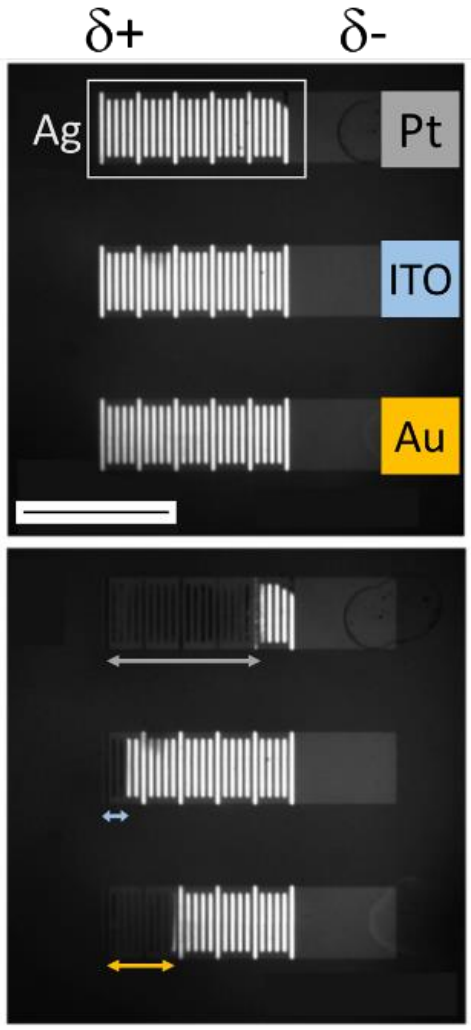

Figure 52: Optical micrographs of BEs with different cathodic compositions (platinum, ITO, gold) before screening (top), after screening (bottom). Scale bar, 500 µm (adapted from [34])

Finally, these works have shown that BEC is a powerful tool to detect analytes when coupled with ECL. In addition, it is very helpful to select new electrocatalysts among a large number of candidates in a simple and fast experiment.

I.2.2. Motion

BEC is also widely used to induce motion. Breaking the symmetry of a system is a requirement to induce a movement. By nature, BEC induces site-selective oxidation and reduction, generating the needed asymmetry to create the movement. The asymmetry can originate from the BE itself or can come from an asymmetric reactivity. For instance, water

splitting which induces an asymmetric production of bubbles for stoichiometric reasons, or the deposition/dissolution of a metal are reactions that can be used for this purpose. Below are some examples of motion induced by BEC.

In 2010, Loget *et al.* proposed to use BEC to induce motion by self-regeneration of metallic BEs [46]. The possibility of the BE to undergo site-selective oxidation and reduction allows to dissolve a metallic particle at one pole and to deposit the same metal on the other pole. This mechanism allows the metallic object to move from one feeder electrode toward the other one. An object made of zinc in a solution of zinc sulfate was used to illustrate this new mechanism (Figure 53). Moreover, working with the same redox couple on both sides of the BE decreases significantly the potential difference required at the extremities of the BE to induce the reaction and thus, the potential imposed at the feeder electrodes (Eq. 20).

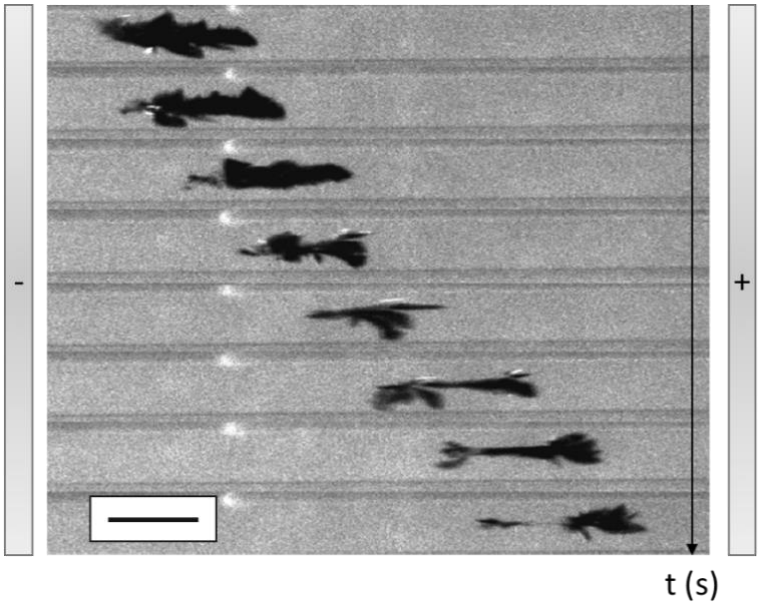

Figure 53: Optical micrographs of the movement of a zinc dendrite under the influence of an electric field. Scale bar, 100 µm (adapted from [46])

The same group also worked on the motion induced by asymmetric bubble production [20,36]. They showed the possibility of creating a linear or a rotational movement depending on the geometry of the BE (Figure 54). Firstly, they used the water splitting reaction:

$$2\,H^+ + 2\,e^- \rightarrow H_2 \qquad E° = 0\,V\ vs\ NHE \qquad \text{Eq. 25}$$

$$H_2O \rightarrow {}^1\!/_2\,O_2 + 2\,H^+ + 2\,e^- \qquad E° = 1.23\,V\ vs\ NHE \qquad \text{Eq. 26}$$

For the same amount of electrons, the reduction reaction produces twice more bubbles of hydrogen than the oxidation side produces oxygen. This asymmetric production of gas

induces a motion pushing the BE toward its anodic side (the feeder cathode). However, the production of gas on the anodic side slows down the motion. To overcome this drawback, the group coupled the reduction of protons with the oxidation of hydroquinone (**HQ**) into benzoquinone (**BQ**):

$$HQ \rightarrow BQ + 2\,H^+ + 2\,e^- \qquad E° = 0.70\,V\ vs\ NHE \qquad \text{Eq. 27}$$

On one hand, it prevents the production of oxygen gas, allowing a faster displacement. On the other hand, the potential for the oxidation of HQ is lower than the one required for the oxidation of water, thus, lowering the necessary potential.

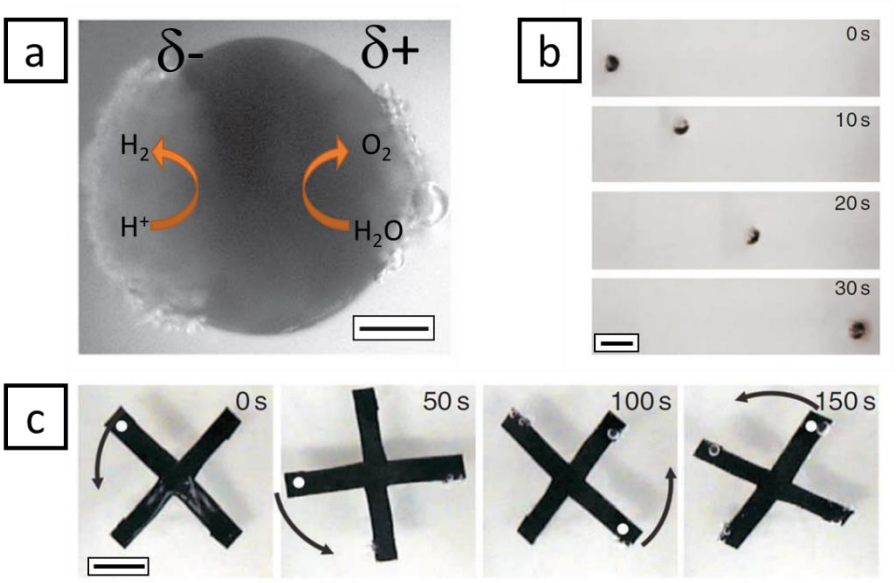

Figure 54: Optical micrographs of moving BEs (adapted from [20]). a) bubble production on a BE during a BEC experiment. Scale bar, 250 µm. b) Linear motion of a BE in HQ electrolyte. Scale bar, 2 mm. c) Rotational motion of a BE due to a different geometry. Scale bar, 5 mm

Recently, the actuation of conducting polymers controlled by BEC has also been studied [21,47]. Polypyrrole (**Ppy**) strips were used as BE. They were synthesized by chronopotentiometry on a gold surface and removed from the substrate after their synthesis. This process generates two different morphologies: the side which faced the solution during the synthesis is rougher than the side in contact with the perfectly flat gold substrate. Afterwards, the polymer was placed in a bipolar electrochemical cell. The anode-facing side of the polymer underwent a reduction, allowing cations to penetrate inside the Ppy strip and thus the polymer to swell. Moreover, the rough surface has a larger porosity and thus, the amount of cations which goes inside the polymer is higher compared to the smooth surface (Figure 55). This

asymmetric morphology associated with the asymmetric reactivity allows bending of the polypyrrole when it is attached [21] or the movement of the polymer when it is free-standing in the cell [47].

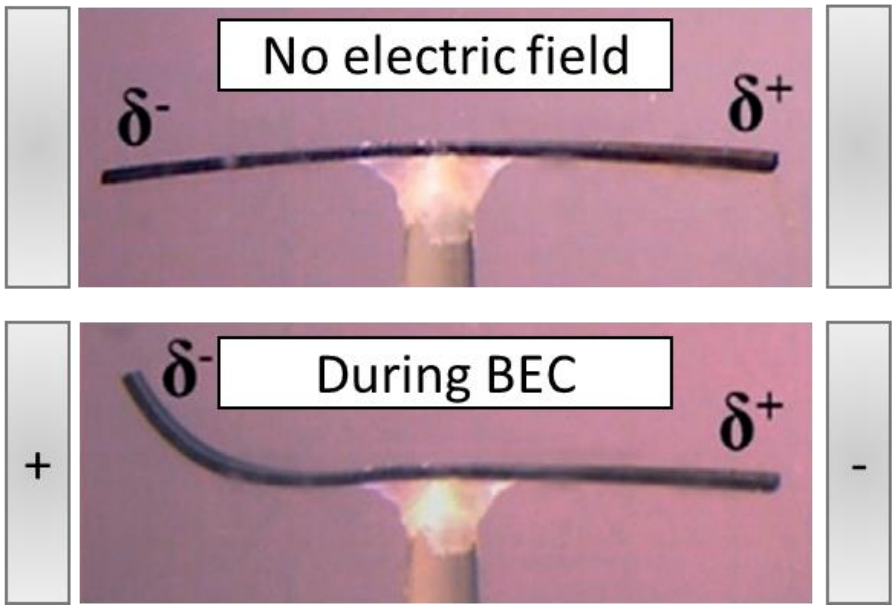

Figure 55: Bipolar actuation of a Ppy film (adapted from [21])

Therefore, BEC is also an interesting technology to induce motion. These examples show the diversity of possibilities to generate movement on various objects of different size, shape or composition.

I.2.3. Materials Science

BEC represents a powerful technology in materials science too. The electric field gradient allows the synthesis of materials presenting a gradient of composition. Indeed, a conducting object is equipotential in solution, therefore, the interfacial difference of potential evolves along BE. It results in a gradient of overpotential along BE. This characteristic gives access to a continuous evolution of the composition and/or the thickness of the material. Some works have been performed with polymers, such as doping or electrochemically controlled polymerizations [48–50]. Metal depositions forming alloys with a progressive evolution of their composition have also been studied [19,51].

Tisserant *et al.* studied the deposition of three different metals (copper, nickel, zinc) by BEC on gold [51]. First, they performed the deposition of a single metal (Cu, Ni, Zn) and showed

that a higher electric field leads to a deposition over a longer distance. This length also depends on the standard potential of the metal. Noble metals require a lower electric field than non-noble metals to be deposited (Figure 56 a). Afterwards, they deposited bi- and trimetallic alloys (Cu/Zn, Ni/Zn and Cu/Ni/Zn). The resulting materials were analyzed by scanning electron microscope (**SEM**) and energy dispersive X-ray spectroscopy (**EDS**). From the cathodic extremity toward the center of the BE, one can find a trimetallic alloy of Cu/Ni/Zn, then a bimetallic alloy of Cu/Ni and finally only Cu which is in agreement with the standard potential of each metal (Figure 56 b). This work shows the possibility to produce alloys with a composition gradient in one single experiment which is easy to setup. It can be used as a first step to synthesize materials of different chemical composition prior to test them for other purposes (such as electrocatalysis for instance).

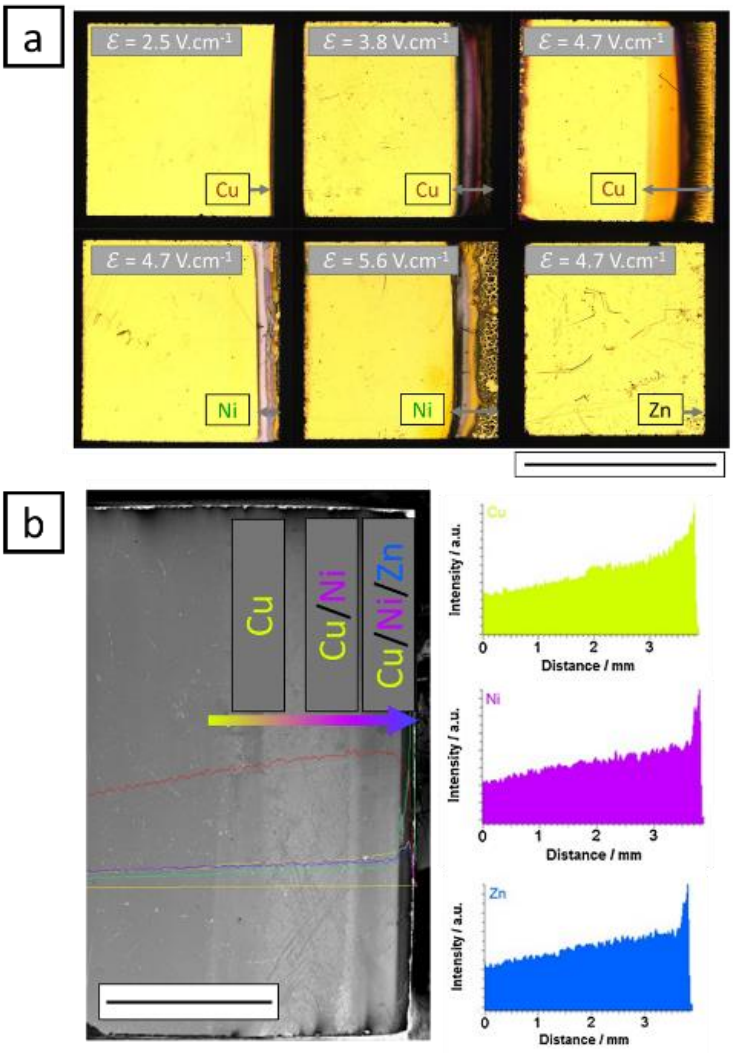

Figure 56: a) Optical micrographs of gold substrates after BEC with different metals and electric fields. Scale bar, 5 mm. b) SEM image and EDS analysis of trimetallic deposition. Scale bar, 2 mm (adapted from [51])

Termebaf *et al.* also showed the possibility of using BEC for the synthesis of metal gradients and to perform a screening of the best composition to catalyze HER [19]. They deposited an alloy of nickel and copper (Figure 57). As for the previous work, they observed an evolution of the composition by analyzing the samples by SEM and EDS. At the cathodic extremity, which is the place where the overpotential is the highest, the deposit contained copper and nickel with a higher proportion of nickel. Going towards the anodic side, the amount of nickel decreased until deposits were only made of copper. Afterwards, the obtained materials were tested for HER. On the cathodic side were the deposits with different proportions of nickel and copper. On this side occurred the reduction of proton. On the anodic side was silver which was dissolved during the experiment. The best Ni-Cu alloy composition corresponded to the longer part of silver dissolution.

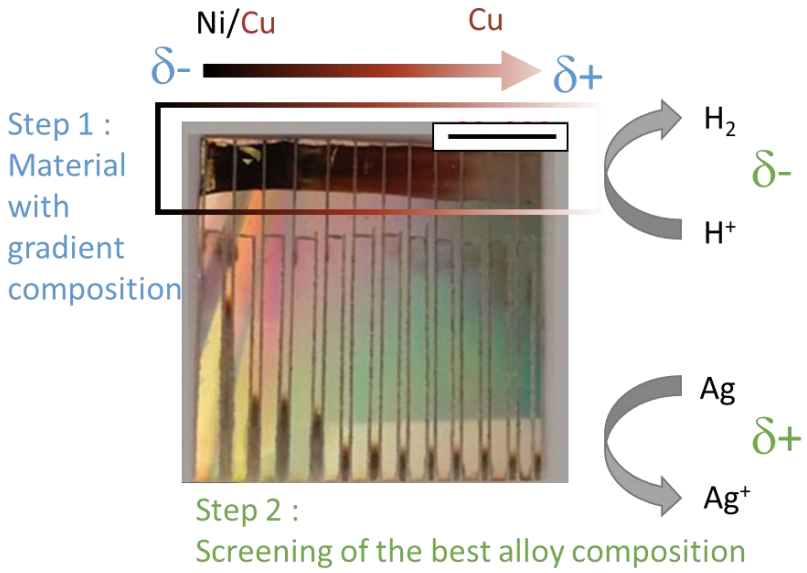

Figure 57: Optical micrograph of an array of BEs after screening. The cathodic sides were composed of composition gradients of a nickel/copper alloy obtained by a first BEC experiment. The anodic side was made out of a sacrificial silver layer. Scale bar, 1 cm (adapted from [19])

Thus, this work has shown the suitability of BEC to be used both to generate a composition gradient and to screen the best catalyst for a selected reaction.

BEC is also interesting to produce Janus Particles (**JP**). Several setups can be used such as capillary electrophoresis or bulk synthesis. The features of BEC also allow the deposition of non-conductive material [40] and the synthesis of ringed particles [52]. Our group developed multiple pathways to break the symmetry of various materials.

More than a decade ago, they used carbon fibers in a BEC setup and modified them at one extremity by generating a gold cluster [53]. In order to modify smaller BEs such as carbon nanotubes, they showed the possibility to adapt a capillary electrophoresis setup. This progress opened the possibility to break the symmetry of smaller BEs (tenth of micrometers of length) which require high electric fields. This method, called capillary-assisted bipolar electrodeposition (**CABED**), has been used afterwards to deposit other metals [54–56] and polymers [57]. It allowed the modification of carbon microtubes with 10 to 30 µm length which required tens of kV. In a later work, Loget *et al.* showed the possibility to modify one extremity of carbon tubes (by copper, gold or nickel) and to modify also both extremities producing dumbbell-like particles [57], either with a symmetrical composition based only on metal deposition, or a dissymmetric configuration, due to the generation of a polymer at the anodic side (Figure 58).

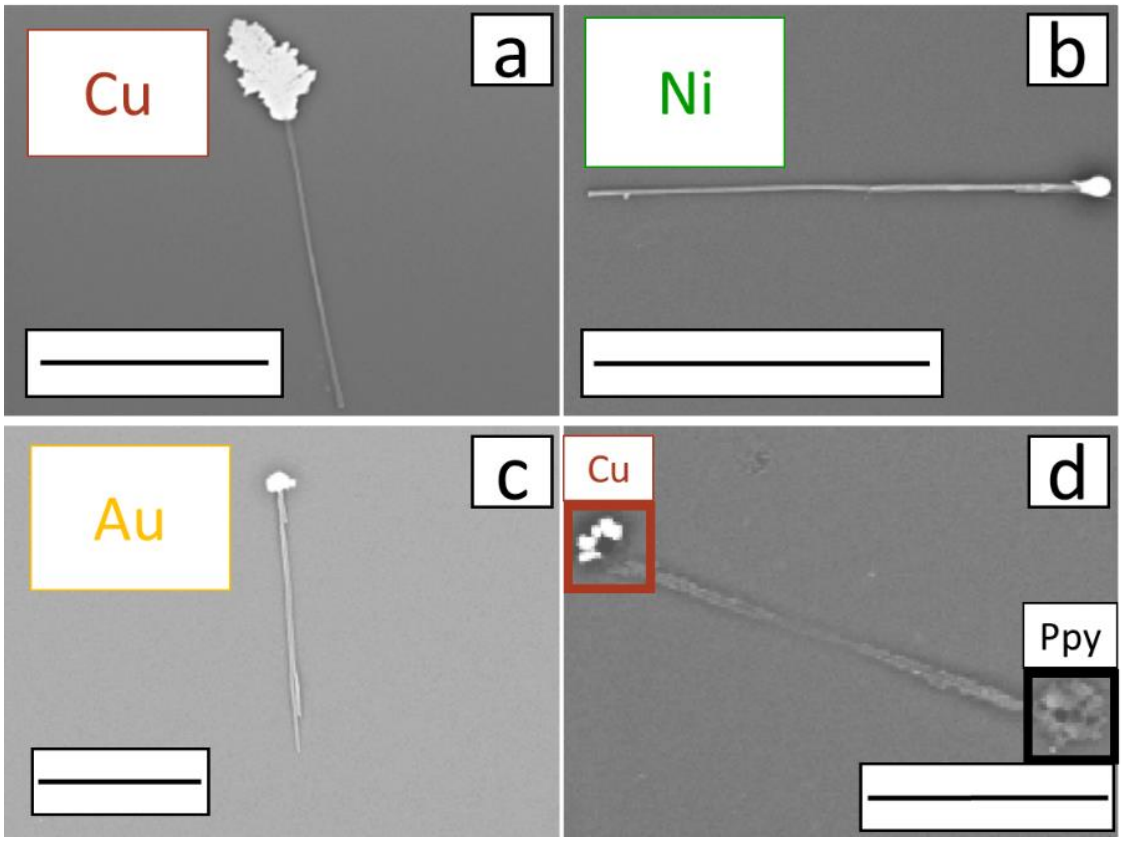

Figure 58: SEM image after asymmetric modification of carbon microtubes with different metals (a-c) and a combination of metal and polymer (d). Scale bar, 20 µm (a, b) and 10 µm (c, d) (adapted from [57])

A few years later, they developed a setup allowing the site-selective modification of carbon tubes and carbon beads in solution [58]. This progress allowed the modification of a large amount of conducting objects in the bulk and thus increased the throughput with respect to the

synthesis of JPs. It also offered the possibility to produce new types of deposits such as ring-shaped layers [52] and non-centered deposition [59] (Figure 59).

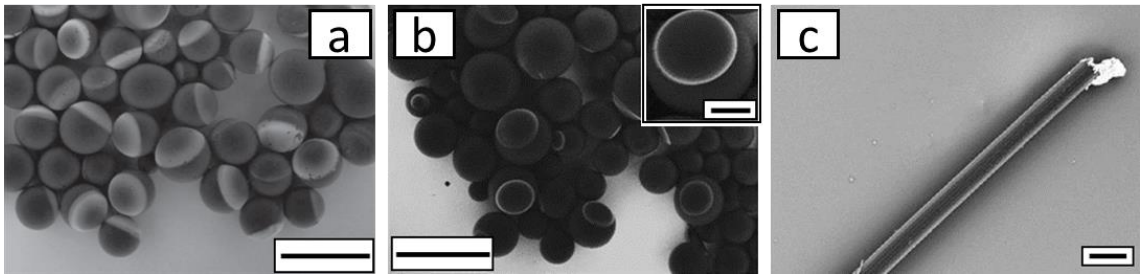

Figure 59: SEM images after asymmetric deposition of a) gold on glassy carbon beads, b) platinum as rings on glassy carbon beads; c) non-centered copper on carbon fibers. Scale bar, 500 µm (a, b), 100 µm (inset of b), 20 µm (c) (Adapted from [58], [52] and [59], respectively)

In these examples, BED has been used to deposit conductive materials (metals or polymers) on BE. Our group proposed also another pathway of modification allowing the deposition of non-conductive materials. As electrochemistry relies on electron transfer, the concept uses the electron transfer to modify the chemical composition of the solution in the vicinity of the electrode, inducing toposelective deposition by precipitation. Indeed, BEC allows the formation of a chemical gradient along the BE, mainly a pH gradient when the electric field induces the electrolysis of water at the extremities of BE. This feature allows indirect bipolar electrodeposition (**IBED**) [23,40]. It was possible to deposit electrophoretic paint (**EP**), silica and titanate using this process (Figure 60).

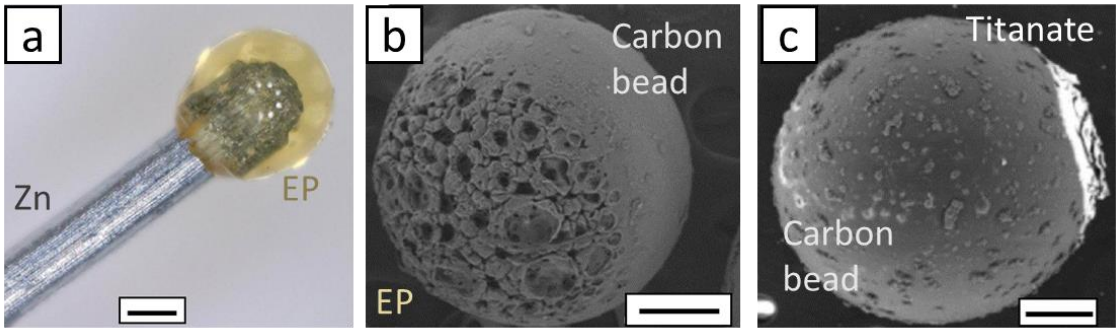

Figure 60: Asymmetric modification by IBED of a) zinc wire with EP, b) carbon particle with EP, c) carbon particle with titanate. Scale bar, 200 µm (adapted from [23] and [40])

So far BEC has been used with BEs which are entirely conductive. In this chapter, we were interested in the asymmetric modification of particles which are composed of a non-conductive core such as glass. Prior to the BEC experiment, this substrate was covered by a

thin layer of nickel. The metal was deposited by an ELD process. The use of ELD should allow us to add initially non-conductive objects to the list of materials that can be asymmetrically modified by BEC. Also, we expect to reduce ΔV_{min} when working with the same redox couple (Ni^{2+}/Ni^{0}) which should give access to the modification of nano-objects.

The next part will be dedicated to our experimental results. The system has been first studied by conventional electrochemistry with a three-electrodes setup. Afterwards, BEC experiments have been performed on Ni-coated glass substrates. Different parameters such as ΔV, size and geometry have been investigated.

II. Results and discussions

II.1. Glass slides

II.1.1. Conventional electrochemistry

Prior to BEC experiments, we have studied the minimum potential difference (ΔV_{min}) required to induce electrochemical reactions at the extremities of the BE. Glass slides were sonicated in KOH for and immersed successively in $SnCl_2$ solution then $PdCl_2$ solution. After these sensitization and activation parts, glass pieces were introduced in an ELD nickel bath. Afterward, to use these pieces in classical electrochemistry, a connection was established with copper tape and the electroactive surface was delimited by Kapton® tape (varying from 0.4 to 0.6 cm²). Scheme 16 summarizes these different steps.

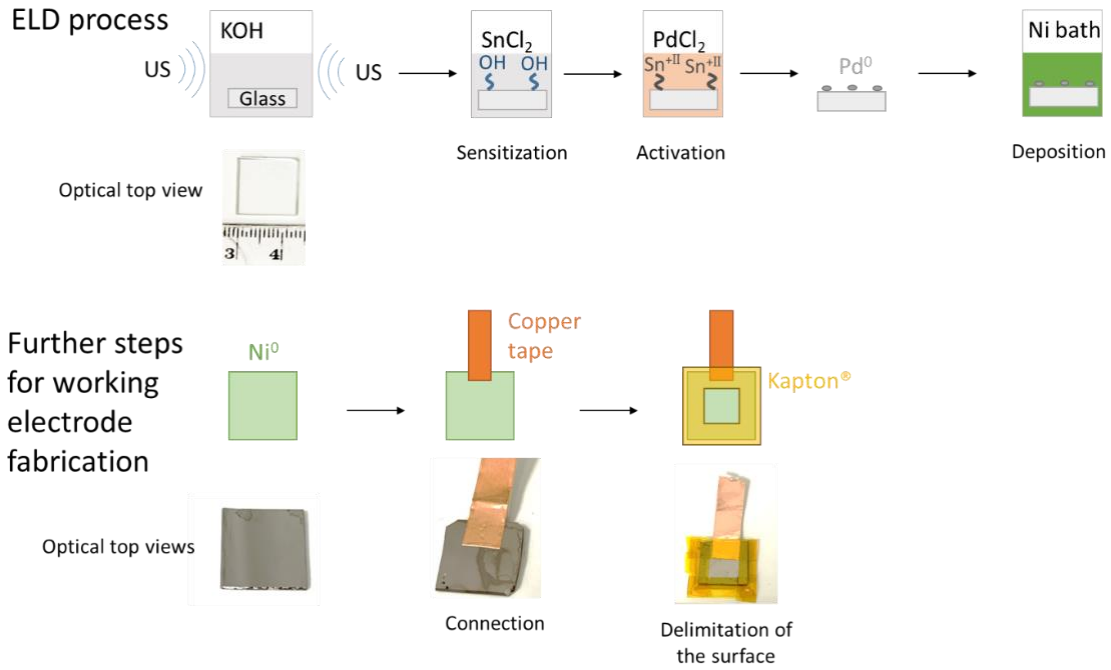

Scheme 16: Successive steps to obtain glass slides covered by nickel used either as WEs for LSV (with copper tape) or as BE (before connection)

These electrodes were used in three different solutions containing either nickel, gold or platinum ions in order to select the most suitable electrolyte for BEC experiments. The electrochemical measurements have been performed by LSV, starting from the open-circuit potential (**OCP**) and scanning towards either reducing or oxidizing potentials. Each experiment was performed with an electrode which had not been used before in order to benefit from the initial surface reactivity of electroless deposited nickel. Moreover, when the potentials are

scanned toward anodic values, the measurement induced the dissolution of the nickel film which made the electrodes unusable afterwards. The reference electrode was Ag/AgCl (3 M NaCl) and a platinum mesh was used as a counter electrode.

The purpose of this study was to determine the best electrolyte to produce JP by BEC. Firstly, we studied the electrochemical behavior of the solution containing nickel ions (Figure 61). The black lines correspond to the LSV performed in supporting electrolyte. The green lines are related to the LSV performed in presence of nickel ions.

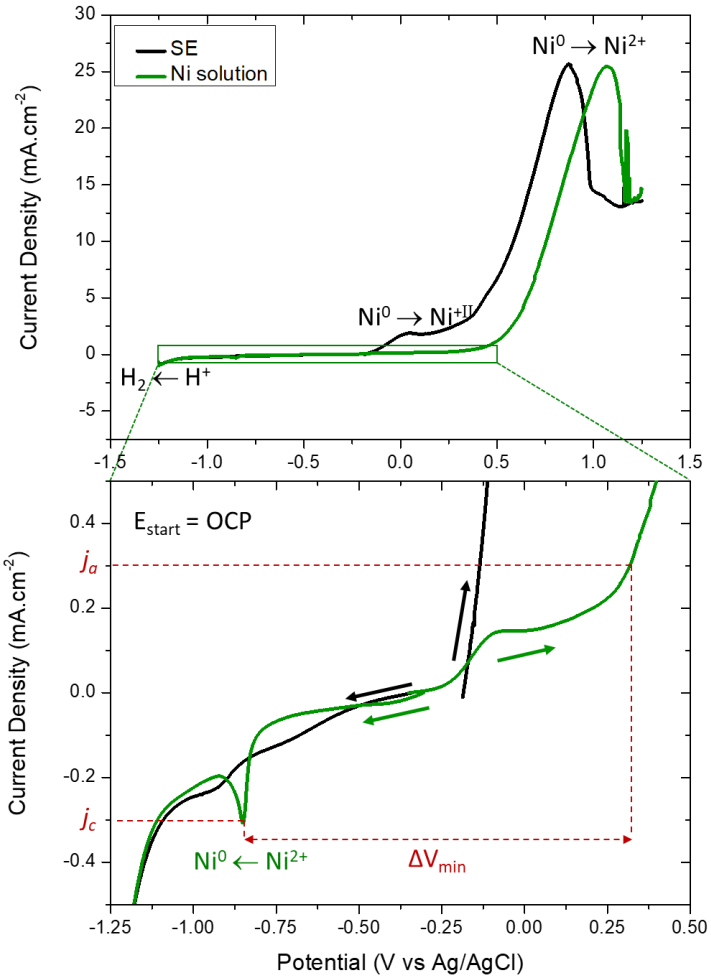

Figure 61: LSV in 0.1 M NaCl, pH = 2.5 (black lines) and in 1 mM $NiCl_2 \cdot 6H_2O$, 0.1 M NaCl, pH = 2.5 (green lines), WE = Ni-coated glass, scan rate = 10 $mV \cdot s^{-1}$

The LSV in SE (black lines) shows a reduction starting at -1.25 V vs Ag/AgCl corresponding to the reduction of protons. On the anodic part, there is an increase of the current density at 0.0 V vs Ag/AgCl related to the oxidation of nickel (either into nickel oxide, nickel hydroxide or nickel complex). At higher potentials, a huge increase in current density is

observed, followed by a drop of the current around 0.8 V vs Ag/AgCl which is related to the oxidative dissolution of the nickel.

The LSVs in the nickel solution are slightly different from the ones obtained in SE. On the reduction side, it is necessary to zoom in to be able to see the reduction of Ni^{2+} ions at E_c = - 0.85 V vs Ag/AgCl ($j_c = - 3 \cdot 10^{-4}$ A·cm^{-2}). This fact reveals that the deposition of nickel from this solution on this substrate is not favored. Thinking about BEC experiment, such a low current density is a drawback in the sense that ΔV_{min} will increase rapidly after the beginning of the experiment since the reduction reaction will move from the reduction of Ni^{2+} ions toward the reduction of protons. Moreover, this latter reduction produces dihydrogen and the bubbles can damage the metallic film. Therefore, it is important to avoid bubble production. In the meantime, on the anodic part, the current related to the formation of Ni^{+II} decreased. Regarding the dissolution of nickel, it requires a more positive potential (around 1.1 V vs Ag/AgCl), thus it appeared to be more difficult to oxidize the metallic layer in a solution containing nickel ions. In order to ensure equal current densities for the anodic and cathodic process ($j_a = - jc = 3 \cdot 10^{-4}$ A·cm^{-2}), E_a has to be + 0.32 V vs Ag/AgCl. Thus, in the initial state, $\Delta V_{min}^{Ni} = |E_a - E_c|$ = 1.17 V, having in mind that the cathodic potential will move quickly toward more negative potential after the start of the BEC experiment due to a fast consumption of nickel ions.

These experiments allow a better understanding of the behavior of this nickel solution on a nickel-coated glass substrate. The oxidative dissolution of nickel requires a high overpotential. Moreover, the low current density related to the reduction of nickel might lead to the reduction of protons shortly after the start of the experiment. The use of nickel was motivated by the expectation of having a small ΔV_{min} allowing us to reduce the size of BEs without applying a huge electric field for nano-objects. In the framework of BEC, these features encouraged us to study two other systems to select the most suitable conditions to perform BEC.

After the study of the nickel solution, electrochemical measurements have been performed with a solution containing gold ions. Since this metal is more noble than nickel, its deposition should occur at a less negative potential compared to nickel. Figure 62 shows the LSVs recorded in an electrolyte containing gold ions (the black lines represent the LSVs in SE). As expected, the reduction potential of gold is lower than the potential observed with nickel. The reaction occurs at E_c = - 0.63 V vs Ag/AgCl ($j_c = - 3.6 \cdot 10^{-4}$ A·cm^{-2}). However, as previously, the reduction of gold does not appear as a major reaction since the current density related to this transformation is low. Regarding the oxidation behavior, the current density

related to the formation of Ni^{+II} and the dissolution of nickel are much lower compared to the experiments carried out in SE. As gold is a more noble metal than nickel, its precursor salt might react spontaneously to oxidize the WE. We can assume that there is a competition between a chemical and an electrochemical oxidation of the nickel layer explaining why the current density related to the oxidation is lower in gold solution compared to the one in SE.

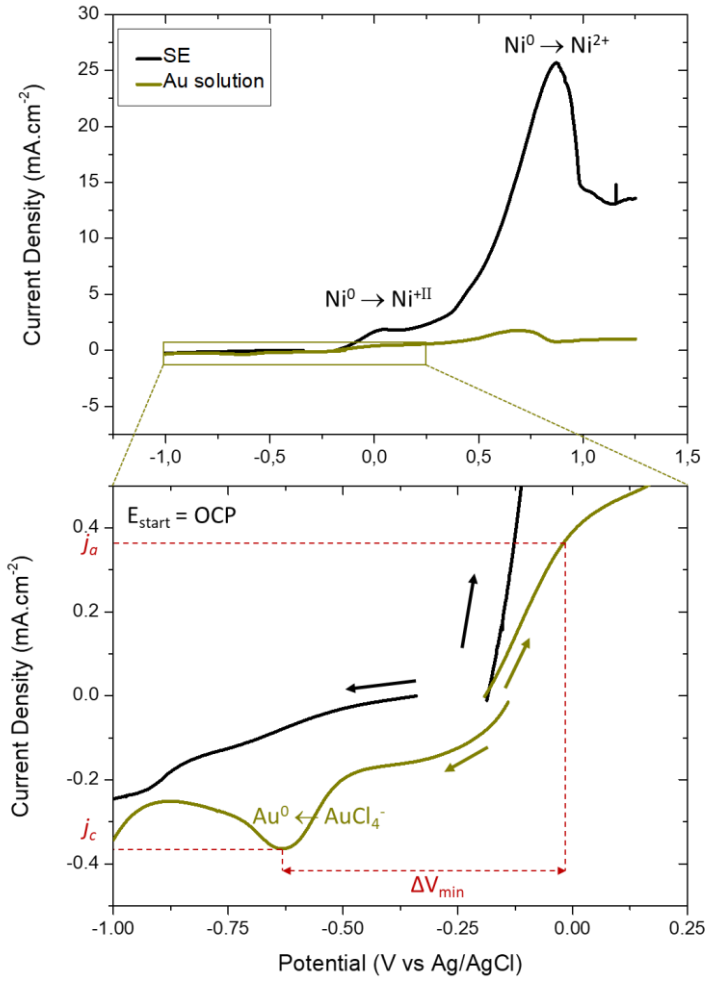

Figure 62: LSV 0.1 M NaCl, pH = 2.5 (black lines) and in 1 mM $HAuCl_4 \cdot 3H_2O$, 0.1 M NaCl, pH = 2.5 (dark yellow lines), WE = Ni-coated glass, scan rate = 10 $mV \cdot s^{-1}$

A balance in current densities ($j_a = - j_c = 3.6 \cdot 10^{-4}$ $A \cdot cm^{-2}$) is obtained for E_a = -0.01 V vs Ag/AgCl which leads to ΔV_{min}^{Au} = 0.62 V. Such a potential difference is interesting to perform BEC experiments on small objects. However, the low current density related to gold reduction is not suitable since only small amounts of gold will be deposited. Consequently, either nothing happens if the electric field is too small, or dihydrogen production occurs, which can damage the metallic layer deposited on glass.

Finally, we studied the electrochemical behavior of a solution containing platinum ions (Figure 63). In the reduction part of the voltammogram, two reduction steps appear at -0.55 V and -0.80 V vs Ag/AgCl with a higher current density than the ones observed for the two former systems. A chronoamperometry was performed at -0.55 V during one hour. EDS measurements with the resulting electrode reveal the presence of platinum (Figure 64Figure 63). The presence of these two peaks can be explained by two hypotheses:

- The first peak corresponds to the formation of an alloy of Ni_xPt_y at -0.55 V vs Ag/AgCl which could be confirmed by X-ray diffraction (**XRD**) measurements, and the second peak is related to the deposition of platinum only.
- The second explanation is that at – 0.55 V, platinum is deposited on nickel and, at -0.8 V, the deposited platinum is reacting with the solution.

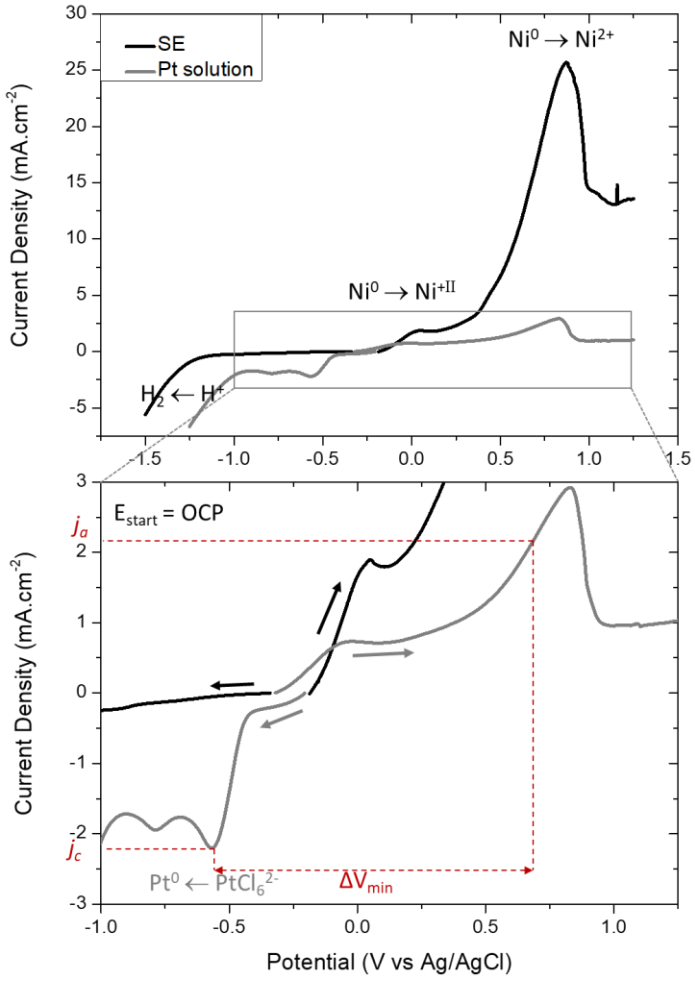

Figure 63: LSV in 0.1 M NaCl, pH = 2.5 (black lines) and in 1 mM $H_2PtCl_6 \cdot xH_2O$, 0.1 M NaCl, pH = 2.5 (grey lines), WE = Ni-coated glass, scan rate = 10 $mV \cdot s^{-1}$

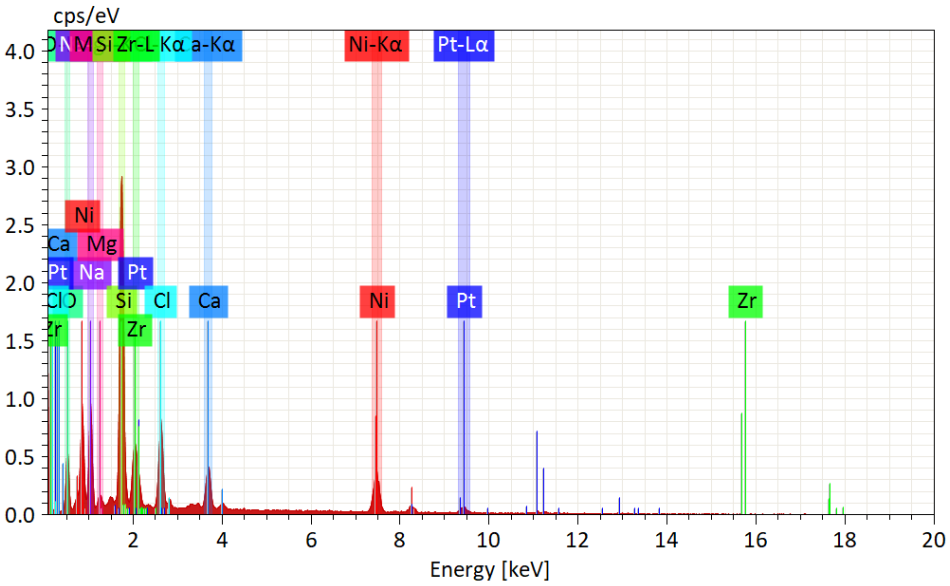

Figure 64: EDS spectrum after a chronoamperometry at -0.55 V vs Ag/AgCl (Q/A = 0.80 C·cm^{-2}) with a solution containing platinum ions (0.1 M NaCl, 1 mM $H_2PtCl_6 \cdot xH_2O$, pH = 2.5)

It can also be noticed that, proton reduction occurs at less negative potential (-1.0 V vs Ag/AgCl) compared to the reduction in SE (-1.25 V vs Ag/AgCl). This observation is an additional indication that platinum was effectively deposited during the reduction sweep since platinum catalyzes the reduction of protons.

Regarding the anodic side, we can notice a similar voltammogram with the platinum solution compared to the gold electrolyte. Like gold, platinum is a more noble metal than nickel. Spontaneous oxidation of nickel might occur and thus be in competition with electrochemical oxidation which can explain the lower current density observed in a platinum solution compared to the current density recorded in SE only.

However, control experiments were performed in order to study this hypothesis. Slides covered by nickel were immersed, without any applied potential, in a solution containing platinum ions for 20 minutes and 1 hour. The substrates were analyzed by SEM and EDS (Figure 65). The analyses did not reveal the presence of platinum on the surface of the substrate. Thus, it seems that the reaction between Ni^0 and $PtCl_6^{2-}$ does not take place or only in a minor proportion undetectable by SEM and EDS.

Another possibility which could explain this difference of current density is a mechanism involving an electrochemical reaction follow by a chemical reaction, namely, the oxidation of Ni^0 to Ni^{+II} (as an oxide, hydroxide or a complex form) by electrochemistry

followed by a chemical reaction between this obtained species and $PtCl_6^{2-}$. Even though this pathway is thermodynamically less favorable than a direct reaction involving Ni^0 and $PtCl_6^{2-}$, kinetic considerations might explain this behavior.

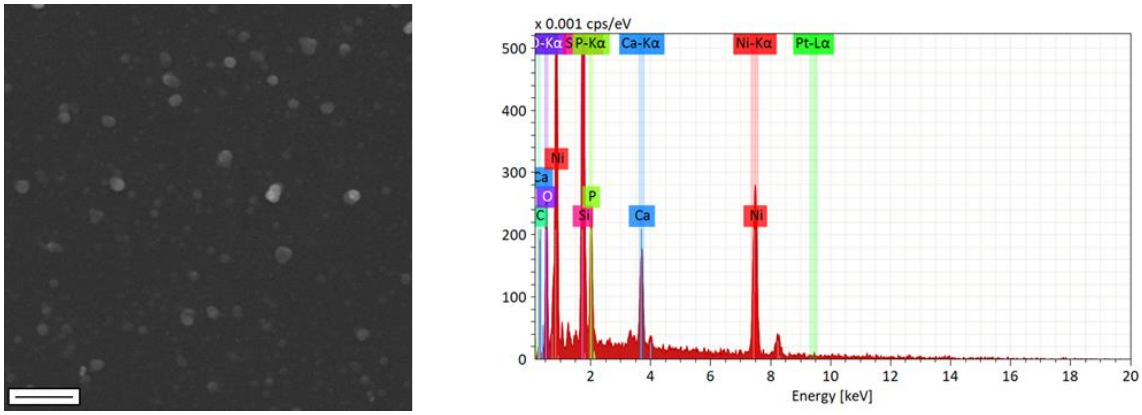

Figure 65: SEM image and EDS spectrum of Ni-coated glass after 1 hour in platinum solution without any applied potential (control experiment). Scale bar, 2 µm.

To determine ΔV_{min}, we considered the reduction occurring at E_c = - 0.55 V vs Ag/AgCl (j_c = - 2.2 · 10^{-3} A·cm^{-2}); thus, to ensure equal current densities for both process (j_a = - j_c = 2.2 · 10^{-3} A·cm^{-2}), E_a has to be + 0.70 V vs Ag/AgCl, leading to ΔV_{min}^{Pt} = 1.25 V. This potential difference is higher compared to the previous systems. However, as the current density related to the deposition of platinum is ten times higher, we decided to work with these redox reactions.

In conclusion, we have studied three electrolytes by LSV containing either nickel, gold or platinum ions in order to select the system having the best features to perform BEC, namely the smallest ΔV_{min} and the most substantial amount of deposit (the highest current density). Unfortunately, there is no system combining both of these features. Indeed, the electrolyte containing gold ions provides the smallest ΔV_{min}, but a too low current density for the reduction of gold, whereas the platinum solution provides the most pronounced deposition of metal, but a high ΔV_{min} is required to induce the redox reactions by BEC. For the following experiments, we decided to select the platinum electrolyte due to the possibility of depositing more metal. Nevertheless, a more detailed study of the solution composition might lead to a more adapted electrolyte.

II.1.2. From conventional to bipolar electrochemistry

Previously, we used a system with three electrodes (working, reference and counter electrodes) to record the LSV experiments. In this section, the experiments were performed in a BEC setup, which means that there is no more reference electrode and the working and counter electrodes are replaced by two feeder electrodes (platinum mesh). The BE, positioned in between the feeder electrodes, was a nickel-covered glass slide obtained by ELD (as shown in Scheme 16). BEC was used to induce an asymmetry on the BE by depositing Pt on the cathodic side and oxidizing the nickel on the anodic side (Scheme 17).

From the last experiments, we could determine ΔV_{min}^{Pt} = 1.25 V. However, this value is underestimated due to the potential drop at the feeder electrodes and the solution resistance. That is why we varied the imposed potential (E_{imp}), and thus the electric field ($\mathcal{E}$) and the potential difference at the extremities of BE (ΔV) (Eq. 20) in order to determine the optimum value which leads to deposition of platinum on one side and dissolution of nickel on the other side. Each experiment was carried on a new BE. As the length of the BEs varies slightly from one BE to another, the electric field was also impacted. For more clarity, the discussion will be based on the values of the potential difference, ΔV. The ΔV was varied from 1.5 V to 12 V.

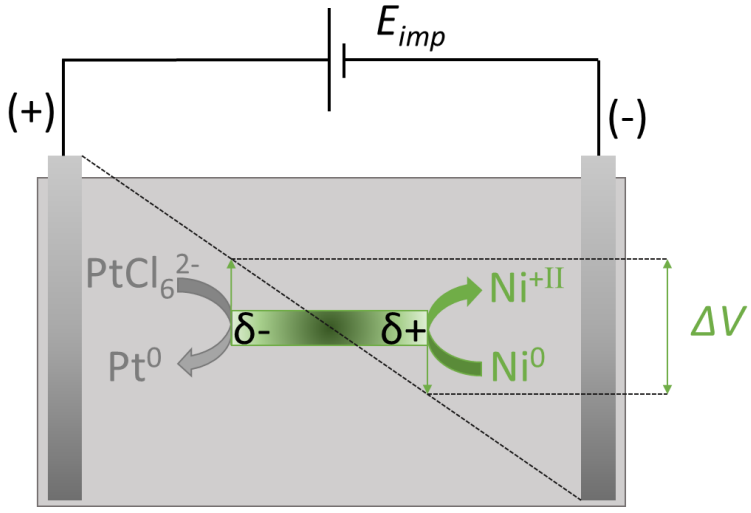

Scheme 17: Representation of BEC experiment

Figure 66 gathers SEM images with corresponding EDS spectra of the cathodic side of the BEs for each ΔV. These observations were made at a constant distance from the cathodic extremity. On this side, we expected the deposition of platinum. At the lowest values, ΔV = 1.5

V and ΔV = 3 V, the EDS spectra already show the presence of platinum. Moreover, the SEM images show small grains homogeneously distributed on the substrate. At higher *ΔV* (6 and 12 V), we expected to detect a higher amount of platinum, but the amount of deposited metal appeared to be in the same order of magnitude on the EDS spectra. Nevertheless, one can notice some differences on the SEM images. At 6 V, the particles have rather a homogeneous size whereas at 12 V, in addition to small particles (which are bigger than the ones observed for the sample at 6 V), we can observe some clusters, probably resulting from coalescence of small particles. This observation is common when a high overpotential is applied to deposit a metal on a substrate and the affinity between both materials is low [60,61].

Figure 67 shows SEM images and EDS spectra of the anodic side of the BEs for each *ΔV*. These observations were made at a constant distance from the anodic extremity. On this side we expected to see the dissolution of nickel. At the lowest value (ΔV = 1.5 V), we observed that the nickel film is still on the glass slide. Likely, nickel oxide or nickel hydroxide was formed during the experiment. An increase to ΔV = 3 V allowed a homogeneous dissolution of the metallic film since no nickel was detected by the EDS analysis. At ΔV = 6 V, platinum started to be deposited on the anodic side and a further increase until 12 V led to a more important deposition. The SEM images show small particles on the nickel film (for 6 V) and a rather homogeneous and covering film with clusters (for 12 V). The EDS spectra indicate that these observations are associated with the increase of the amount of platinum. Such results are surprising since platinum is not supposed to be deposited on this side and nickel should be dissolved, making the slide insulating.

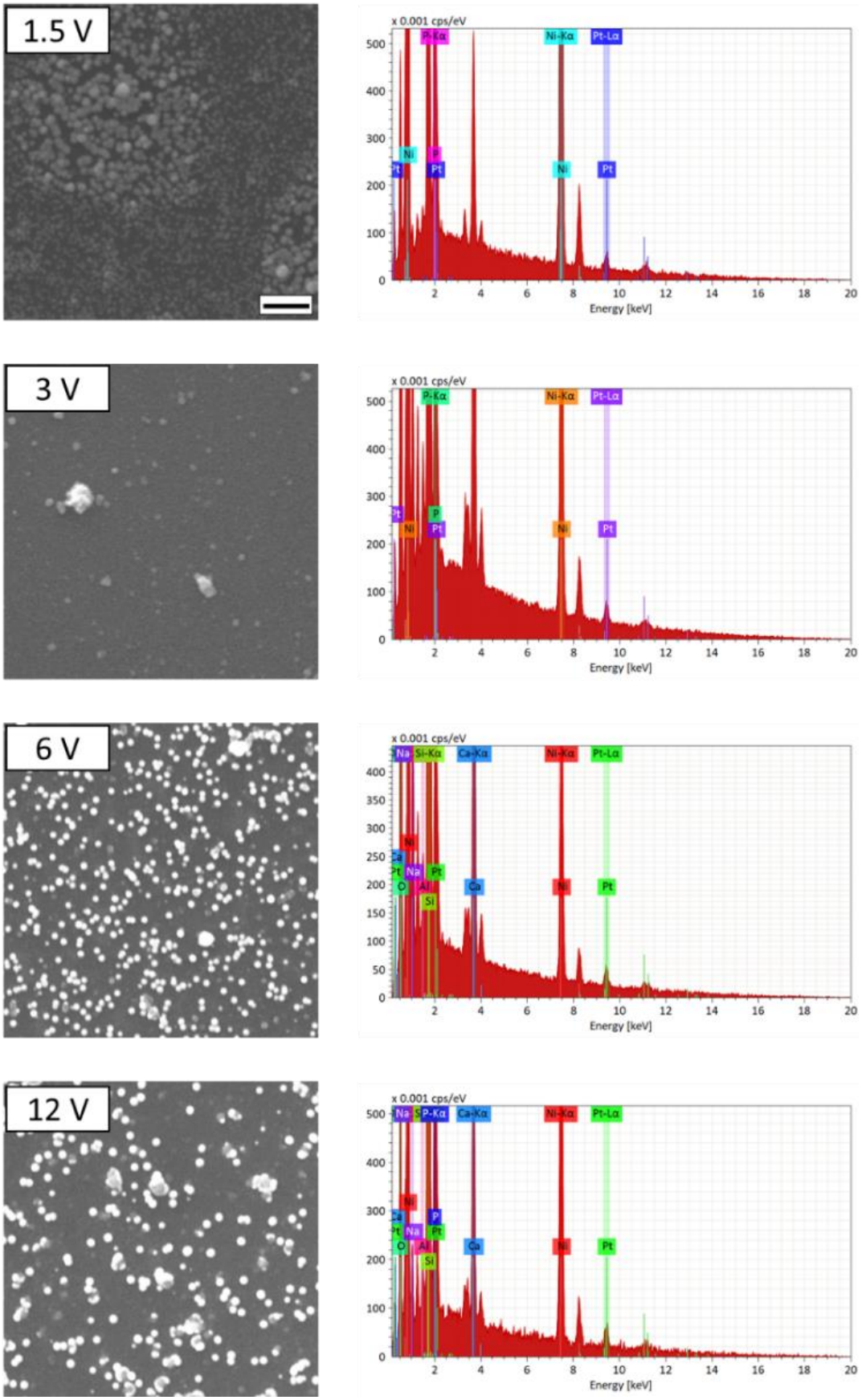

Figure 66: SEM Images (Scale bar, 2 µm) and EDS spectra of cathodic side of Ni-coated glasses at different ΔV.

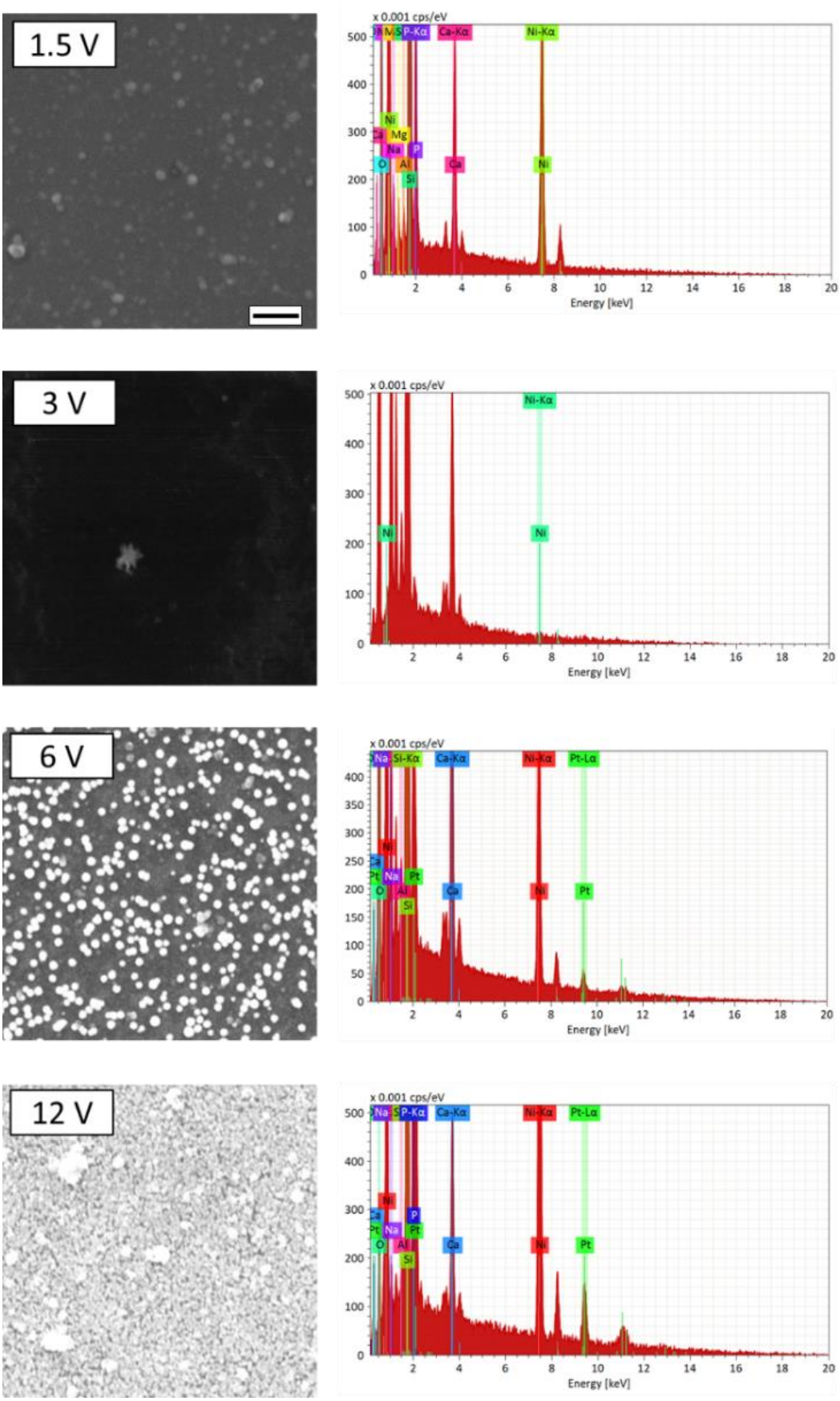

Figure 67: SEM Images (Scale bar, 2 µm) and EDS spectra of the anodic side of Ni-coated glasses at different ΔV

If we compare the anodic and the cathodic side of the BE obtained at ΔV = 12 V, we can clearly see that more platinum is deposited on the anodic side, which is counterintuitive as an oxidation should occur on this side. Figure 68 shows the anodic part of a glass slide with a lower magnification, obtained after the BEC experiment. A large area of platinum is observed (brighter part). As mentioned previously, control experiments showed that no spontaneous deposition of platinum occurs as we could expect from thermodynamic considerations (Figure 65).

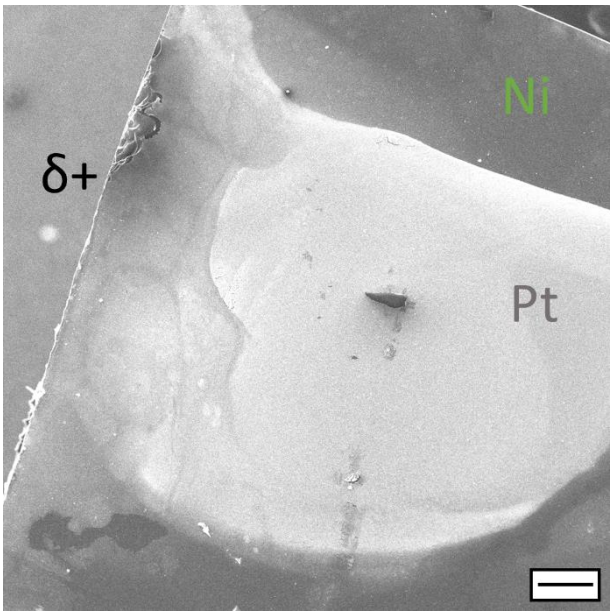

Figure 68 : SEM image at low magnification of the anodic part of Ni-coated glass after BEC experiment at 12 V. Scale bar, 250 µm.

From these two observations, it is difficult to be confident about the explanation of this result but, as proposed for the LSV experiments, we assume that platinum can be deposited by an electrochemical/chemical mechanism. By BEC, Ni^0 is oxidized to Ni^{+II}, which can reduce the platinum anions to Pt^0. This pathway appears to be thermodynamically less favorable than a direct reaction between $PtCl_6^{2-}$ and Ni^0, however, we did not observe deposition in the control experiment. It might be explained by kinetic considerations. Further experiments should be performed to confirm this hypothesis.

These experiments showed the possibility to deposit platinum on the cathodic side at any potential difference from 1.5 V to 12 V. On the anodic side, at 3 V, nickel is dissolved. Below this value, nickel is still present at the surface of the BE. Both experiments provide a dissymmetric object which is one of the purpose of this chapter. Above this *ΔV*, platinum is mainly present on the anodic side, probably due to an electrochemical/chemical pathway. In the

following, the procedure combining ELD and BEC has been applied to spherical glass substrates.

II.2. Spheres

II.2.1. Bipolar electrochemistry

The study on glass slides allowed us to select a range of ΔV to apply for the deposition of platinum and the dissolution of nickel (between 1.5 and 3 V). We are now interested in another geometry, and therefore we applied the BEC approach to commercial glass spheres of 1 mm diameter. The spheres were covered by a nickel film with the same procedure used for the slides.

In order to check the presence of platinum, EDS analysis was performed. As the slides were much larger than the beads, we could clearly distinguish the anodic and cathodic poles and perform selective EDS measurements on each side. In the case of the beads it was not possible from an experimental point of view. Nevertheless, the size of the beads was small enough to fit completely inside an analyzable region of interest, that is why, we performed EDS mapping to highlight where the different elements were present. We show the result for nickel, platinum, and silicon elements. It is noteworthy that due to the geometry and the size of the beads, not the total surface could be examined.

Figure 69 shows the SEM image of a bead obtained after BEC with $\Delta V = 1.5$ V. The probed area is highlighted by the dotted red line. The SEM image reveals a homogeneous surface with a brighter area on the right side in comparison with the rest of the bead, which could be related to the deposition of platinum and thus, the cathodic side of the BE.

The mapping of nickel shows a homogeneous distribution of the element on the probed surface, which highlights that no dissolution occurred at $\Delta V = 1.5$ V. Regarding the platinum, the mapping reveals its presence on the right side of the bead, which confirms the observation made by SEM. The mapping of silicon is rather homogeneous with a weaker part on the right side. The analysis gives us two types of information: first, the nickel layer is thin enough (less than 1 µm) to be able to detect silicon which correspond to the glass bead. Second, the weaker signal indicates that, in this area, there is a thicker layer lowering the signal related to the silicon. This observation is consistent with the deposition of platinum.

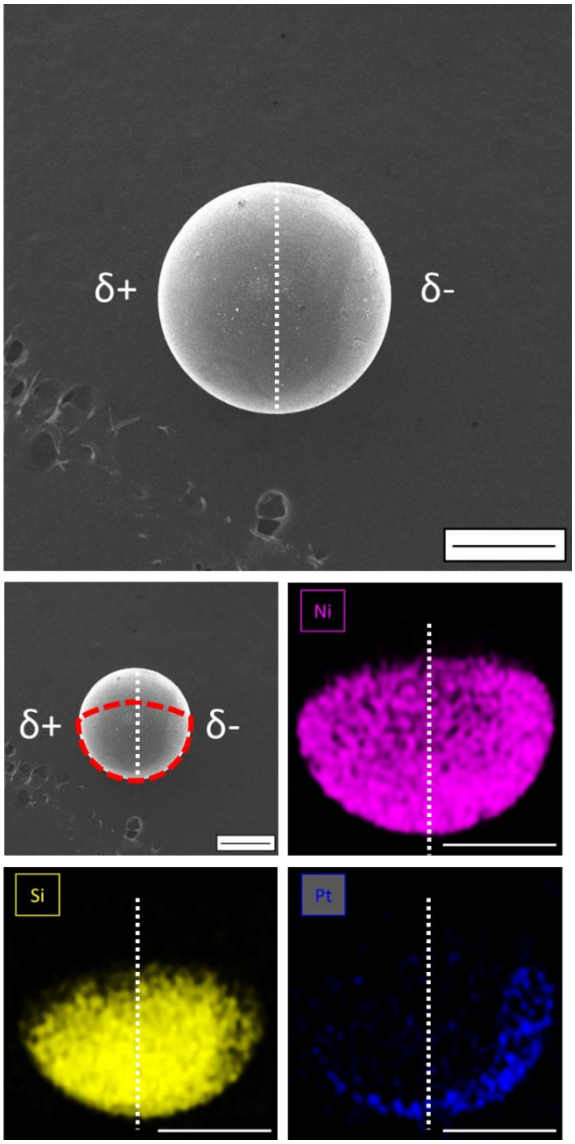

Figure 69: SEM image and EDS mapping of Ni-coated glass bead after the BEC experiment at 1.5 V. Scale bar, 500 µm

These observations indicate similar behaviors at ΔV = 1.5 V for planar and spherical geometries, namely no dissolution of nickel on the anodic side and platinum deposition on the cathodic side. In order to check the evolution of this behavior as a function of electrochemical driving force, we increased in a next experiment the potential difference to 3 V (Figure 70).

The SEM image shows a difference in contrast at the bottom of the bead. As previously, EDS mapping has been performed to analyze the distribution of nickel, platinum and silicon (area highlighted in dotted red line).

The mapping of nickel reveals the presence of this element at the bottom of the bead and a weaker signal when going towards the center of the BE. For platinum, the emission is strong at the bottom of the bead and not existing everywhere else. The signal related to silicon

is weak at the bottom of the bead and strong at other positions. This mapping is consistent with the analysis of nickel and platinum. These mappings allow us to conclude that with ΔV = 3 V, it is possible to dissolve the nickel on the anodic side while depositing platinum on the cathodic side.

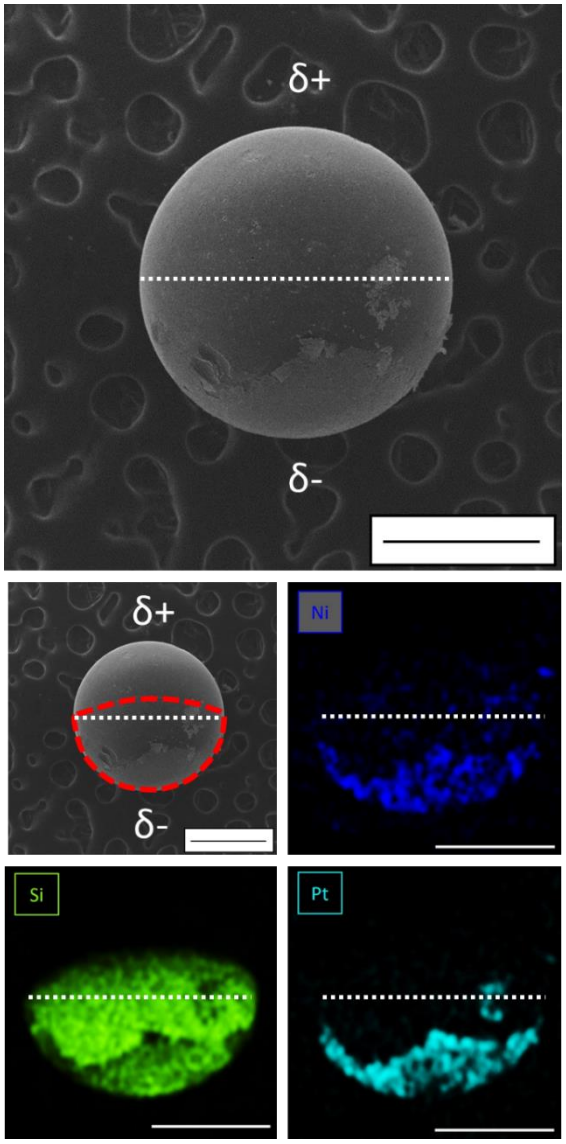

Figure 70: SEM image and EDS mapping of Ni-coated glass bead after BEC experiment at 3 V. Scale bar, 500 µm

In summary, we were able to deposit platinum by BEC on a spherical core-shell structure. The behavior of the beads is comparable to the one observed with the glass slides despite a change in geometry. Indeed, we noticed a deposition of platinum at 1.5 V and 3V on the cathodic side. Regarding the anodic side, at ΔV = 1.5 V, there is no dissolution of nickel whereas the metallic layer was dissolved at 3 V.

As we are interested to induce an asymmetry at the micro- and nanoscale, we decided to move in the next step towards even smaller objects and worked with glass beads of *ca.* 250 µm diameter and silica beads of 1 µm diameter.

II.2.2. Decrease in scale

The previously used procedure for nickel deposition has been adapted to smaller objects, such as commercial glass beads with a diameter of *ca.* 250 µm.

Figure 71 shows the SEM image and EDS analysis of glass beads after ELD. We can observe an inhomogeneous topology. The EDS spectrum reveals the presence of nickel and the mapping allows the correlation between the inhomogeneous surface and a non-uniform deposition of nickel. This observation could be explained by mechanical impacts between the beads after the deposition.

Some improvements are still necessary to reach a homogeneous nickel coverage. However, we can already notice the polydispersity of the sample. This characteristic will be an issue when applying BEC, since the driving force generated at the poles of a particle is highly dependent on its diameter. To overcome this problem, we tried to perform ELD on silica beads synthesized in the laboratory.

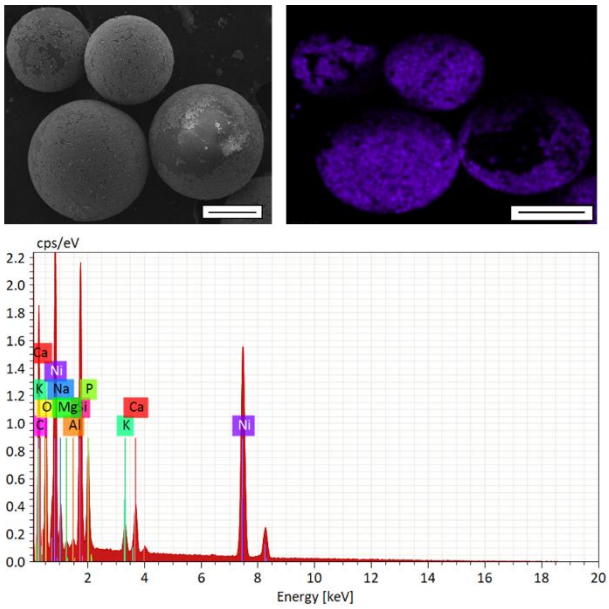

Figure 71: SEM image and EDS analysis of glass beads of 250 µm diameter after ELD. Scale bar, 100 µm.

Silica beads were synthesized by using the Stöber process, which consists in hydrolyzing alkyl silicates followed by condensation of silicic acid [62]. This process allows the synthesis of monodisperse silica beads of 1 µm diameter as shown in Figure 72 and which is of primary importance to use these objects for BEC experiments.

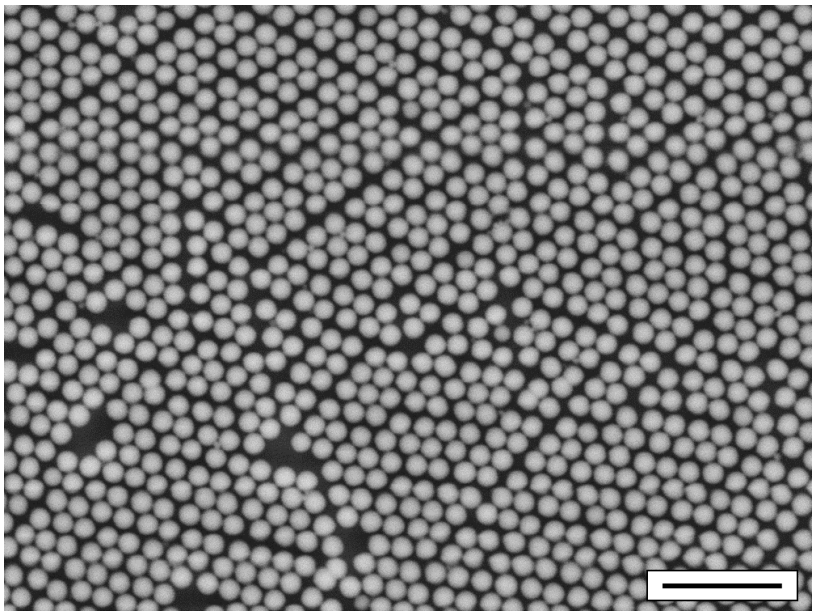

Figure 72: SEM image of silica beads obtained by the Stöber process. Scale bar, 5 µm

Two challenges are present here. The first is the decrease the size of the beads. We already noticed some difficulties with the previous experiments, such as an inhomogeneous coverage of the beads. The second challenge is the change of material. Indeed, until now, we used glass substrates which are mainly made of silicon oxide, but calcium, potassium, aluminum, magnesium, sodium oxides are also present. In this part, the objects were only made out of silicon oxide.

From an experimental point of view, a decrease of size generates some difficulties. Previously, the objects were big enough to be seen during the different steps of the process. In the case of the silica beads, they are too small to be seen, even after centrifugation. Thus, at each change of solution (from sensitization to activation and immersion in the nickel bath) there is a risk to lose some beads.

In order to improve the SEM observations, drops of a suspension containing the beads were deposited on a gold-coated glass substrate in order to ensure a good electrical contact and avoid electric charging phenomena. It was usually hard to find the silica beads, indicating that only a small part of the initial amount of beads remained after the ELD procedure.

Figure 73 shows a SEM image and an EDS spectrum of an isolated silica bead after the ELD process. Based on the EDS analysis, we can clearly see the presence of silicon, however, there is no evidence that nickel deposition occurred.

We can propose several hypotheses to explain the absence of nickel in the EDS analysis:

- The amount of nickel is too low to be detected by the EDS probe. In this case, an increase of the immersion time in the nickel bath should lead to an increase of the thickness of the deposited nickel and thus, should be detectable by EDS.
- Nickel was deposited on the beads but was removed afterwards due to mechanical impacts as we observed for the latter beads. However, in this case, as previously, we would expect to see an inhomogeneous coverage of the beads instead of homogeneous non-covered beads.
- Nickel was not deposited at all on the silica beads.

  The latter effect might be due to an inefficient sensitization. Gao *et al.* developed a different process of sensitization to deposit nickel on silica beads of 240 nm [63], and it could be worth to try it with our system.

  Another explanation could be a too low bath charge. Indeed, in general, an ELD bath requires an optimum charge, which is the ratio of the surface to cover over the volume of ELD bath [$dm^2 \cdot L^{-1}$]. There is a range around this optimal value but if the experiment is carried out with a too low or too high charge, deposition does not occur. In our case, this problem could be overcome by increasing the amount of beads at the beginning of the procedure.

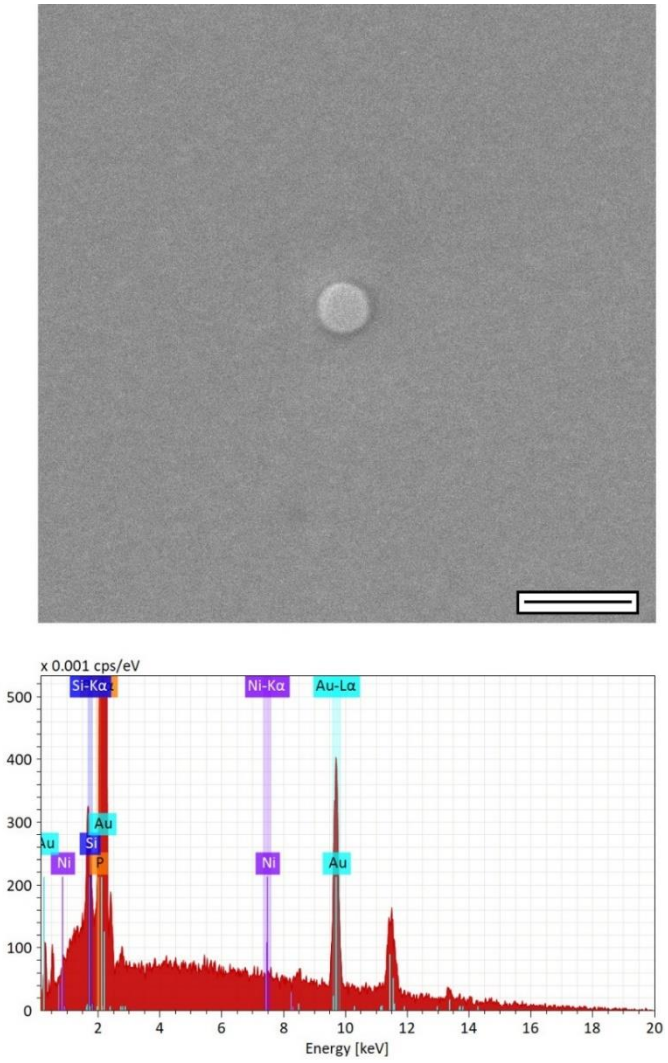

Figure 73: SEM image and EDS spectrum of 1 µm diameter silica bead after ELD. Scale bar 2 µm

To summarize, we were able to perform ELD and BEC experiments on 1 mm diameter commercial glass beads. ELD was performed to deposit a uniform nickel shell. The resulting objects were used as BEs. It was possible to deposit platinum on the cathodic side and to dissolve nickel on the anodic side for $\Delta V = 3$ V. Afterwards, we applied the ELD process to smaller beads. Nickel was deposited on commercial glass beads of *ca.* 250 µm diameter. We observed some inhomogeneity which might be explained by mechanical impacts between the beads. We noticed the polydispersity of these beads which is a drawback for the use of BEC. Then, we synthesized monodisperse silica beads of 1 µm diameter. No nickel has been detected by EDS measurements. The most likely hypothesis would be that no deposition occurred because of a too low amount of objects in the ELD bath and thus a too low bath charge.

III. Conclusion and Perspectives

In conclusion, we used the ELD process to deposit nickel on different types of non-conductive substrates. Glass slides covered by a metallic layer were used as WE in a setup with three electrodes. LSV experiments have been performed and allowed us to study the behavior of this material in three different electrolytes containing either nickel, gold or platinum ions. These experiments helped us to select the best conditions for BEC. An electrolyte containing platinum ions has been selected due to its higher reactivity despite the high ΔV_{min}.

Afterwards, glass objects covered by nickel were used as BE. We studied two different geometries, a planar one based on glass slides, and spherical beads. We saw that platinum deposition occurred at $\Delta V = 1.5$ V on the cathodic side, and that nickel was not dissolved on the anodic side. It might be oxidized towards nickel oxide or hydroxide. An increase of the potential (3 V) allowed nickel dissolution. On the slides, a further increase enables the deposition of platinum even on the anodic side: When the difference of potential was higher than 6 V, we observed a rather homogenous platinum deposition on the whole BE; a potential of 12 V induced a preferential deposition on the anodic side. At this state, it is difficult to conclude on the mechanism which allows the deposition of platinum on the anodic side. Our assumption is an electrochemical oxidation of Ni^0 in an oxide or hydroxide form followed by a chemical reduction of platinum ions, but this hypothesis needs to be validated by complementary experiments.

In parallel, we tried to deposit nickel on smaller objects with the aim of using them in BEC. We were able to deposit inhomogeneous nickel layers on beads of *ca.* 250 µm diameter. These imperfections could be due to mechanical interactions between the beads after deposition. We also tried to transfer this procedure to even smaller objects, the silica beads, which present the advantage of being monodisperse. However, so far the results are not conclusive. Maybe the sensitization of silica beads requires some optimizations, and the procedure should be improved to offer a better control of the amount of silica beads.

These results are only of preliminary nature and the experiments should be continued in order to get a better insight into the most relevant parameters.

Different electrolyte compositions for BEC could be studied by LSV. So far, we did not vary the concentration of metal ions and we did not use any additives. These two parameters

could give access to a more suitable electrolyte for BEC. Platinum has been chosen due to the most efficient deposition on the used substrate. However, the ΔV of this system is still high if we want to decrease the size of BE. Some products could be added to favor the dissolution of nickel (such as complexing ligands) and thus decrease the anodic overpotential. Gold electrolyte has an interesting ΔV, but the amount of deposited gold was not significant. A surface treatment of the BE could be helpful in this case.

The influence of the potential has been studied for the slides, but one could also study the influence of the experimental time for a given potential. For the beads of 1 mm diameter, only two potentials could be tested, and more potential values should be studied prior to applying BEC to the smaller beads. Regarding the glass beads of *ca.* 250 µm diameter, we have evidence that nickel has been deposited, however some efforts need to be done to improve the homogeneity of the deposit by limiting the mechanical collisions. Silica beads of 1 µm diameter seem to be a different case due to the decrease in size, making the experimental procedure more complicated compared to the bigger substrates, and being a material with a different composition compared to the glass used in the previous experiments. A different sensitization process could be used prior to ELD.

There are still some improvements to be done to use this procedure to modify substrates at the micrometer scale and below. The main motivation of this work was to modify silica nanohelices with a homogeneous layer of nickel to induce motion or to perform BEC. The silica beads are the material closest to the helices. So far, the modification was not possible on these objects, however, once this obstacle would be overcome, the transposition to the helices should be rather fast.

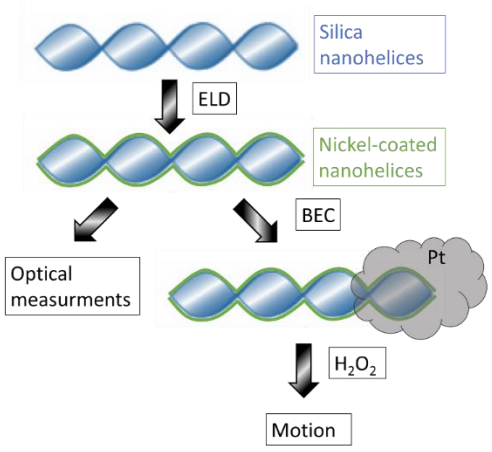

Figure 74: Perspectives of modification of silica nanohelices by ELD followed by BEC experiments

Nevertheless, we reported here the first utilization of BEC on glass substrates covered by nickel. Thanks to the ELD process, it is possible to apply BEC to initially non-conductive materials and thus provide new JPs with diverse functionalities. In our work, we deposited platinum on the substrates. This metal is well-known for the decomposition of hydrogen peroxide to induce motion. Thus, one can imagine to synthesize autonomous swimmers made of a non-conducting core controlled by chemical reactions (Figure 74). As nickel has magnetic properties, these particles can also be controlled by a magnetic field. If gold is deposited on such particles instead of platinum, thiols with fluorescent groups can be adsorbed allowing an easier tracking of the particles. Moreover, the ELD process is also widely used to deposit other metals such as aluminum, copper, silver or gold. Changing the nature of the metallic layer would offer even more possibilities to tune the functionalization of these objects.

IV. References

[1] T. Delclos, C. Aimé, E. Pouget, A. Brizard, I. Huc, M.-H. Delville, R. Oda, *Nano Lett.* **2008**, *8*, 1929.

[2] R. Tamoto, S. Lecomte, S. Si, S. Moldovan, O. Ersen, M.-H. Delville, R. Oda, *J. Phys. Chem. C* **2012**, *116*, 23143.

[3] J. Cheng, G. Le Saux, J. Gao, T. Buffeteau, Y. Battie, P. Barois, V. Ponsinet, M.-H. Delville, O. Ersen, E. Pouget, R. Oda, *ACS Nano* **2017**, *11*, 3806.

[4] A. Ghosh, P. Fischer, *Nano Lett.* **2009**, *9*, 2243.

[5] J. R. Backhurst, J. M. Coulson, F. Goodridge, R. E. Plimley, M. Fleischmann, *J. Electrochem. Soc.* **1969**, *116*, 1600.

[6] D. C. Eardley, D. Handley, S. P. S. Andrew, *Electrochimica Acta* **1973**, *18*, 839.

[7] F. Goodridge, C. J. H. King, A. R. Wright, *Electrochimica Acta* **1977**, *22*, 347.

[8] F. Goodridge, C. J. H. King, A. R. Wright, *Electrochimica Acta* **1977**, *22*, 1087.

[9] M. Fleischmann, J. Ghoroghchian, S. Pons, *J. Phys. Chem.* **1985**, *89*, 5530.

[10] M. Fleischmann, J. Ghoroghchian, D. Rolison, S. Pons, *J. Phys. Chem.* **1986**, *90*, 6392.

[11] K. G. Ellis, R. E. W. Jansson, *J. Appl. Electrochem.* **1981**, *11*, 531.

[12] E. Smotkin, A. J. Bard, A. Campion, M. A. Fox, T. Mallouk, S. E. Webber, J. M. White, *J. Phys. Chem.* **1986**, *90*, 4604.

[13] E. S. Smotkin, S. Cervera-March, A. J. Bard, A. Campion, M. A. Fox, T. Mallouk, S. E. Webber, J. M. White, *J. Phys. Chem.* **1987**, *91*, 6.

[14] J. Duval, J. M. Kleijn, H. P. van Leeuwen, *J. Elecanal. Chem.* **2001**, *505*, 1.

[15] J. F. L. Duval, G. K. Huijs, W. F. Threels, J. Lyklema, H. P. van Leeuwen, *J. Coll. Inter. Sci.* **2003**, *260*, 95.

[16] J. F. L. Duval, J. Buffle, *J. Phys. Chem. B* **2006**, *110*, 6081.

[17] R. M. Crooks, *ChemElectroChem* **2016**, *3*, 357.

[18] K.-F. Chow, F. Mavré, R. M. Crooks, *J. Am. Chem. Soc.* **2008**, *130*, 7544.

[19] H. Termebaf, M. Shayan, A. Kiani, *Langmuir* **2015**, *31*, 13238.

[20] G. Loget, A. Kuhn, *Nat. Commun.* **2011**, *2*, 535.

[21] B. Gupta, B. Goudeau, A. Kuhn, *Angew. Chem. Int. Ed.* **2017**, *56*, 14183.

[22] G. Loget, S. So, R. Hahn, P. Schmuki, *J. Mater. Chem. A* **2014**, *2*, 17740.

[23] Z. A. Fattah, L. Bouffier, A. Kuhn, *Appl. Mater. Today.* **2017**, *9*, 259.

[24] G. Loget, Electric field-generated asymmetric reactivity: From materials science to dynamic systems, Université de Bordeaux, France, **2012**.

[25] C. J. H. King, A. R. Wright, *Electrochimica Acta* **1977**, *22*, 1135.

[26] K. Kusakabe, S. Morooka, Y. Kato, *J. Chem. Eng. Japan / JCEJ* **1982**, *15*, 45.

[27] K. Kusakabe, S. Morooka, Y. Kato, *J. Chem. Eng. Japan / JCEJ* **1986**, *19*, 43.

[28] M. Sudoh, T. Kodera, H. Hino, H. Shimamura, *Journal of Chemical Engineering of Japan* **1988**, *21*, 198.

[29] Ch. Comninellis, E. Plattner, P. Bolomey, *J Appl Electrochem* **1991**, *21*, 415.

[30] D. Plana, G. Shul, M. J. Stephenson, R. A. W. Dryfe, *Electrochem. Commun.* **2009**, *11*, 61.

[31] D. Plana, F. G. E. Jones, R. A. W. Dryfe, *J. Elecanal. Chem.* **2010**, *646*, 107.

[32] J. P. Guerrette, S. M. Oja, B. Zhang, *Anal. Chem.* **2012**, *84*, 1609.

[33] J. T. Cox, J. P. Guerrette, B. Zhang, *Anal. Chem.* **2012**, *84*, 8797.

[34] S. E. Fosdick, R. M. Crooks, *J. Am. Chem. Soc.* **2012**, *134*, 863.

[35] F. Mavré, R. K. Anand, D. R. Laws, K.-F. Chow, B.-Y. Chang, J. A. Crooks, R. M. Crooks, *Anal. Chem.* **2010**, *82*, 8766.

[36] G. Loget, A. Kuhn, *Lab Chip* **2012**, *12*, 1967.

[37] G. Loget, D. Zigah, L. Bouffier, N. Sojic, A. Kuhn, *Acc. Chem. Res.* **2013**, *46*, 2513.

[38] Y. Wang, R. M. Hernandez, D. J. Bartlett, J. M. Bingham, T. R. Kline, A. Sen, T. E. Mallouk, *Langmuir* **2006**, *22*, 10451.

[39] J.-C. Bradley, H.-M. Chen, J. Crawford, J. Eckert, K. Ernazarova, T. Kurzeja, M. Lin, M. McGee, W. Nadler, S. G. Stephens, *Nature* **1997**, *389*, 268.

[40] G. Loget, J. Roche, E. Gianessi, L. Bouffier, A. Kuhn, *J. Am. Chem. Soc.* **2012**, *134*, 20033.

[41] A. Arora, J. C. T. Eijkel, W. E. Morf, A. Manz, *Anal. Chem.* **2001**, *73*, 3282.

[42] W. Zhan, J. Alvarez, R. M. Crooks, *J. Am. Chem. Soc.* **2002**, *124*, 13265.

[43] K.-F. Chow, F. Mavré, J. A. Crooks, B.-Y. Chang, R. M. Crooks, *J. Am. Chem. Soc.* **2009**, *131*, 8364.

[44] F. Mavré, K.-F. Chow, E. Sheridan, B.-Y. Chang, J. A. Crooks, R. M. Crooks, *Anal. Chem.* **2009**, *81*, 6218.

[45] S. E. Fosdick, S. P. Berglund, C. B. Mullins, R. M. Crooks, *ACS Catal.* **2014**, *4*, 1332.

[46] G. Loget, A. Kuhn, *J. Am. Chem. Soc.* **2010**, *132*, 15918.

[47] B. Gupta, B. Goudeau, P. Garrigue, A. Kuhn, *Adv. Funct. Mater.* **2018**, *28*, 1705825 (1 to 6).

[48] S. Inagi, *Polymer J.* **2016**, *48*, 39.

[49] Y. Ishiguro, S. Inagi, T. Fuchigami, *Langmuir* **2011**, *27*, 7158.

[50] N. Shida, Y. Koizumi, H. Nishiyama, I. Tomita, S. Inagi, *Angew. Chem. Int. Ed.* **2015**, *54*, 3922.

[51] G. Tisserant, Z. Fattah, C. Ayela, J. Roche, B. Plano, D. Zigah, B. Goudeau, A. Kuhn, L. Bouffier, *Electrochimica Acta* **2015**, *179*, 276.

[52] J. Roche, G. Loget, D. Zigah, Z. Fattah, B. Goudeau, S. Arbault, L. Bouffier, A. Kuhn, *Chem. Sci.* **2014**, *5*, 1961.

[53] C. Warakulwit, T. Nguyen, J. Majimel, M.-H. Delville, V. Lapeyre, P. Garrigue, V. Ravaine, J. Limtrakul, A. Kuhn, *Nano Lett.* **2008**, *8*, 500.

[54] G. Loget, G. Larcade, V. Lapeyre, P. Garrigue, C. Warakulwit, J. Limtrakul, M.-H. Delville, V. Ravaine, A. Kuhn, *Electrochimica Acta* **2010**, *55*, 8116.

[55] Z. Fattah, G. Loget, V. Lapeyre, P. Garrigue, C. Warakulwit, J. Limtrakul, L. Bouffier, A. Kuhn, *Electrochimica Acta* **2011**, *56*, 10562.

[56] Z. Fattah, P. Garrigue, B. Goudeau, V. Lapeyre, A. Kuhn, L. Bouffier, *Electrophoresis* **2013**, *34*, 1985.

[57] G. Loget, V. Lapeyre, P. Garrigue, C. Warakulwit, J. Limtrakul, M.-H. Delville, A. Kuhn, *Chem. Mater.* **2011**, *23*, 2595.

[58] G. Loget, J. Roche, A. Kuhn, *Adv. Mater.* **2012**, *24*, 5111.

[59] Z. Fattah, P. Garrigue, V. Lapeyre, A. Kuhn, L. Bouffier, *J. Phys. Chem. C* **2012**, *116*, 22021.

[60] L. Guo, P. C. Searson, *Electrochimica Acta* **2010**, *55*, 4086.

[61] L. Guo, G. Oskam, A. Radisic, P. M. Hoffmann, P. C. Searson, *J. Phys. D: Appl. Phys.* **2011**, *44*, 443001 (12pp).

[62] W. Stöber, A. Fink, E. Bohn, *J. Coll. Inter. Sci.* **1968**, *26*, 62.

[63] J. Gao, F. Tang, J. Ren, *Surf. Coat. Tech.* **2005**, *200*, 2249.

General conclusion and perspectives

In summary, this thesis addressed a strategy to generate chiral features at the molecular scale by electrochemistry and explored also the possibility to break the symmetry of initially non-conductive objects by bipolar electrochemistry.

The first chapter presented different strategies to generate chiral surfaces that can be used for electrochemical experiments. They can be obtained by the adsorption of chiral molecules, when exposing high Miller index surfaces or by molecular impression. The mesostructuration using a lyotropic liquid crystal phase as a template and subsequent electrochemical deposition was also presented since this allows increasing the electrochemical active surface area. The combination of the mesostructuration and molecular impression allows developing new metallic matrices for enantiorecognition and asymmetric synthesis by electrochemistry.

The second chapter was devoted to the development of this latter technology by using palladium which is very interesting for hydrogenation reactions. The first step was to obtain a mesoporous film by electrodeposition at the macroscale. Morphological analyses by scanning electron microscope were performed on the different films obtained with different deposition parameters (potential, temperature, surfactant, nature of substrate, treatment surface and the injected charge). However, none of these parameters provided encouraging results to obtain a smooth morphology. Moreover, the variation of the charge showed that the deposited palladium is not mesoporous.

In order to circumvent this problem, ultramicroelectrodes were finally used to remove the limitation of the diffusion of palladium ions, and the results were presented in the third chapter. A comparison of the deposits obtained at the macroscale and on ultramicroelectrodes highlights the benefit of using these smaller electrodes. Moreover, measurements of the active surface area by cyclic voltammetry indicates an increase by a factor of 100 of the surface compared to the geometrical area. Therefore, deposits were generated in the presence of chiral molecules and used as working electrodes to test their selectivity by differential pulsed voltammetry. So far, the experimental process is not optimal and still needs some investigation to provide reproducible results.

In order to explore further this topic, it is essential to gain a better understanding of the system, firstly focused on palladium, to discover why such irreproducible results were obtained, and also, to find a way allowing the development of mesoporous palladium at a larger scale. Second, this concept still requires a more exhaustive description using domains which are complementary to electrochemistry such as X-Ray diffraction or optical measurement.

Gathering more information about this concept, from the deposition to the recognition and synthesis, should allow optimizing the strategy. Moreover, the materials used so far are either expensive (platinum and platinum-iridium alloys) or fragile (nickel) and both of them present a modest yield for the conversion of prochiral molecules into enantiomers. The next development would be to electrodeposit an alloy which is stable and presents good catalytic properties to increase the rate of conversion.

The fourth chapter dealt with the break of the symmetry at the macro- and microscale by a two-step wireless modification of glass substrates. The first step was the use of electroless deposition of nickel by using a commercial bath. The second step consisted of performing bipolar electrochemical modification of the obtained substrates. First, a classical three-electrode setup was used to measure important parameters for the bipolar electrochemical experiments. Then, wireless electrochemical experiments were performed at different scales, from the centimeter- to the micrometer-scale. Glass slides and beads (centimeter- and millimeter-scale, respectively) were successfully modified by electroless deposition and subsequently by bipolar electrodeposition of platinum at one extremity of the substrate. Smaller beads (250 µm and 1 µm of diameter) still require an optimization of the electroless deposition process (a change in the sensitization procedure and a decrease of the mechanical impact between beads during nickel deposition). The optimization of the modification of smaller beads is of critical importance. Indeed, the next step of this project is the modification of nanohelices to produce chiral autonomous swimmers or the magnetic control of such nanohelices covered by nickel.

Experimental part

I. Chemicals, materials and apparatus

Chemicals		Supplier
Ch II and III	3,4-dihydroxy-L-phenylalanine ≥ 98 %	Sigma Aldrich
	3,4-dihydroxy-D-phenylalanine ≥ 95 %	Sigma Aldrich
	3,4-dihydroxy-DL-phenylalanine	Sigma Aldrich
	HCl, ACS reagent, 37%	Sigma Aldrich
	H_2SO_4, ACS reagent, 95.0-98.0 %	Sigma Aldrich
	$(NH_4)_2PdCl_4$, 97 %	Sigma Aldrich
	$C_{16}EO_8$, BioXtra, ≥ 98.0 %	Sigma Aldrich
	Brij® 56, polyoxyethylene cetyl ether (Not available anymore)	Sigma Aldrich
	Brij® C10, polyoxyethylene (10) cetyl ether, M_n ~ 683 g·mol^{-1}	Sigma Aldrich
	KNO_3, ACS reagent, ≥99.0%	Sigma Aldrich
	Fc(diMeOH), 97%	Sigma Aldrich
Ch IV	KOH, ACS reagent, ≥ 85%, pellets	Sigma Aldrich
	$SnCl_2 \cdot 2\ H_2O$, reagent grade, 98 %	Sigma Aldrich
	$PdCl_2$, anhydrous, 60 % Pd basis	Sigma Aldrich
	Nipol HP (Electroless bath)	Technic
	NaCl, ACS reagent, ≥ 99.0 %	Sigma Aldrich
	$NiCl_2 \cdot 6\ H_2O$, ReagentPlus	Sigma Aldrich
	$HAuCl_4 \cdot 3\ H_2O$, ACS Reagent, ≥ 49.0 % Au basis	Sigma Aldrich

	$H_2PtCl_6 \cdot x\ H_2O$, ~38% Pt basis	Sigma Aldrich
	HCl, ACS reagent, 37 %	Sigma Aldrich
	HCl, 0.01 N Standardized Solution	Alfa Aesar
	Tetraethyl orthosilicate (**TEOS**), reagent grade, 98 %	Sigma Aldrich
	NH_4OH, ACS reagent, 28.0-30.0 % NH_3 basis	Sigma Aldrich
	EtOH, absolute, suitable for HPLC, $\geq$ 99.8 %	Sigma Aldrich
Materials		Supplier
Ch II and III	PDE, Palladium electrode	Biologic
	Reference electrode, Ag/AgCl (3M NaCl)	IJCambria
	Platinum gauze, unimesh N7433, expanded metal mesh 0.34 mm	Alfa Aesar
	Gold-coated glass, 50x25x1 mm	A.C.M.
	10 µm dia. Platinum SECM Tip	IJCambria
Ch IV	Glass slides	
	Glass beads, 1 mm diameter	Sigma Aldrich
	Glass beads, unwashed 212-300 µm diameter	Sigma Aldrich
	Copper tape	
	Kapton®	
	Reference electrode Ag/AgCl	IJCambria
	Counter electrode, Pt mesh	Alfa Aesar
Apparatus		Supplier
Ch II and III	PGStat directed with Nova 2.5	Autolab
	Vega 3-SBH, tungsten filament source	Tescan

	XFlash 630-M Energy dispersive X-ray spectrometer (EDS)	Bruker
	Palmsens 4 directed by PSTrace 5.8	Palmsens
Ch IV	Vega 3-SBH, tungsten filament source	Tescan
	XFlash 630-M Energy dispersive X-ray spectrometer (EDS)	Bruker
	PGStat directed with Nova 2.5	Autolab
	Heinzinger, PNC 600-1000 pos	Heinzinger

II. Methods

II.1. Preparation of solutions

All solutions were prepared using MilliQ water (18.2 MΩ·cm)

II.2. Deposition of palladium films

Lyotropic liquid crystal was composed by 12 wt.% $(NH_4)_2PdCl_4$, 40 wt.% H_2O, 48 wt% surfactant (Brij® or $C_{16}EO_8$). First, the palladium salt was dissolved into water and only after the complete dissolution the surfactant was added. The mixture was mixed and heat above 70°C with a water bath in order to obtain the micellar phase and thus, to ensure the homogeneity of the gel. Afterwards, it was slightly cool down to room temperature.

The macroscopic working electrodes (Au- or Pt-coated glass, A = 0.25 cm^2) were cleaned by ultrasound in isopropanol, piranha solution, O_2 plasma or cyclic voltammetry in 0.5 M H_2SO_4 (no influence of the cleaning procedure has been observed). For the shown result, the cleaning by cyclic voltammetry in 0.5 M H_2SO_4 was performed.

The ultramicroelectrodes were polished and cycled in 0.5 M H_2SO_4 and then in 1 mM Fc(diMeOH) in 0.1 M KNO_3 to check the surface. The counter-electrode was burnt prior to every deposition.

After a certain number of deposition, the fritted part of the reference electrode gets colored and a shift of potential was observed. When it occurred, the reference electrode was changed.

At macroscopic scale (Chapter II), the obtained gel was placed on the working electrode, a platinum mesh was used as a counter electrode, placed on the top of the gel. A hole was made to the counter to let the reference electrode be in contact with the electrolyte.

At microscopic scale (Chapter III), the obtained gel was cool down and placed on the counter electrode. The ultramicroelectrode and the reference electrode were introduced inside the gel.

The electrochemical experiments were performed using a potentiostat: PGStat Autolab directed by Nova has been used for experiments at macroscale and Palmsens4 directed by PSTrace has been used for experiments at microscale and the system was placed in a Faraday cage for this latter case.

After deposition, the films were rinsed in milliQ water for 24h and the water was change regularly, to remove the maximum of the gel.

II.3. Differential pulse voltammetry

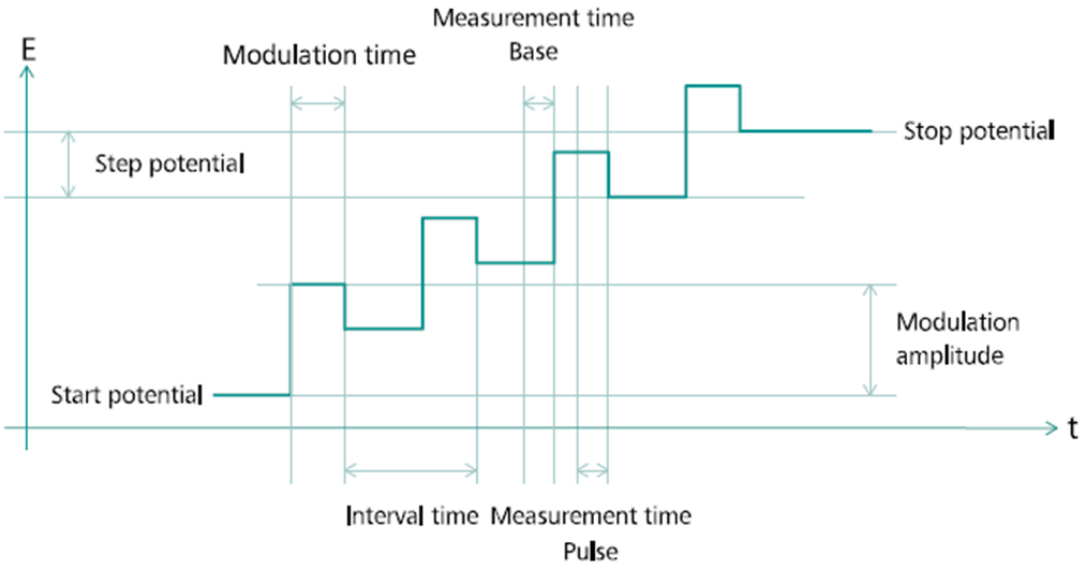

Figure 75: Parameters to define to register a DPV (from user manual of Nova software)

The DPV were recorded with the following parameters:

Step potential: 5 mV

Modulation amplitude: 50 mV

Modulation time: 50 ms

Interval time: 1.1 s

Scan rate: 50 $mV \cdot s^{-1}$

II.4. Electroless deposition process

Glass substrates (glass slides, glass beads 1mm, glass beads 212-300 µm) were sonicated in 2.5 mol·L^{-1} KOH for 15 minutes and rinsed with a flow a water afterwards. They were immersed in tin chloride solution ($4.4 \cdot 10^{-4}$ mol·L^{-1} in $1.2 \cdot 10^{-3}$ mol·L^{-1} HCl) for 1 minute, rinsed and immersed in palladium chloride solution ($5.6 \cdot 10^{-4}$ mol·L^{-1} in $1.2 \cdot 10^{-3}$ mol·L^{-1} HCl) for 1 minute and rinsed, representing the sensitization and activation steps, respectively.

Nickel bath was prepared according to the procedure given by the supplier (Technic). The pH was adjusted to 4.8, the temperature was controlled by a water bath to be at 88 °C. The volume of the plating bath was adapted to the surface to be covered in order to ensure a charge of 1.5 $dm^2 \cdot L^{-1}$ (surface of glass to cover per volume of nickel bath). The activated glass substrates were immersed in the nickel bath for 30 seconds. The thickness is estimated to be around 50 nm. This procedure gave a homogeneous coverage of the substrate.

The same procedure was used of the silica beads but an extra step of centrifugation (2000 rpm during 2 minutes) was added between each solution.

II.5. Bipolar electrochemistry experiments

BEC experiments were carried out in a homemade cell (Figure 76). The feeder electrodes were made out of a platinum mesh. The distance between the feeder electrodes (L) was kept constant at 3.5 cm. The bipolar electrode was positioned at the “gate” connecting the two feeder electrode compartments.

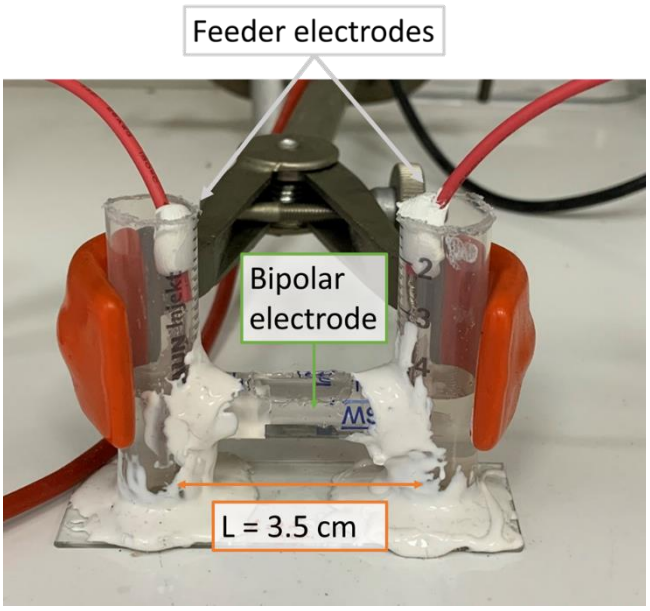

Figure 76: Picture of BEC cell

In the following table (Table 1), the different experimental parameters are summarized.

Table 1: Experimental parameters for BEC

Slides		
ΔV	BE length, d	E_{imp}
1.5 V	1.2 cm	4.4 V
3 V	1.25 cm	8.4 V
6 V	1.6 cm	13.1 V
12 V	1.3 cm	32.3 V
1 mm diameter beads		
ΔV	BE length, d	E_{imp}
1.5 V	1 mm	52.5 V
3 V	1 mm	105 V

II.6. Synthesis of silica beads

In a single-used container, 50 mL of EtOH were mixed with 12 mL of NH_3. The mixture was continuously stirred at 100 rpm. In a syringe, 5 mL of TEOS were diluted in 20 mL of EtOH. This mixture was added to the first mixture at a rate of 8 $mL.h^{-1}$ (Figure 77). At the end of the procedure, regular monodisperse beads were obtained with a diameter *ca.* 620 nm (Figure 78).

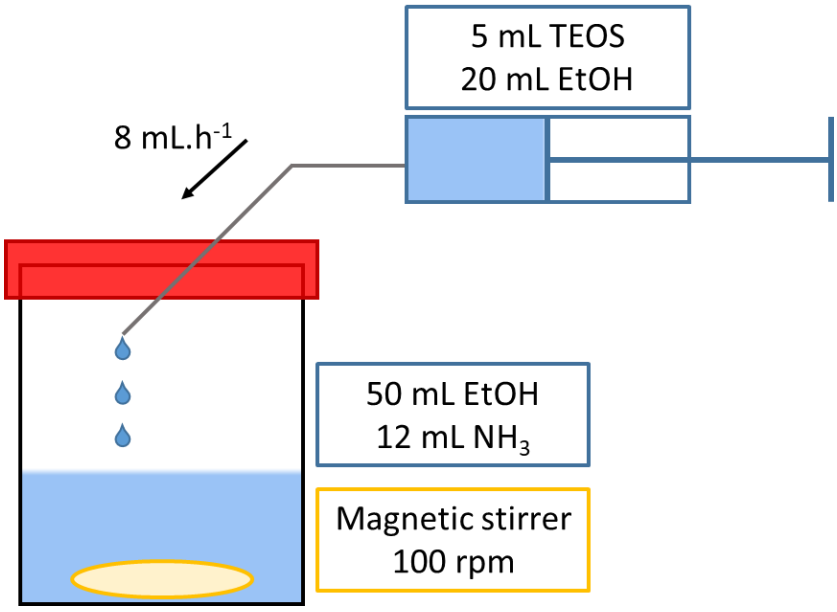

Figure 77: Setup for the silica seeds synthesis

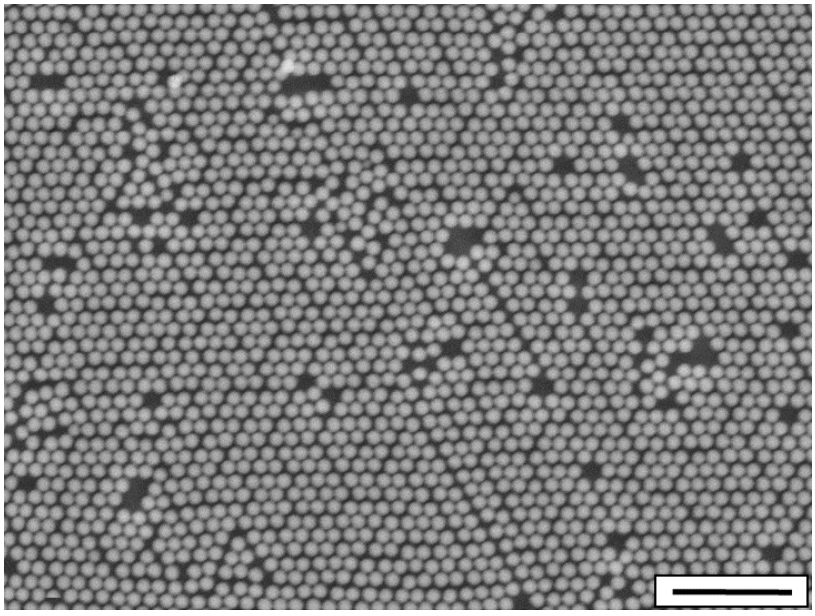

Figure 78: SEM image of silica beads after the first step of synthesis. Scale bar, 5 µm

A second step was added to reach a diameter of 1 µm. 10 % of the initial suspension was used for this second step. The total volume at the end of the first step was 87 mL, thus we took 8.7 mL to increase the diameter of the resulting beads. The 8.7 mL of the initial suspension were mixed with 50 mL of EtOH and 12 mL NH_3. The mixture was continuously stirred at 100 rpm. In a syringe, 1.6 mL of TEOS were diluted in 10 mL of EtOH. This mixture was added in the media at a rate of 20 $mL.h^{-1}$ (Figure 79). This procedure provided monodisperse silica beads of *ca.* 1 µm diameter (Figure 80).

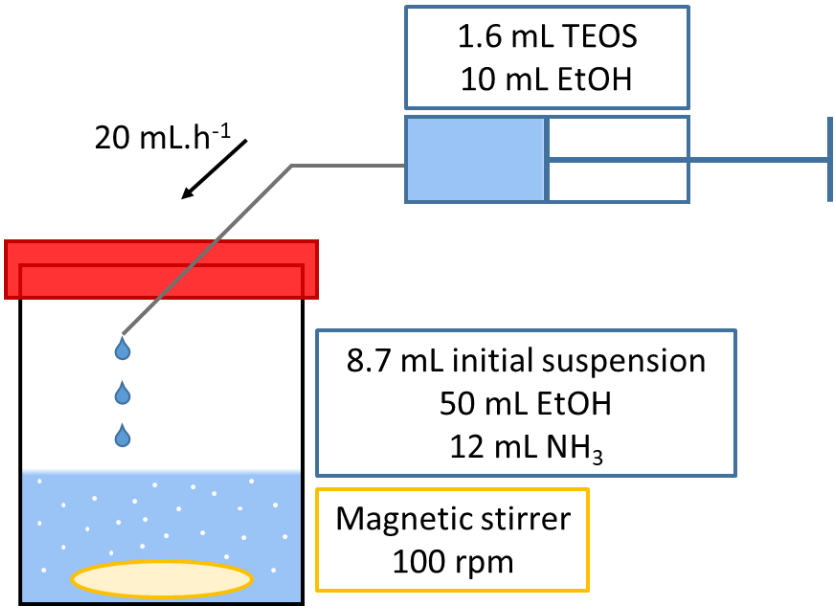

Figure 79: Growing of silica seeds

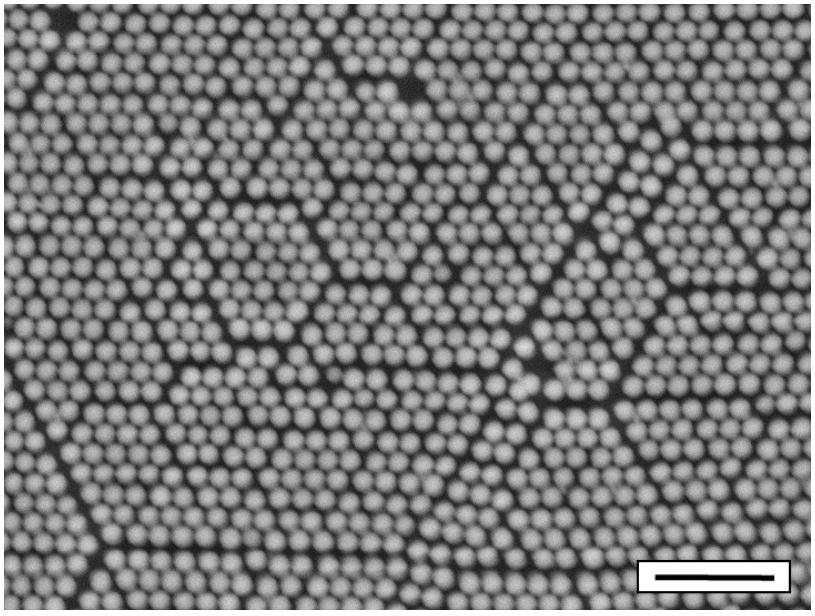

Figure 80: SEM image of silica beads after the growing step. Scale bar, 5 µm